Université Côte d'Azur
Ecole Doctorale de Sciences
Fondamentales et Appliquées

Humboldt-Universität zu Berlin
Mathematisch-
Naturwissenschaftliche Fakultät

Dissertation

Im Rahmen der binationalen Promotion

zur Erlangung der akademischen Grade

Doctor rerum naturalium (Dr. rer. nat.)

und

Docteur en Science

Im Fach Physik
Spezialisierung: Experimentalphysik

von

Natalia Stolyarchuk

Transmission electron microscopy study of polarity control in III-N films grown on sapphire substrates

Betreuer: Philippe Vennéguès / Prof. Dr. Henning Riechert

Tag der mündlichen Prüfung: 17.11.2017

Promotionskomission:

Dr. Martin Albrecht	Leibniz Institute for Crystal Growth	Examinator
Dr. Wilfried Blanc	CNRS-LPMC, Université Côte d'Azur	Examinator
Dr. Catherine Bougerol	CNRS-Institut Néel	Gutachterin
Prof. Dr. Nicolas Grandjean	Ecole polytechnique fédérale de Lausanne	Examinator
Prof. Dr. Ted Masselink	Humboldt-Universität zu Berlin	Gutachter
Prof. Dr. Henning Riechert	Humboldt-Universität zu Berlin	Betreuer
Philippe Vennéguès	CNRS-CRHEA, Université Côte d'Azur	Betreuer

Abstract

In this work we study the issue of polarity control in GaN and AlN films grown on (0001) epi-ready sapphire substrates by metal-organic vapor phase epitaxy (MOVPE). The layers are investigated at each growth step separately to follow the evolution of films' polarity during the growth process. A variety of experimental techniques is applied to study surface morphology, chemistry and atomic structure of the layers. Aberration-corrected high-resolution transmission electron microscopy (TEM) is the principal technique used for determination of the layer polarity. Additional information about the atomic structure of the layers was gained by high-angular annular dark field scanning TEM and electron energy-loss spectroscopy techniques. Our investigations have revealed the following main results:

(i) Metal polarity of AlN and GaN films is established during nitridation of the sapphire substrate at T $\geq$ 850 °C via formation of a rhombohedral aluminum-oxynitride structure ($Al_9O_3N_7$), that promotes the inversion from N-polarity at the sapphire substrate interface to Al-polarity at topmost monolayers of the nitridation layer. The AlN or GaN buffer layer deposited at low temperatures (580 – 650 °C) inherits metal polarity of the topmost $Al_9O_3N_7$ monolayers and protects it from dissociation during high temperature growth. When the low temperature buffer layer is omitted and a high temperature layer is deposited directly on the nitridated sapphire surface, $Al_9O_3N_7$ dissociates, which results in an N-polar monolayer at the surface and the layer deposited on top inherits N-polarity.

(ii) Nitridation for extended time and at high temperatures ($>$ 1000 °C) leads to transformation of smooth and closed aluminum-oxynitride films to heterogeneous three-dimensional films, where, in addition to a two-dimensional $Al_9O_3N_7$ film, three-dimensional AlN islands form. The AlN islands are Al-polar directly from the interface and more stable against dissociation at high temperatures. Metal polar AlN islands are responsible for inducing metal polar domains in the otherwise N-polar AlN films. While the aluminum-oxynitride layer is unstable under high temperature growth conditions and results in N-polar films after high temperature growth, Al-polar islands are stable and induce Al-polar columnar inversion domains in the N-polar AlN films.

(iii) We demonstrate the controlled inversion from N- to Al-polarity in films with mixed-polarity by applying ex-situ oxygen annealing as an intermediate step in MOVPE growth of AlN. The crystal structure of the inversion domain boundary is similar to the rhombohedral $Al_9O_3N_7$ phase and contains 1.5 monolayers of oxygen atoms. Hence, the polarity inversion by annealing in oxygen atmosphere follows mechanisms similar to aluminum-oxynitride formation due to nitridation.

Résumé

Cette thèse est dédié à l'etude du contrôle de la polarité dans les films de GaN et AlN épitaxiés sur (0001) substrats saphir par EPVOM. Les couches sont étudiées à chaque étape de croissance séparément pour suivre l'évolution de la polarité. Plusieurs techniques expérimentales sont utilisées pour étudier la morphologie de la surface, la chimie et la structure atomique des couches. La polarité est déterminée principalement par microscopie électronique en transmission (MET) haute résolution corrigée des aberrations. Des informations supplémentaires sur la structure atomique des couches sont été obtenues par microscope électronique à balayage en transmission en champ sombre et par spectroscopie de perte d'énergie des éelectrons. Nos recherches ont révélé les résultats principaux suivants :

(i) La polarité métallique des films AlN et GaN est établie au cours de la nitruration du substrat saphir à des températures supériores ou égales à 850 ° C par la formation d'une couche d'oxynitrure d'aluminium rhomboédrique ($Al_9O_3N_7$), qui induit une inversion de la polarité N à l'interface avec le substrat à vers la polarité Al dans les monocouches supérieures de la couche de nitruration. La couche tampon déposée à basse température (580 – 650 ° C) garde la polarité métallique des monocouches supérieures de $Al_9O_3N_7$ et les protège de la dissociation pendant la croissance à haute température. Si la couche tampon est omis et qu'une couche haute température est déposée directement sur la surface de saphir nitrurée, $Al_9O_3N_7$ se dissocie et découvre les couches de polarité à l'interface. Dans ce cas, la couche déposée reproduit la polarité N des couches interfaciales.

(ii) Une nitruration longue à des températures élevées ($>$ 1000 ° C) conduit à la transformation du film d'oxynitrure d'aluminium lisse et continu en film tridimensionnel hétérogènes. Des îlots d'AlN se forment en plus d'un film bidimensionnel $Al_9O_3N_7$. Les îlots AlN sont de polarité Al dès l'interface et sont stables à haute température. Les îlots AlN de polarité métallique induisent des domaines de polarité Al dans les films AlN majoritairement de polarité N. Alors que la dissociation de la couche d'oxynitrure d'aluminium dans des conditions de croissance haute température conduit à des films de polarité N, les îlots d'AlN de polarité Al sont stables et induisent la présence de domaines d'inversion colonnaires dans les films AlN.

(iii) Nous montrons qu'il est possible d'inverser de façon contrôlée la polarité N des films EPVOM d'AlN de polarité mixte en introduisant un recuit ex-situ d'oxygène en cours de la croissance. La structure cristalline de la paroi d'inversion de domaine est similaire à celle de la phase rhomboédrique de $Al_9O_3N_7$ et contient 1,5 monocouches d'atomes d'oxygène. L'inversion de polarité par recuit dans l'atmosphère oxygène

suit des mécanismes similaires à la formation de l'oxynitrure d'aluminium due à la nitruration.

Kurzzusammenfassung

In dieser Arbeit untersuchen wir die Fragestellung der Polaritätskontrolle in GaN- und AlN-Schichten, die mittels metallorganischer Dampfphasenepitaxie (MOVPE) auf (0001) Saphirsubstraten gewachsen worden sind. Die Schichten werden nach jedem Wachstumsschritt separat untersucht, um die Entwicklung der Polarität der Schichten während des Wachstumsprozesses Schritt für Schritt nachvollziehen zu können. Eine Vielzahl von experimentellen Methoden wird angewendet, um die Oberflächenmorphologie, die chemische Zusammensetzung und die atomare Struktur der Schichten zu untersuchen. Die Polaritätsbestimmung wird im Wesentlichen durch aberrationskorrigierte hochauflösende Transmissionselektronenmikroskopie durchgeführt. Um zusätzliche Informationen über die Schichten zu erlangen, wurden die Proben unter Verwendung von Rastertransmissionselektronenmikroskopie Dunkelfeldabbildung und Elektronenenergieverlust-Spektroskopie analysiert. Unsere Untersuchungen haben folgende Ergebnisse hervorgebracht: (i) Die Metallpolarität von AlN- und GaN-Schichten stellt sich bereits während der Nitridierung des Saphirsubstrats bei Temperaturen ≥ 850 ° C durch Bildung einer rhomboedrischen Aluminiumoxynitridstruktur ($Al_9O_3N_7$) ein, die eine Umkehr der zunächst N-Polarität der Schicht direkt an der Grenzfläche zum Saphirsubstrat hin zu Al-Polarität in den oberen Monolagen der Nitridierungsschicht bewirkt. Die bei niedriger Temperatur (580 – 650 ° C) abgeschiedene Pufferschicht übernimmt die Metallpolarität der oberen Monolagen der Nitridierungsschicht und schützt diese vor Zersetzung während des folgenden Hochtemperaturwachstums. Wenn die Niedertemperatur-Pufferschicht weggelassen wird und direkt auf der nitridierten Saphiroberfläche ein Hochtemperaturwachstumsschritt folgt, dissoziiert die $Al_9O_3N_7$ Schicht, was zu einer N-polaren Monolage an der Grenzfläche zum Saphirsubstrat und somit zu N-Polarität in der darauf abgeschiedene Schicht führt. (ii) Eine Nitridierung für längere Zeit und bei hohen Temperaturen (> 1000 ° C) führt zu einem Übergang von glatten und geschlossenen Aluminiumoxynitrid-Schichten hin zu heterogenen und dreidimensionalen Filmen, bei denen sich neben der zweidimensionalen $Al_9O_3N_7$ Schicht ebenfalls dreidimensionale AlN-Inseln ausbilden. Die AlN-Inseln weisen direkt ab der Grenzfläche zum Saphirsubstrat Al-Polarität auf und sind stabiler gegen Dissoziation bei hohen Temperaturen. Metallpolare AlN-Inseln sind verantwortlich für das Auftreten von metallpolaren-Domänen in den ansonsten N-polaren AlN-Filmen. Während die Aluminiumoxynitrid-Schicht unter Hochtemperatur-Wachstumsbedingungen instabil ist und zu N-polaren Filmen nach dem Hochtemperaturwachstum führt, sind Al-polare Inseln stabil und induzieren Al-polare säulenförmige Inversionsdomänen in den N-polaren AlN-Schichten. (iii) Eine ex-situ Sauerstoff-Behandlung als Zwischenschritt während des MOVPE-Wachstums von AlN bewirkt eine kontrollierte Umkehr

von N- zu Al-Polarität in gemischtpolaren Schichten. Die Kristallstruktur der Inversionsdomänengrenze ähnelt der rhomboedrischen $Al_9O_3N_7$-Phase und enthält 1.5 Monolagen Sauerstoff. Die Polaritätsumkehr durch Behandlung in einer Sauerstoffatmosphäre folgt den Mechanismen ähnlich der Aluminiumoxynitrid-Bildung während der Nitridierung.

Contents

[1]The data of HRTEM and HAADF-STEM investigations of AlN templates was contributed by Stefan Mohn. It is a result of his study of AlN templates grown on Al_2O_3 substrates by MOVPE and provided by Z.Sitar group from North Carolina State University. The results are published as a part of common work in [1].

Introduction

The Group III-nitrides (GaN, AlN, InN and their alloys) today form one of the most important material system for optoelectronic and electronic applications, such as blue and green light emitting diodes (LED), semiconductor lasers or high electron mobility transistors (HEMT). Thermodynamically stable wurtzite phase lacks inversion symmetry and has polar axes along the *c*-direction, that are classified as N-polar or Metal (Ga, Al, In) polar. III-Nitrides therefore exhibit spontaneous polarization in addition to piezoelectric polarization caused by biaxial strain in coherently grown heterostructures. The direction of internal fields caused by the spontaneous polarization is opposite for N-polar and metal-polar films and significantly influences the formation of two-dimensional electron gas (2DEG) and the optical properties of light emitting devices. [2, 3] In addition, the polarity of the growth surface influences impurity incorporation, adatom transport and defect formation. [4, 5, 6] Therefore, polarity is a critical issue for III-nitrides material system, that has an impact on the quality of epitaxial films and the performance of nitride-based devices.

The vast majority of today‘s group-III nitride devices are based on metal-polar heteroepitaxial layers grown on non-polar sapphire substrates, which are among the most common used substrates due to their low cost and accessibility. Metal polar surfaces exhibit two main advantages, when compared to their N-polar counterparts: orders of magnitude lower concentrations of abundant impurities (e.g. oxygen) [6] and a higher surface diffusivity [5], that promotes step-flow growth and improves structural perfection of the heterostructure. [7] The classical scheme of MOVPE growth of metal polar III-nitride films on sapphire includes three main steps: first the surface of the sapphire is exposed to ammonia at high temperature (commonly known as nitridation); then a thin buffer layer of AlN or GaN is deposited onto the nitridated surface at relatively low growth temperatures and subsequently annealed at high temperatures; finally an epitaxial GaN or AlN film is grown on top of the buffer layer at high temperatures. This process results in smooth high quality films, which are metal-polar as shown later by Rouviere et al. [7] The concept of sapphire nitridation was first suggested by Kawakami et.al. [8] and insertion of low temperature buffer layer was among the breakthroughs made by Amano, Akasaki and Nakamura that significantly improved the quality of GaN epitaxial layers and paved the way to device grade group-III nitride materials in the past. [9, 10]

Recently, however, layers with N-polarity gained new interest as it has been discovered that N-polar III-nitrides films have a number of advantages for device applications. They can be used as high-frequency high electron mobility transistors (HEMTs), because they provide an improved confinement of the 2D electron gas

and a suppression of short channel effects due to the back barrier. [11, 12, 13] Besides, Verma et.al. showed the advantages of using N-polar structures for improving efficiencies of visible blue and green LEDs and lasers application. [14] Despite of these advantages, most N-polar AlN and GaN films are still characterized by a rough surface morphology and the presence of inversion domains with metal polarity (ID), which deteriorate the properties of the resulting devices. [7, 15, 16, 17]
Another important application which comes with control of polarity is the possibility of fabricating structures, where domains with defined sizes and different polarities can be grown side-by-side on a non-polar substrate. [3, 18, 19] This approach opens fascinating perspectives for device concepts based on polarity engineering, such as quasi-phase matching structures for second harmonic generation [20] or the realization of 2DEG in lateral polarity junctions for electronic applications. [21, 3, 22]
Although the question of polarity control during growth of III-nitride films is of great importance, there is still lack of understanding of the elementary mechanisms that are responsible for establishing metal or nitrogen polarity of the films on non-polar substrate. The existing concepts are based on empirical observations and even contain ambiguous results, thus they are not able to provide reliable roadmaps for controlled growth of N-polar layers or structures with lateral polarity junctions. One of the main reasons for that was – at the time, the lack of precise analytical tools, allowing localized determination of polarity and atomic structure of layers, at the time, when main concepts for polarity control were established.
The aim of this work is to develop a concept of polarity control in AlN and GaN layers grown by MOVPE on sapphire substrates, based on data obtained by rigorous analysis using various experimental methods, such as atomic force microscopy (AFM), X-ray photoelectron spectroscopy (XPS), conventional and high resolution (HR) transmission electron microscopy, scanning TEM (STEM) and electron energy loss spectroscopy (EELS). We investigate the polarity of the layers by aberration corrected HRTEM and high resolution high-angle annular dark field (HAADF) scanning TEM, which allow us to resolve even oxygen and nitrogen atomic columns, so that the polarity of layers can be determined directly and locally with atomic resolution. In chapter 1 we are giving a detailed description of each of the analytical methods and tools used in this work along with the description of the group III-nitrides material system and MOVPE growth technique as applied to III-N growth..
We investigate the surface morphology of layers, their chemical properties, atomic structure and, in particularly, their polarity at each growth step. The main focus of the study will be on understanding the atomic processes, governing the polarity selection during initial steps of the MOVPE growth. Therefore, chapter 2 is dedicated to the study of the effect of nitridation – annealing of sapphire substrate in NH_3 ambient at high temperature. We conduct the study on the effect of the nitridation conditions, such as temperature and duration of annealing, on the structural properties of the sapphire surface after nitridation. In chapter 3 we investigate the role of the low temperature buffer layer and develop a model elucidating the mechanism of polarity selection in MOVPE growth of III-nitride films. In chapter 4 we analyze

the limitations of this model for the growth of N-polar films and discuss how fundamental processes taking place during sapphire nitridation influence the polarity uniformity of N-polar films. In the last chapter 5 we will show how understanding of the mechanism, governing the polarity selection during MOVPE growth, allows us to introduce a method for controlled switch of the polarity in AlN films, which opens attractive possibilities for engineering devices with heteropolar junctions.

1. Theoretical background and experimental methods

1.1. Structural properties

III-Nitride materials

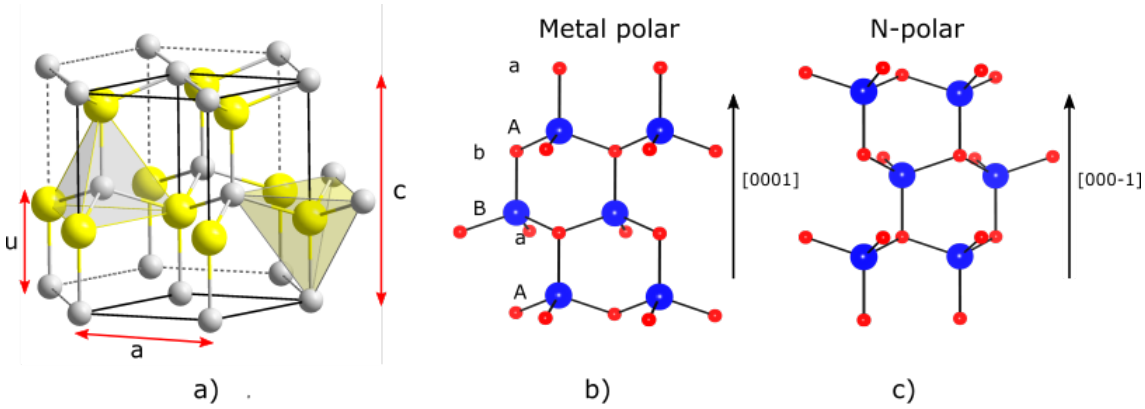

Figure 1.1.: Crystal structure of wurtzite III-nitride. a) Three-dimensional model. Metal atoms are displayed in yellow, N atoms are displayed in gray. c and a are lattice parameters, u – is a bond length; b) and c) Wurtzite lattice in [0001] and [000$\bar{1}$] directions, corresponding to Metal polar and N-polar III-nitride. (Here and further metal atoms are displayed as blue balls, N atoms are displayed as red balls) "AaBbAa" letters denote stacking sequence of wurtzite lattice. .

III-nitride materials exist in two different crystallographic phases – wurtzite and zinc-blend. The wurtzite phase is the phase that is thermodynamically stable under ambient pressure. In this phase atoms hybridize in sp3-configuration. Each group III-atom is bonded to four N atoms, forming a tetrahedron (fig.1.1 (a)). The arrangement of the atoms can be described by two close-packed sub-lattices, shifted with respect to each other by a lattice vector $< \frac{1}{3}, \frac{1}{3}, \frac{1}{2} >$. These two sub-lattices form a stacking sequence of AaBbAaBbAaBb, as it is shown in fig.1.1 (b). The distance between two neighboring atoms in the basal plane equals the a lattice parameter. The distance between two basal planes consisting of atoms of the same type equals the c lattice constant. The distance between two basal planes with atoms of different type is assigned as u.

Wurtzite belongs to the P63mc symmetry group. In wurtzite lattice the *c*-axis is unique, i. e. there is no other equivalent axis that can be by obtained by a symmetry operation. The directions [0001] and [000$\bar{1}$] are not equivalent and *c*-axis is polar. The [0001] direction is defined by a vector that points from the the III-metal atom towards the N-metal atom and is collinear with the c-axis (fig.1.1 (b)). The structure grown along this direction is called metal polar. The [000$\bar{1}$] is defined by a vector that points from the N atom towards the III-metal atom and is collinear to the c-axis. The crystal grown along this direction is called "N-polar" (fig.1.1 (c)).

Material	a , Å	c, Å	c/a	u/c
AlN	3.112	4.982	1.600	0.382
GaN	3.189	5.185	1.626	0.377

Table 1.1.: Lattice parameters of AlN and GaN.

The wurtzite unit cell contains two atoms: N atom on $(\frac{2}{3}, \frac{1}{3}, 0)$ site and metal atom on $(\frac{2}{3}, \frac{1}{3}, \frac{3}{8})$ site. This result in $c/a = 1.633$ and $u/c = 0.375$. The experimentally measured lattice constants of AlN and GaN deviate from the values of ideal wurtzite lattice. [23, 24, 25]
In fact the tetrahedron is compressed along the *c*-direction in comparison with ideal wurtzite. The deviation from the ideal wurtzite structure produces an electronic dipole along *c*-direction that creates an internal spontaneous polarization within the crystal. The direction of spontaneous polarization is opposite to [0001] direction and points from N-atom to metal atom.

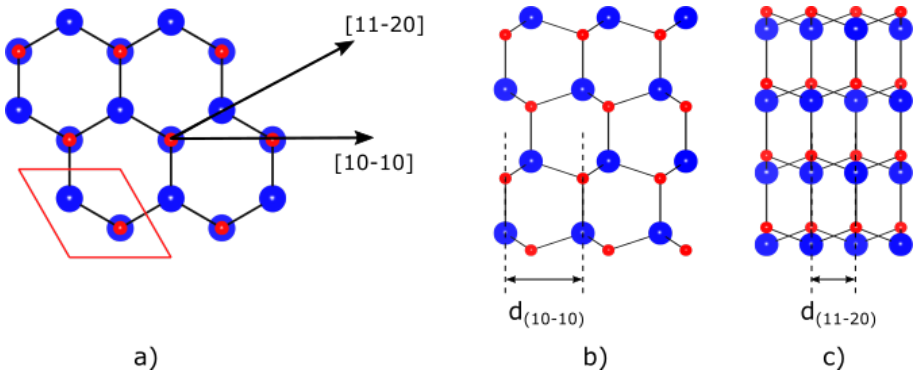

Figure 1.2.: Perspectives of wurtzite along [0001] (a), [11$\bar{2}$0] (b) and [10$\bar{1}$0] (c) directions. Red parallelogram illustrates unit cell in the [0001] projection. $d_{(10\bar{1}0)}$ and $d_{(11\bar{2}0)}$ are distances between nearest identical planes in [11$\bar{2}$0] and [10$\bar{1}$0] projections, respectively.

In this work we performed transmission electron microscopy investigations (see 1.2) of AlN and GaN epitaxial layers along two principal projections: [11$\bar{2}$0] and [10$\bar{1}$0]. The wurtzite structure in these two projection is shown on fig. 1.2 (b) and (c). The

inter-planar distances in these projection are:

$$d_{(10\bar{1}0)} = \frac{\sqrt{3}}{2}a,\ d_{(11\bar{2}0)} = \frac{1}{2}a$$

For AlN material the inter-planar distances in these two projections are: $d^{\mathrm{AlN}}_{(10\bar{1}0)}$= 2.695 Å, $d^{\mathrm{AlN}}_{(11\bar{2}0)}$= 1.55 Å.

Al_2O_3 structural properties

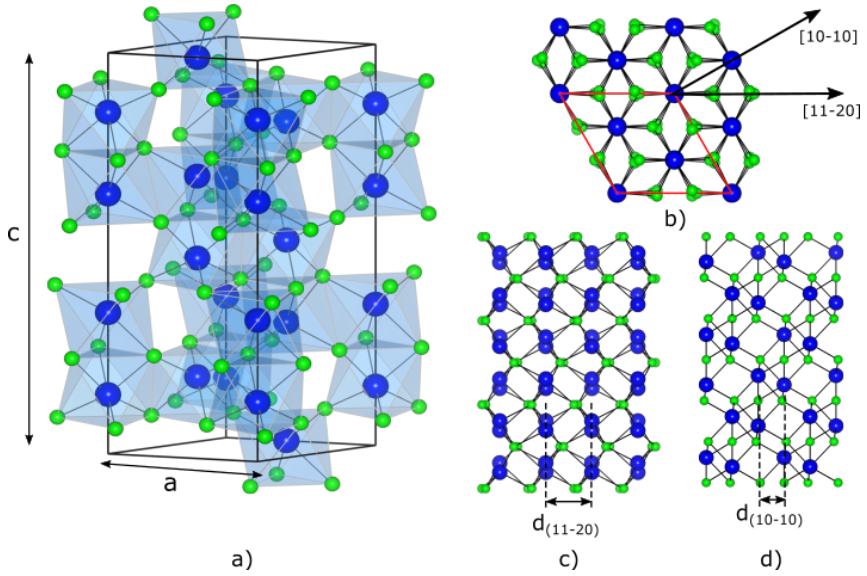

Figure 1.3.: Crystal structure of Al_2O_3. (Blue balls denote Al atoms, green balls denote oxygen atoms) a) Three-dimensional model. a and c – lattice parameters; b), c) and d) Perspectives of Al_2O_3 along [0001], [10$\bar{1}$0] and [11$\bar{2}$0] directions, respectively. $d_{(11\bar{2}0)}$ and $d_{(10\bar{1}0)}$ are interplanar distances in [10$\bar{1}$0] and [11$\bar{2}$0] projections.

In this work we study AlN and GaN layers epitaxially grown on sapphire substrate. Sapphire – Al_2O_3 – has the corundum crystal structure, which belongs to the rhombohedral crystal system. Aluminum atoms are located in the center of octahedra and are octahedrally coordinated with oxygen atoms (fig.1.3 (a)).
The unit cell of corundum sapphire contains 12 aluminum atoms and 18 oxygen atoms. Lattice constants of Al_2O_3 are shown in tab.1.1.

a, Å	c, Å	$d^{Al_2O_3}_{(10\bar{1}0)}$, Å	$d^{Al_2O_3}_{(11\bar{2}0)}$, Å
4.76	12.89	1.37	2.379

Table 1.2.: Lattice parameters and interplanar distances in Al_2O_3.

When AlN and GaN are grown along [0001] on *c*-sapphire, two hexagonal lattices matches, introducing rotation of 30°, and epitaxial relations between are AlN (GaN) and Al_2O_3 are known to be: [26, 27]

$$[0001]_{Al_2O_3} \Longleftrightarrow [0001]_{AlN},$$

$$[10\bar{1}0]_{Al_2O_3} \Longleftrightarrow [11\bar{2}0]_{AlN},$$

$$[11\bar{2}0]_{Al_2O_3} \Longleftrightarrow [10\bar{1}0]_{AlN}.$$

The inter-planar distances in sapphire along $[11\bar{2}0]$ (fig.1.3 c) and $[10\bar{1}0]$ (fig. 1.3 d) projections are shown in tab.1.2.

1.2. Transmission electron microscopy

In this work we applied transmission electron microscopy (TEM) to study the morphology of the epitaxial layers, their atomic structure and, in particular, polarity of III-nitride layers grown on sapphire substrates. For these purposes we used three principal methods: diffraction contrast imaging, high resolution TEM and Z-contrast imaging in scanning transmission electron microscopy. Moreover, we applied electron energy-loss spectroscopy to investigate chemical composition of epitaxial layers. We will give a brief overview on basic principles of each of these techniques. For more detailed information on TEM we refer to the books by Williams and Carter [28] and Fultz and Howe [29]. For the details on STEM and EELS methods we refer to the books by Pennycook and Nellist [30] , Brydson [31] and Egerton [32].

1.2.1. Basic principles of operation and imaging

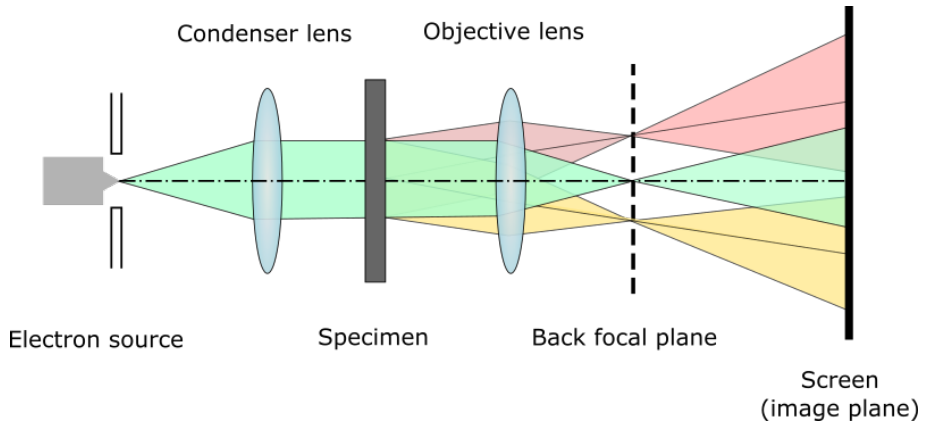

Figure 1.4.: Basic principle of image formation in TEM. The horizontal dashed-dotted line illustrates the optical axis of the microscope.

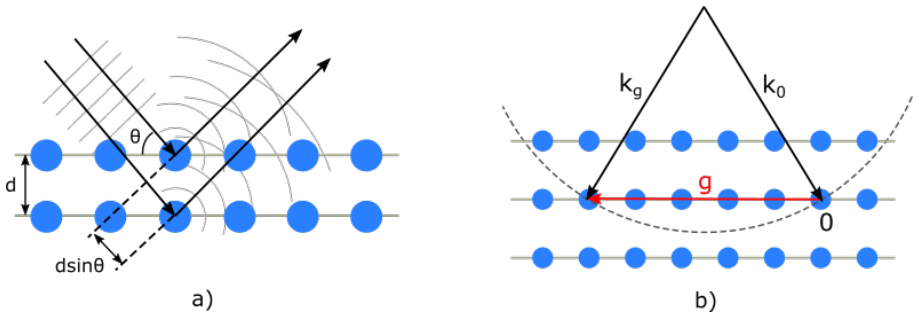

Figure 1.5.: Schematic representation of plane wave diffraction on a crystal. a) Real space: blue circles and horizontal line represent lattice planes with atoms, on which the incident plane wave is diffracted; light gray lines and circle segments represent wave fronts of the incident and diffracted waves, respectively. (b). Reciprocal space: blue circles represent reciprocal lattice points; vectors $\vec{k}_0$ and $\vec{k}_g$ are the wave vectors of the incident and diffracted beam, and $\vec{g}$ is the diffraction vector; the dashed gray circle represents the Ewald sphere with a radius of $\left|\vec{k}_0\right| = 1/\lambda$, that passes through the origin point of reciprocal lattice "0".

Fig.1.4 shows the principle scheme of optical column of transmission electron microscope. The electron source generates electrons, which are accelerated by the voltage applied to the anode. The wave length λ of the resulting electron wave is given by De Broglie equation: [28]

$$\lambda = \frac{h}{\sqrt{2m_0eU(1+\frac{eU}{2m_0c^2})}}, \tag{1.1}$$

where U – accelerating voltage, h – Planck constant, e and m_0– electron charge and mass respectively, c– speed of light.
The experiments performed in this work were made at an accelerating voltages of either $U = 300$ kV or $U = 200$ kV . The corresponding values for the wavelengths are $\lambda = 1.97$ pm and$\lambda = 2.51$ pm, respectively. The condenser lens system, situated below, forms a parallel electron beam, which can be described as a plane wave:

$$\Psi_0 = A_0 exp\left[2\pi i(\vec{k_0}\cdot\vec{r})\right], \tag{1.2}$$

where A_0– amplitude of plane wave;$\vec{k_0}$– the wave vector with $\left|\vec{k_0}\right| = \frac{1}{\lambda}$.
The plane wave is transmitted through electron transparent specimen. The interaction of the electron wave with the specimen results in coherent elastic scattering, incoherent quasi-elastic scattering and inelastic scattering. Depending on the scattering type, different kinds of information on the specimen can be collected. If electrons are scattered inelastically due to interaction with the electrons of the specimen atoms they loose characteristic energies that can be analyzed by electron energy-loss spectrometer (EELS). From the analysis of the energy spectra of these

electrons useful information on the chemical composition and electronic excitation of the specimen may be obtained. More details on this method will be given further in 1.2.6. Useful information can also be gained by analyzing secondary processes resulting from inelastic interactions. For example, emission of secondary electrons can be analyzed by Auger electron spectroscopy, emission of characteristic X-rays – by energy dispersive X-ray spectroscopy (EDXS), visible light – by cathodoluminescence (CL) detector.

When the incident plane wave is coherently elastically scattered by the periodically arranged atoms of a crystal, the atoms, according to Huygens' principle, may be considered as a source of a secondary spherical wavelets (fig.1.5 (a)). This wavelets are expressed by: [28]

$$\Psi_s = \Psi_0 f(\theta) \frac{1}{R} exp(2\pi i k R), \tag{1.3}$$

where R – is the distance from the scattering center; $f(\theta)$ – atomic scattering factor, which is a measure of the scattered electron wave amplitude.

The superposition of the scattered waves will result either in constructive or destructive interference. The criterion for constructive interference is fulfilled when the difference of path lengths between spherical waves, emitted by atoms from the adjacent planes, is an integer multiple of the wavelength λ. This condition is also known as Bragg's law of diffraction:

$$2d_{hkl} sin\theta = n\lambda, \tag{1.4}$$

where d_{hkl} – is the distance between (h, k, l) diffracting lattice planes.

In reciprocal space the analogue of the Bragg's law takes the form of the Laue equation:

$$\vec{k_g} - \vec{k_0} = \vec{g} \tag{1.5}$$

where $\vec{k_g}$and $\vec{k_0}$– are the wave vectors of diffracted and incident wave, respectively (fig.1.5 (b)).

This mean that the wave is diffracted if the difference between the diffracted and incident wave vectors equals a reciprocal vector of the lattice $\vec{g}$ ($|\vec{g}| = \frac{1}{d_{hkl}}$). In terms of the Ewald sphere, that has its center at the origin of the incident wave vector $\vec{k_0}$ and radius $r = \left|\vec{k_0}\right| = \frac{1}{\lambda}$, diffraction will occur when the Ewald sphere passes through the point in the reciprocal lattice.

The resulting electron wave at the exit surface of the specimen will be a sum of discrete components, corresponding to diffracted waves, that satisfy the condition 1.5: [33]

$$\Psi_{exit}(\vec{r}) = \sum_g \Psi_g(\vec{r}) = \sum_g A_g \left[2\pi i(\vec{k_g} \cdot \vec{r}) + \phi_g\right], \tag{1.6}$$

where A_g and ϕ_g– are the amplitude and phase shift of the diffracted waves.

When the electron wave leaves the crystal at its back side it forms a diffraction pattern image in the back focal plane of the objective lens. The amplitude and phase of electron wave at the exit of the specimen are then modulated by means of

objective lens system, so that the electron wave function at the exit of the specimen is not identical to the wave function in the image plane. In the back focal plane of the objective lens the electron wave function is a Fourier function of spatial frequencies q, given by: [33]

$$\Psi^{'}(q) = \mathscr{F}(\Psi_{exit}(\vec{r})) \cdot T(q), \tag{1.7}$$

where q – is a spatial frequency; $\mathscr{F}$ – Fourier transformation; $T(q)$ – the objective lens transfer function, which represents the impact of the objective lens on the exit electron wave wave as a function of spatial frequency.
After the electron wave propagates from the back focal plane of the objective lens to the imaging device (fluorescence screen or CCD camera), the wave function in the image plane is given by an inverse Fourier transformation:

$$\Psi_{image}(x, y) = \mathscr{F}^{-}(\Psi^{'}(q)) \tag{1.8}$$

At last, the information that we measure on the fluorescent screen or CCD camera is the intensity distribution of this wave on the image plane, given by complex conjugate of wave function :

$$I_{image}(x, y) = \Psi_{image}(x, y) \cdot \Psi^{*}_{image}(x, y) = |\Psi_{image}(x, y)|^2 \tag{1.9}$$

Transfer function

According to [28], mathematically the transfer function is given by:

$$T(q) = A(q) \cdot E(q) \cdot exp(i\chi(q)), \tag{1.10}$$

where $A(q)$ – is the objective aperture function, that cuts off all the spatial frequencies above $q_{aperture}$; $\chi(q)$ – phase-distortion function of the objective lens; $E(q)$ – envelope function.
The phase-distortion function $\chi(q)$ mainly arises from the fact that electron waves are affected by spherical aberration C_S and defocus Δf. Spherical aberration is a lens aberration that results in different foci of a monochromatic wave, emitted from a point object on the optical axis due to stronger refraction for the waves passing further from the optical axis.
$\chi(q)$ is given by a sum of two contributions: [28]

$$\chi(q) = \pi\lambda q^2 \Delta f + \frac{\pi}{2}\lambda^3 q^4 C_S, \tag{1.11}$$

Therefore, when the electron wave passes through objective lens, $\chi(q)$ introduces phase shift (from $-\pi$ to $+\pi$), which is dependent from spatial frequency.
The envelope function $E(q)$ describes the attenuation of an electron wave function due to chromatic effects and limited spatial coherence. It can take values in the range from 0 to 1.

Mathematically, the envelope function is expressed as a product of separate components:

$$E(q) = E_S(q) \cdot E_C(q) \cdot E_D(q) \cdot E_V(q), \tag{1.12}$$

where:
$E_S(q)$ – envelope function due to limited spatial coherence;
$E_C(q)$ – envelope function due to chromatic aberration;
$E_D(q)$ – envelope function due to specimen drift;
$E_V(q)$ – envelope function due to specimen vibration;
In case of an ideal parallel illumination, the term $E_S(q)$ can be canceled out. If the drift and vibrations of the sample are negligible, the damping of transfer function will be mainly limited by chromatic chromatic aberrations. Chromatic aberration occurs due to non-monochromaticity of the incident electron beam. This means that waves of different energies (i.e. wavelengths) emitted from one point, are not focused into one point. The envelope function of chromatic aberration is expressed by: [28]

$$E_C(q) = exp\left[-\left(\pi\lambda\frac{\Delta}{2}\right)^2 q^4\right], \tag{1.13}$$

where Δ– is the defocus spread due to chromatic aberration, which depends on energy spread of electron beam ΔE, instabilities in high voltage U and lens current I:

$$\Delta = C_C\sqrt{\left(\frac{\Delta E}{E}\right)^2 + \left(\frac{\Delta U}{U}\right)^2 + 4\left(\frac{\Delta I}{I}\right)^2} \tag{1.14}$$

Using a field emission gun (FEG) as an electron source, improves the monochromaticity of the electron beam and reduces the term $\frac{\Delta E}{E}$ in eq.1.14, thus extending the envelope function to higher frequencies. For modern microscopes defocus spread Δ may reach few nanometers.
According to eq.1.13, the envelope function stronger damps the electron waves with higher spatial frequencies, i.e. waves that scatter at higher angles θ. Therefore, the envelope function limits the resolution of the microscope. The spatial frequency, at which the envelope function has dropped to a value $\frac{1}{e^2}$ is defined as information limit of the microscope. For the TEM used for high-resolution measurements in this work, the information limit is approximately 12.5 nm^{-1} which results in spacial resolution of 0.8 Å.

1.2.2. High-resolution transmission electron microscopy

Let us now consider a specimen, so thin, that its inner potential only slightly modulates the phase of the entering electron wave.
The potential of the specimen, which an electron “feels” when it passes through it,

is called a projected potential and for thin specimens, can be expressed as: [28]

$$V_t(x,y) = \int_0^t V(x,y,z)dz \tag{1.15}$$

When an electron wave passes through a thin specimen with thickness t, the total shift of its phase is given by:

$$d\phi = \sigma V_t(x,y), \tag{1.16}$$

where $\sigma = \frac{\pi}{2\lambda}$ and is called an interaction constant.
Then the electron wave at the exit surface of the specimen Ψ_{exit} may be expressed as:

$$\Psi_{exit}(x,y) = \Psi_0 exp(-i\sigma V_t(x,y)), \tag{1.17}$$

This representation, when we consider a specimen being a phase object (that only changes the phase of an electron wave) is called phase-object approximation and it only holds for thin specimens.
If we assume that the thickness t of the specimen is very small (few nm), then $V_t(x,y) \ll 1$ in eq. 1.17. Normalizing eq.1.17 with $\Psi_0 = 1$ and extending the exponential function we obtain:

$$\Psi_{exit}(x,y) \approx 1 - i\sigma V_t(x,y) \tag{1.18}$$

This approximation for very thin specimens is called Weak Phase-Object Approximation (WPOA). This approximation states that for thin specimens the amplitude of wave function at the exit of the specimen is linearly related to the projected potential of the specimen.
According to 1.9, during imaging in an electron microscope with an ideal lens with no aberrations we measure the amplitude of electron wave in the image plane $I_{image}(x,y)$, which is a complex conjugate of wave function, and will be equal on the whole image. The phase of the electron wave, that contains all the information about the atomic structure of the specimen, is therefore lost. We can restore the phase contrast in the image by considering the phase shift that electron wave experiences when it transfers through the objective lens system. As we have shown in earlier, the phase shift is given by the phase-distortion function $\chi(q)$ of the objective lens.
In case of WPOA, only the imaginary part of phase distortion function contributes to the image intensity, and therefore the eq.1.10 simplifies to:

$$T_{WPOA}(q) = A(q) \cdot E(q) \cdot 2\sin(\chi(q)) \tag{1.19}$$

According to eq.1.11, spherical aberration C_S and defocus Δf are the principal parameters influencing $\chi(q)$. Fig. 1.6 shows the phase distorting termsin$(\chi(q))$ of the transfer function of a conventional 300kV TEM with a spherical aberration $C_S = 0.64$ for different defocus values Δf. Negative values at lower spatial frequencies mean that electron waves within this range of spatial frequencies will experience

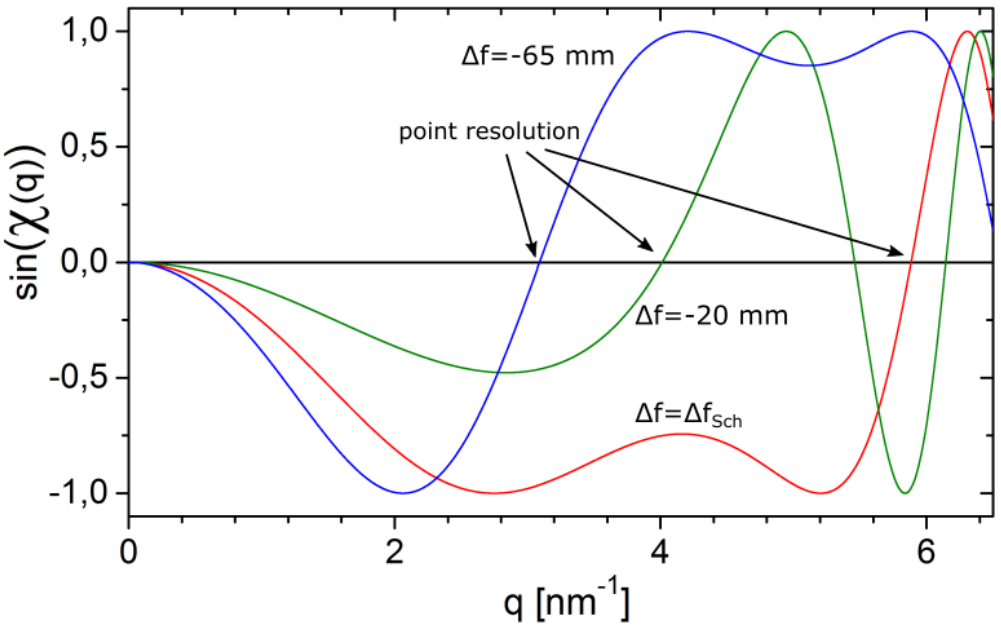

Figure 1.6.: Imaginary part of phase-distortion function for the 300 kV TEM with fixed spherical aberration parameter$C_S = 0.64$ mm at different defocus Δf values. For the green curve $\Delta f = -20$ nm, for the blue curve $\Delta f = -65$ nm, for the red curve $\Delta f = -\Delta f_{Sch}$. The point at which curve crosses the zero-axis corresponds to point resolution at given defocus value.

phase shift of $-\pi$ and result in dark atoms on on the bright background on the final image. For higher spatial frequencies (small distances of the image), the function oscillates faster, which means that the phase shift will change from negative to positive rapidly. This makes the contrast of the images not interpretable. Therefore, the point at which the transfer function crosses the zero-axis, essentially defines the minimum interpretable spacing of the image. The defocus value, at which the widest range of spatial frequencies is transferred to the image, was calculated by Scherzer: [28]

$$\Delta f_{Sch} = -1/2(C_S\lambda)^2 \tag{1.20}$$

On the fig.1.6 $\sin(\chi(q))$ function with $\Delta f = \Delta f_{Sch}$ is shown by the red curve. In this case the transfer function amounts as -1 for a wide range of frequencies. The maximum resolved spatial frequency at Scherzer defocus for a 300kV TEM with a spherical aberration $C_S = 0.64$ is 5.9 nm^{-1}, which corresponds to point resolution of approximately 1.7Å. The same $\sin(\chi(q))$ function at Scherzer defocus (on a larger scale of spatial frequencies q) together with the envelope function $E(q)$ and the result of the product of these two functions $T(q)$ at Scherzer defocus are shown on fig. 1.7 in cyan, black and blue colors, respectively.
Another difficulty is related to contrast delocalization R. It means that the wave function emitted from a point at the exit surface of the specimen is delocalized in the image plane. At a given position in the image delocalized waves from several

points from the specimen will superimpose, resulting in image artifacts.
R is expressed by:

$$R = max \left| \frac{1}{2\pi} \frac{\partial \chi(q)}{\partial q} \right|, \; q \in [0; q_{max}] \tag{1.21}$$

Lichte showed that the optimum conditions to minimize the delocalization are achieved at a certain defocus: [34]

$$\Delta f_{Lichte} = -0.75 C_S \left(\frac{q_{max}}{\lambda} \right)^2, \tag{1.22}$$

where q_{max} – is a maximum transmitted spatial frequency, which is given by the information limit of the microscope or the objective aperture cut-off.

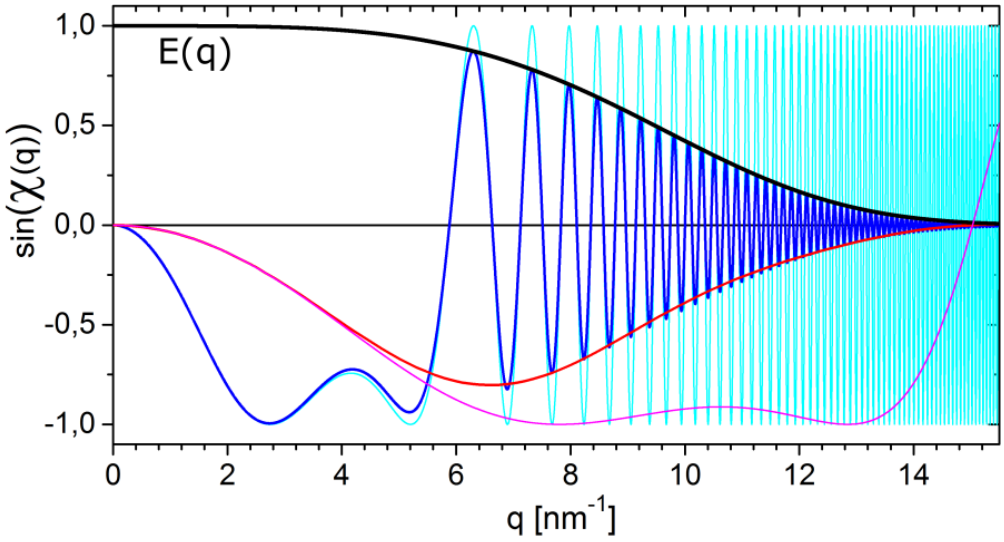

Figure 1.7.: Transfer function of 300 kV TEM in weak-phase object approximation at Scherzer defocus. Black line illustrates the envelope function $E(q)$(1.13) for a focal spread of $\Delta = 3$ nm. Cyan line illustratessin$(\chi(q))$ for spherical aberration parameter$C_S = 0.64$ mm, and magenta – $\sin(\chi(q))$ function for C_S^{opt}=13 µm. Blue and red lines illustrate transfer function $T(q)$, which is a product of envelope function $E(q)$ with respective phase-distortion functions $\sin(\chi(q))$.

Aberration correction

As we have seen the spherical aberration of image forming lens is a detrimental parameter that reduces the point resolution of the microscope. Nowadays there is a possibility to extend point resolution and decrease the impact of lens aberrations. This can be done by introducing a unit, that consists of several multipole correctors, after the objective lens, as it was shown by Rose [35]. This unit corrects the most detrimental parameters of the lens system, such as spherical aberration C_S, axial coma, 3-fold astigmatism, star-aberration e t.c. [36] In modern microscopes

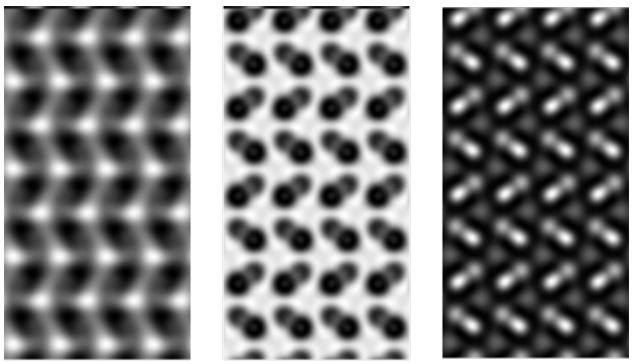

Figure 1.8.: Multislice simulation of AlN crystal along [11$\bar{2}$0] projection, illustrating the effect of spherical aberrationC_S correction in HRTEM. a) Conventional microscope withC_S = 0.64 mm and $\Delta f = \Delta f_{Sch}$; b) Aberration-corrected microscope with C_S^{opt} = 13 µm and $\Delta f^{opt} = -5.8$ nm; c) Negative C_S imaging conditions: $C_S^{opt} = -13$ µm and $\Delta f^{opt} = +5.8$ nm;

with correcting lenses it is possible to adjust the spherical aberration coefficient to any value. Lentzen et.al. showed that it is possible to tune spherical aberration coefficient C_S and defocusΔf to optimal values, when Scherzer condition of maximum phase-contrast and Lichte condition of minimum contrast delocalization are simultaneously satisfied. [37]

For the aberration-corrected FEI Titan 80–300 electron microscope operated at 300 kV accelerating voltage and with an information limit of $q = 12.5\ nm^{-1}$, which we use for high-resolution imaging in this study, such values are: $C_S^{opt} = 13\mu m$, $\Delta f_{opt} = -5.8$ nm. The effect introduced by aberration correction is shown on fig. 1.7. The magenta curve represents the $\sin(\chi(q))$ with optimal values C_S^{opt} and Δf_{opt}. The red curve is a result of product of $\sin(\chi(q))$ with the envelope function. In this case, the CTF crosses the zero-axis at the information limit $q = 12.5\ nm^{-1}$, meaning that the point resolution of 0.8 Åis achieved. The contrast delocalization R at these optimum conditions amounts to approximately 0.4 Å.

The effect of aberration correction on HRTEM imaging of AlN crystals is illustrated in multislice simulation images on fig. 1.8. In the case of a not-corrected microscope (fig.1.8(a)), neighboring Al and N columns can not be resolved separately in the [11$\bar{2}$0] projection, as if their projected distance (approximately 1.1 Å) is smaller than the point resolution of the microscope. In the case of an aberration corrected microscope (fig.1.8(b) and (c)), Al and N atomic columns can be easily identified.

Another advantage of a tunable spherical aberration coefficient C_S was described by Jia et.al [38, 39] and resulted in a development of new imaging method called negative spherical aberration imaging (NCSI). Usually, in a conventional microscope the spherical aberration C_S is fixed at a positive value. For thin samples with a small under-focus ($\Delta f < 0$), this results in a atomic columns appearing dark on a bright background (fig.1.8(b)). If the negative value of C_S is applied in a combination with

a slight over-focus, the atomic columns will appear bright on the dark background (fig.1.8(c)). One of the main advantages of using NCSI method is the increased absolute contrast of atomic columns in comparison with positive C_S imaging, due to constructive superposition of linear and non-linear terms of contrast forming function. [38]
Besides, Jia et.al shown that NCSI method result in the linear dependence of intensity of atomic columns on their atomic number. [39]It means that applying the negative C_S method it is possible to detect even light elements, such as, for example oxygen.

1.2.3. Diffraction contrast imaging

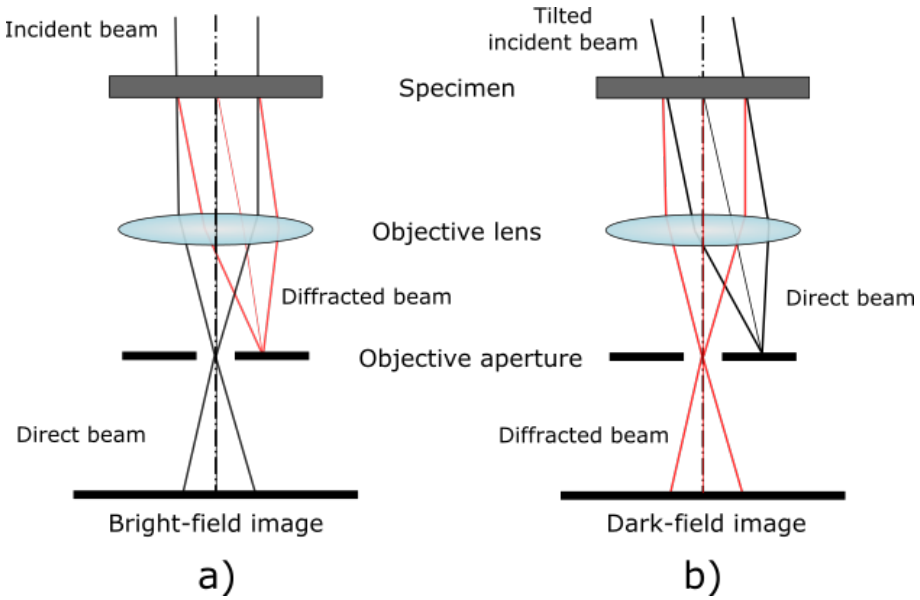

Figure 1.9.: Basic principle of diffraction contrast imaging. a) Bright-field imaging conditions. The incident beam is parallel to optical axis of microscope, which is denoted by dashed-dotted line. b) Dark-field imaging conditions.The incident beam is tilted, the diffracted beam is parallel to optical axis and passes through objective aperture.

For analysis of structural defects we use diffraction contrast. In this case imaging conditions are chosen so that only one set of lattice planes is in Bragg condition and therefore only one diffracted beam is excited strongly (two-beam conditions). If an objective aperture is placed in the back focal plane of the objective (c.f. fig.1.9 (a) and (b)) and the transmitted beam, parallel to optical axis of the microscope, passes through the objective aperture the (i.e $\vec{k} = \vec{k}_0$) a two-beam "bright-field" (BF) image is formed. If the incident beam is tilted with respect to the optical axis by an angle so that the diffracted beam with $\vec{k} = \vec{k}_g$ passes parallel to the optical axis through the objective aperture a "dark-field" (DF) image is formed.

When a lattice defect is present it causes a local distortion of lattice planes and therefore influences the intensity of diffracted beam, that corresponds to this set of lattice planes. We can use diffraction contrast imaging to analyze the nature of crystalline defects. By recording several dark-field images with different reflections g, we may find certain conditions at which dislocation is out of contrast. This indicates that the diffraction vector $\vec{g}$ and burgers vector of dislocation $\vec{b}$ are perpendicular to each other and the criterion $\vec{g} \cdot \vec{b} = 0$ holds. Therefore, by finding such diffraction vectors, we can determine the burgers vector of dislocation.
If the specimen is aligned along a particular zone-axis, the intensity of all diffraction spots is uniform for a complementary set of planes. Such conditions are called as many-beam (or multiple beam) conditions diffraction imaging.
Friedel's law states that the intensity of the beam diffracted in the direction $\vec{k}_g$ for an incident beam along $\vec{k}_0$ is equal to the intensity of the beam diffracted in the direction $-\vec{k}_g$ for an incident beam propagating along $-\vec{k}_0$. In other words, if we have a set of planes (h, k, l), than the intensity formed due to diffraction from this set of planes should be equal to the intensity of the image formed due to diffraction of complementary planes $(\bar{h}, \bar{k}, \bar{l})$:

$$I_{(h,k,l)} = I_{(\bar{h},\bar{k},\bar{l})} \tag{1.23}$$

Friedel's law only holds under kinematic diffraction conditions, i.e. when we assume that the incident electron beam is diffracted only once while passing through the specimen. Under these imaging conditions Friedel's law is strictly fulfilled and it is impossible to determine whether an inversion center is present in crystal. Based on theoretical calculations of the diffraction contrats, Serneels et al., [40] could show that the intensity of two adjacent domains of the crystal, related to each other by inversion operation, is complementary for dark fields images formed with g = (hkl) and g = (-h-k-l) in multiple beam imaging conditions.
Previously we have discussed that wurtzite crystallographic structure is non-centrosymmetrical, and (0002) planes are not equal to $(000\bar{2})$ plane. Romano et.al was the first who experimentally demonstrated the possibility to detect ID in GaN films by taking advantage of Friedel's law failure. [41] Fig.1.10 (a) and (b) show the diffraction patterns of AlN along $[11\bar{2}0]$ and the dark-field images formed, when the objective aperture is placed around $g = (0002)$ and $g = (000\bar{2})$, respectively. We observe the complementary intensity between the columnar domain and adjacent surrounding matrix. Besides, contrast reversal for these columnar domains is observed on dark-field images at two different imaging conditions. This a clear indication of the crystallographic domain which is related by inversion operation to the surrounding matrix. This method is useful for imaging inversion domains on the large scale, however it does not provide the information on the polarity of the inversion domains.

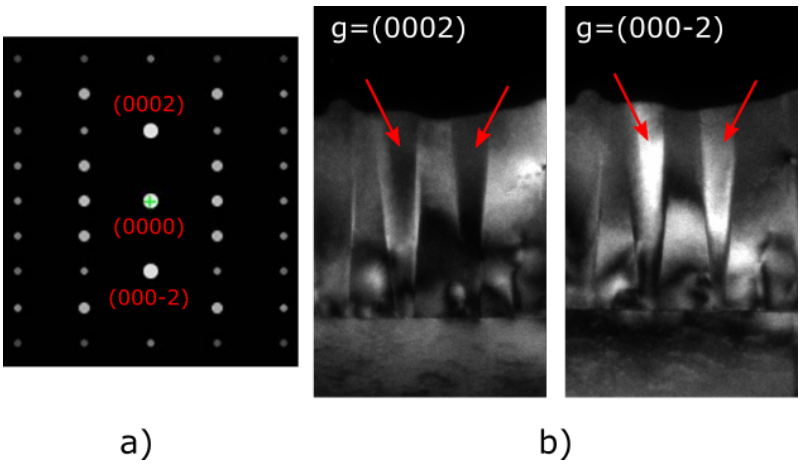

Figure 1.10.: Imaging inversion domain in AlN layers using many-beam dark-field imaging conditions. a) Diffraction pattern of AlN in $[11\bar{2}0]$ projection. b) Dark-field images taken with $g = (0002)$ and $g = (000\bar{2})$, respectively. Red arrows indicate the domains with reversed contrast, characteristic for crystalline inversion domains.

1.2.4. Moiré patterns

Moiré pattern arises from the interference of diffracted beams from two set of planes with the close inter-planar distance. Fig.1.11 (a) schematically shows the appearance of Moiré fringes from two sets of lines with a small misfit between them. The simple misfit between two set of planes gives rise to a translational Moiré pattern, and the distance D between the Moiré fringes is related to the distances d_1 and d_2 between original planes. Since the distance D is much larger then that of the corresponding lattice planes d_1 and d_2 they result from, by measuring the distance of Moiré fringes we can obtain useful structural information about the lattice planes even if the microscope resolution is not high enough to resolve lattice planes separately.
If $\vec{g}_1$ is the beam, diffracted from the first set of planes , and $\vec{g}_2$ is the beam diffracted from the second set of planes, then the reciprocal spacing between them is given by:

$$\vec{g}_M = \vec{g}_2 - \vec{g}_1 \tag{1.24}$$

And the distance between corresponding Moiré fringes in the real space is given by:

$$D = \frac{d_1 d_2}{d_1 - d_2} \tag{1.25}$$

The formation of Moiré fringes is a particular case of "double-diffraction". In a simplified way we can imagine that beam $\vec{g}_1$, generated by the diffraction of the incident beam $\vec{k}_0$ by upper set of planes, then act as an incident beam for the lower set of planes generating beam $\vec{g}_2$. Therefore on the diffraction pattern in TEM each reflection, corresponding to $\vec{g}_1$, will act as a central reflection of an incident beam

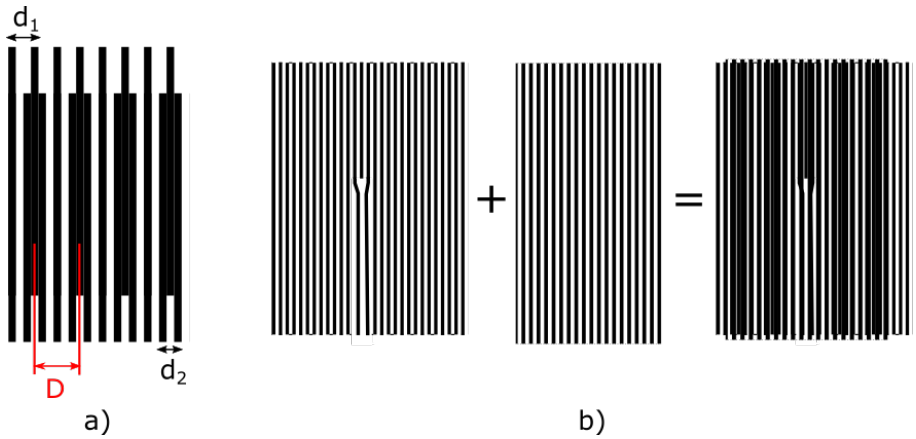

Figure 1.11.: Schematic representation of Moiré pattern formation.a) Translational Moiré fringes: d_1 and d_2 are interplanar distances of original lattices, D is the distance between Moiré fringes. b) Example of a dislocation image formed on Moiré by interference between a regular lattice and one containing an extra half-plane.

for the reflections $\vec{g}_2$ and the diffraction pattern of second crystal will be produced around each reflection $\vec{g}_1$ of the first crystal.
We can also use Moiré patterns to reveal dislocations present in one of the lattices. If the lattice contains an inserted half-plane due to the presence of a dislocation, the interference with another regular lattice will give rise to a terminated Moiré fringe, as it is illustrated on the fig. 1.11 (b). The projected Burgers vector of the dislocation can be directly determined from the images of Moiré patterns with a terminated fringes. [28]

1.2.5. Scanning TEM and Z-contrast imaging

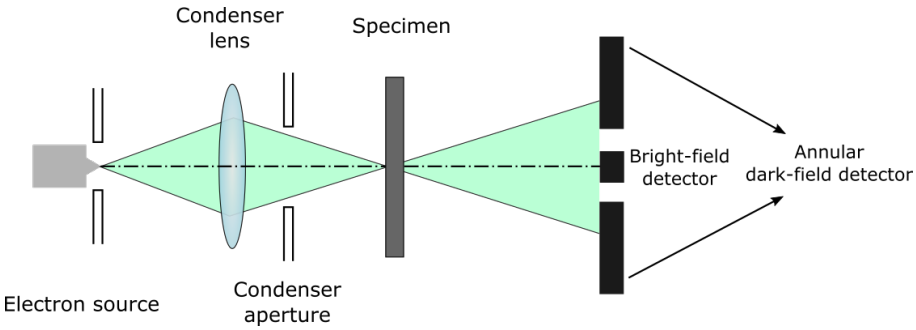

Figure 1.12.: Basic principle of image formation and signal collection in STEM. The horizontal dashed-dotted line illustrates the optical axis of the microscope.

The principle difference between the TEM techniques, described above, and scanning transmission electron microscopy (STEM) is that in the latter case the optical

lens system forms the convergent focused beam (probe) before the beam enters the specimen. The probe is then scanning across the area and the image in STEM mode is formed by collecting a signal, generated due to interaction of electron beam with the specimen at each scanning point. If the scattering angle is low (10-20 mrad), the signal is collected by a bright field detector. The collected signal in this case includes contributions from incoherently scattered electrons and coherent Bragg scattering, therefore strong phase contrast arises on the images.
Electrons, scattered at higher angles (several tens of mrad) are collected by high-angular annular dark field (HAADF) detector. Nowadays HAADF-imaging is the most widely used technique in STEM analysis. At high scattering angles the amplitude of Bragg scattered electrons becomes weak, and the scattering intensity will essentially follow the Rutherford scattering model and be proportional to Z^2, where Z – atomic number of the scattering atom. [42]
When we consider scattering at a periodic crystal potential, rather than on a single atom, the dominating scattering mechanism at high angles arises from thermal vibrations of the atoms around their equilibrium positions (phonons) and also known as thermal diffusive scattering (TDS).
In TDS the intensity is given by: [43]

$$I^{TDS}(s) = \left(f^e(s)^2\right)\left[1 - exp(-2Ms)\right], \tag{1.26}$$

where M– is a temperature-dependent Debye-Waller factor; $s = \frac{sin\theta}{\lambda}$ – scattering parameter; $f^e(s)$ – is the atomic form factor of electron scattering, proportional to atomic number Z. [44]
As we see, the major advantages of HAADF-STEM technique is that for the large scattering angles it is incoherent, thus the phase contrast is suppressed, and the intensity is highly dependent on the atomic number Z of the scattering atoms. This is the reason why this method is also often called "Z-contrast imaging". In general, on HAADF-STEM images heavier atoms will appear at higher intensity, while lighter atoms – at lower intensity. However, the direct analysis of composition from HAADF-intensity is not possible, because the intensity depends on temperature and the strength of atomic vibrations and channeling effects. Electron channeling occurs when an electron beam is focused on an atomic column and the electrons are attracted by electrostatic potential and channel along the column close to the atomic nuclei, resulting in strong scattering probability and increased intensity. Various defects, such as dislocations, strain, lattice distortions may disrupt the electron channeling and result in change of HAADF-contrast, however their influence on the image is not intuitively predictable.
Thus, despite of the fact that Z-contrast images can be directly interpreted, in some cases the use of simulations is necessary. The most widely-used simulation method was developed by Kirkland and is called "frozen phonon" approach. [45] It is based on the idea that electron, when it passes through the sample, will see a vibrating lattice in a fixed configuration, because the vibration period of the lattice is smaller than the time in which electron transits the specimen. This means that

each electron encounter different lattice configuration. Therefore, several multislice calculations can be performed, considering the number of configurations of lattice thermal displacements and the total intensity will be a summation over the intensities in these configurations.
In order to compare the experimental HAADF-intensity with frozen phonon simulations, the measured raw intensity (I_{raw}) should be normalized to the intensity of the incident electron probe (I_{probe}): [46]

$$I_{normalized} = \frac{I_{raw} - I_{vacuum}}{I_{probe}}, \tag{1.27}$$

where I_{vacuum} is the intensity of the signal on the detector signal, when the electrons are not scattered on the detector at all. The intensity I_{probe} of the probe is the signal measured on the detector, when the not scattered direct electron beam is placed on it.
Because the HAADF-imaging is incoherent, as we have mentioned before, the collected intensity will be a result of convolution between the intensity of the STEM probe $P(\vec{r})$ (also known as point spread function) and object function $O(\vec{r})$, which defines the fraction of intensity, scattered by each atom on detector:

$$I_{HAADF}(\vec{r}) = P(\vec{r}) \otimes O(\vec{r}) \tag{1.28}$$

Therefore, spatial resolution in STEM is essentially defined by the the point spread function $P(\vec{r})$, or, in other words, by the diameter of the electron probe.
The spatial resolution in STEM thus is mainly limited by the aberrations of the probe forming lens, which have same imperfections as the objective lens, discussed in the previous section. For a 300 kV STEM at optimum conditions and a spherical aberration of the probe forming lens of $C_S = 1.2$ mm a spatial resolution of 1.3 Å can be achieved.
As for the objective lens, it is also possible to mount a correcting lens between the condenser lens and the specimen to reduce the aberration coefficient of the lens, thus decreasing the probe size. [47] Recently, it was demonstrated that by using the corrector for the third and fifth order spherical aberration and introducing cold field-emission gun to reduce the chromatic aberration, it is possible to reduce the spatial resolution in STEM down to 0.5 Å. [48, 49]

1.2.6. Electron energy-loss spectroscopy

Electron energy-loss spectroscopy (EELS) is an analytical technique, implemented into the TEM, that allows to perform structural and chemical analysis of the very small sample volumes with high energy and spatial resolution. In EELS the kinetic energy of the incident electron beam is measured after its inelastic interaction with the specimen. Inelastic scattering arises from the Coulomb interaction between electron from incident beam and atomic electrons.

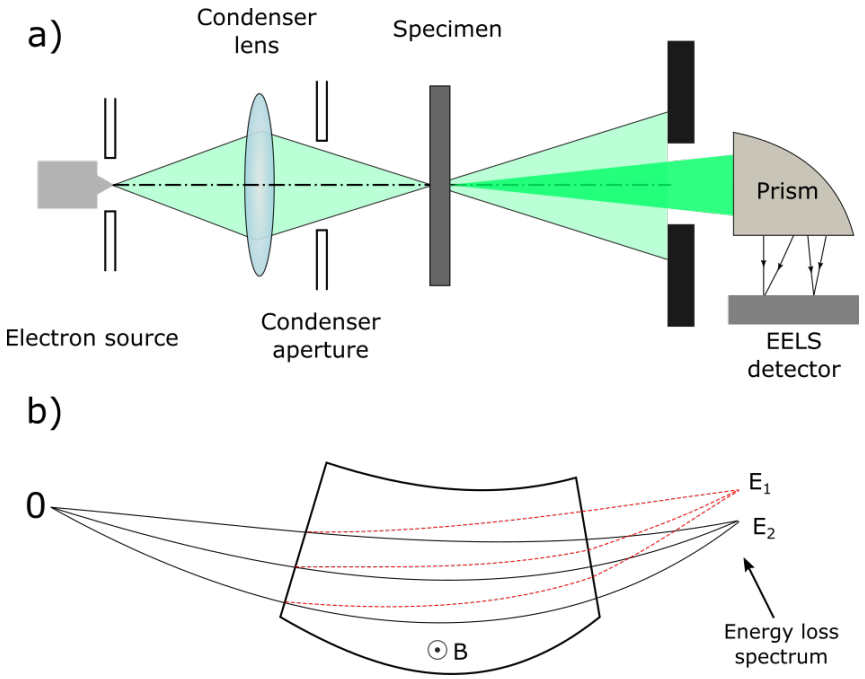

Figure 1.13.: Basic principle of EELS. a) Schematic representation of signal acquisition in combination by EELS and HAADF-STEM detector. b) Basic principle of magnetic prism. Electrons are deflected in magnetic field B at different angles, proportional to their initial energy. At the exit of the magnetic prism the electrons are collected by EELS detector that records the energy spectrum.

EELS instrumentation is based on a magnetic prism (fig.1.13), whose working principle resembles the white light dispersion in a glass prism. The electrons transfer through uniform magnetic field B, following the circular path with radius R. The force acting on the electron is $F = Bev = \frac{mv^2}{R}$, where e, v and m are electron charge, speed and relativistic mass of an electron. Therefore the radius of electron path depends on the electron speed v, i.e. on its kinetic energy:

$$R = \frac{mv}{Be}$$

A magnetic prism also focuses the electrons, that deviate from the optic axis, to a single image point, if they originate from the same point object.
In this work we used a EELS spectrometer installed in a scanning transmission electron microscope (STEM) (fig.1.13 (a)). In this system the field emission source and multipole lenses are used to form a small probe. The corrector allows to correct spherical aberrations of the probe-forming lens and focuses the electron beam into a probe below 1 Å. In such system transmitted the electrons scattered at relatively large angles are collected by an annular detector, while electrons inelastically scattered at lower angles are collected by the EELS detector. It allows to produc both, HAADF images of the specimen and EELS spectra data of the same specimen region simultaneously.

In typical EELS spectrum three principal energy ranges can be distinguished. First peak is the most intensive and occurs at 0 eV ("zero-loss" peak). This peak originates from electrons that did not undergo inelastic interaction with specimen. The width of the zero-loss peak usually indicate the energy distribution of electron source and thus energy resolution of the system can be estimated.
Energy region between 0 eV and approximately 50 eV is called "low-loss" region. Low-loss features arise from inelastic interactions of electron beam with electrons of conduction and valence band, which is useful to study electronic properties of semiconductor and insulator materials.
The high energy-loss spectrum (above ∼50 eV) contains information from inelastic interaction of electron beam with core-shell electrons. In a solid specimen the core-shell ionization occurs due to transition of core-electron to the empty energy state above Fermi level. The core-shell excitation gives rise to ionization edges, that are superimposed on a rapidly decreasing background on the EELS spectrum. The energy-loss of the incident electron beam is equal to binding energy of the core-shell electron, which is characteristic for each chemical element and for each electron shell. Therefore, the ionization edges may be used for identification of elements present in the given region.

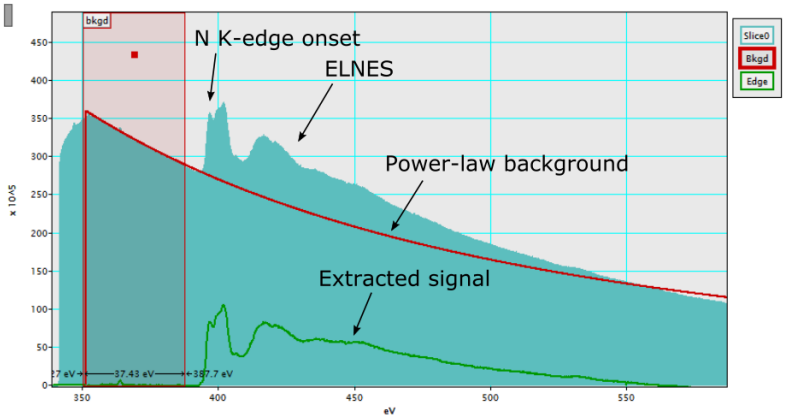

Figure 1.14.: Example of as-recorded EELS spectrum of AlN. In the energy range of 340-585 eV N K-edge is detected. Red line displays the extrapolated power-law background. Green line corresponds to the EELS signal after background subtraction.

In this work we applied EELS to conduct elemental-composition analysis of AlN layers grown on Al_2O_3 substrates. Fig.1.14 shows the example of an EELS spectrum of AlN in the energy range 340-585 eV, where the N K edge is indicated. For elemental analysis the background of a particular element edge should be extrapolated using a power-law energy dependence and subtracted. The saw-tooth shape of the ionization edge with rapid rise and monotonic decay is typical for K-edges. The intensity oscillations beyond approximately 50 eV of the edge onset are called energy-loss near-edge structure (ELNES). They arise from the solid-state effects and

contain rich information about how atom is bonded, its coordination and density of states.
For compositional analysis the core-loss intensity should be integrated over an energy range of Δ=50 eV beyond the edge onset, which will result in averaging the contribution of near-edge structure. The areal density N of element within the given area will be: [50]

$$I_c(\beta, \Delta) \approx N I_1(\beta, \Delta)\sigma(\beta, \Delta), \tag{1.29}$$

where $I_C(\beta, \Delta)$ – the intensity of the core-loss signal collected within the semi-angle β and integrated over an energy range of Δ; $\sigma_c(\beta, \Delta)$ – is a partial cross-section of element, calculated for core-loss scattering up to a collection semi-angle β and energy range Δ beyond the edge onset; $I_1(\beta, \Delta)$ – is an integral of low-loss spectrum including zero-loss peak.
The concentration of the given element n is defined by $\frac{N}{t}$, where t – is local specimen thickness
In this work we apply equation 1.29 to find the concentration ratio of two elements. This allows to cancel the contributions of low-loss spectra region$I_1(\beta, \Delta)$ and the specimen thickness t:

$$\frac{n^A}{n^B} = \frac{N^A}{N^B} = \frac{I_c^A(\beta, \Delta)}{I_c^B(\beta, \Delta)} \times \frac{\sigma_c^B(\beta, \Delta)}{\sigma_c^A(\beta, \Delta)}, \tag{1.30}$$

1.2.7. Experimental details

Plan-view and some diffraction contrast TEM images are performed in a JEOL 2010 FEG microscope operating at 200 kV (λ=2.51 pm) with an information limit 7.1 nm^{-1} and a point resolution of 0.194 nm. For HRTEM investigations a FEI Titan 80-300 operating at 300 kV (λ = 1.97) with an aberration corrector for the objective lens is used. The information limit of FEI Titan 80-300 is 12.5 nm^{-1} and thus the point resolution of 0.8 Åcan be achieved. For high-resolution TEM imaging, the spherical aberration is tuned to a slightly negative value of $C_s = -13\mu m$ and the images are recorded with an over-focus of + 5.8 nm. The HRTEM images presented in this work are composed of several (typically around 10-20) HRTEM images, which are recorded continuously with identical imaging conditions. After a drift correction, occurring during the image acquisition, the intensities of the single images are summed up and the intensity of the resulting image is normalized.
HRTEM images are compared with simulated contrast patterns based on known structural models. HRTEM patterns simulations are performed using the multi-slice approach [51, 45] with a self-developed software. The phase plates and Fresnel propagator were calculated using the EMS software package [52]. The simulation parameters corresponding to the experimental conditions are used: acceleration voltage 300 kV, a semi-convergence angle 0.3 mrad, a defocus spread 2.9 nm, a spherical aberration $C_S = -13$ µm, and a slight over-focus of 5.8 nm. The contrast patterns for AlN and Al_2O_3 in two principal projections $[11\bar{2}0]$ and $[10\bar{1}0]$ for the specimen thickness of approximately 6 nm are shown on fig. 1.15 (a) - (d).

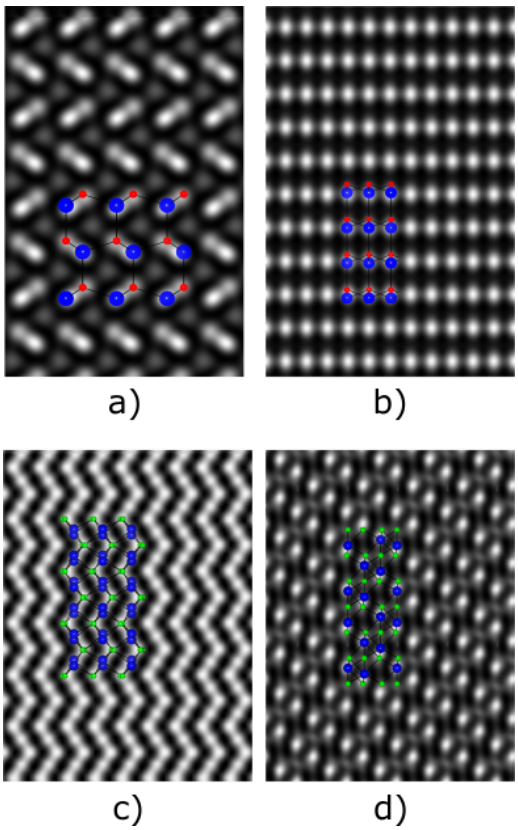

Figure 1.15.: Multi-slice simulation images of AlN and Al_2O_3 in two principle projections for thickness $t \approx$ 6-7 nm. a), d) $[11\bar{2}0]$ and b), c) $[10\bar{1}0]$. The ball-and-stick models of the respective structures are superimposed on simulation images.

The in-situ experiment, discussed in 2, is performed using a Protochips Atmosphere TEM holder and Protochips heating chips. Heating of the sample is realized by resistive heating of a 120 nm thick ceramic SiC membrane, which acts also as the specimen support. The temperature dependent resistivity of the SiC membrane is used to control the temperature of the heating membrane. The sample is observed through holes of the SiC membrane during the experiment.
HAADF-STEM imaging is also performed with a FEI Titan 80-300 operating at 300 kV. Convergence semi-angle of the incident electron probe is 9.0 mrad and a spherical aberration parameter of probe forming lens is $C_S = 1.2$ mm, which results in a spatial resolution of 1.3 Å. The acceptance semi-angle of annular dark field detector (Fishione model 3000) is 35 mrad. In some cases, to improve the signal to noise ratio on the HAADF-STEM images, different image sections showing identical features are superimposed. STEM image simulations are performed by a parallelized multi-slice approach using the frozen-phonon approximation with a total number of 30 different frozen-phonon configurations.
In the $[11\bar{2}0]$ projection the bond length of Al-N dumbbell is 1.1 Å(fig. 1.16 (a)), therefore the spatial resolution of 1.3 Åis not sufficient to resolve Al and N atomic

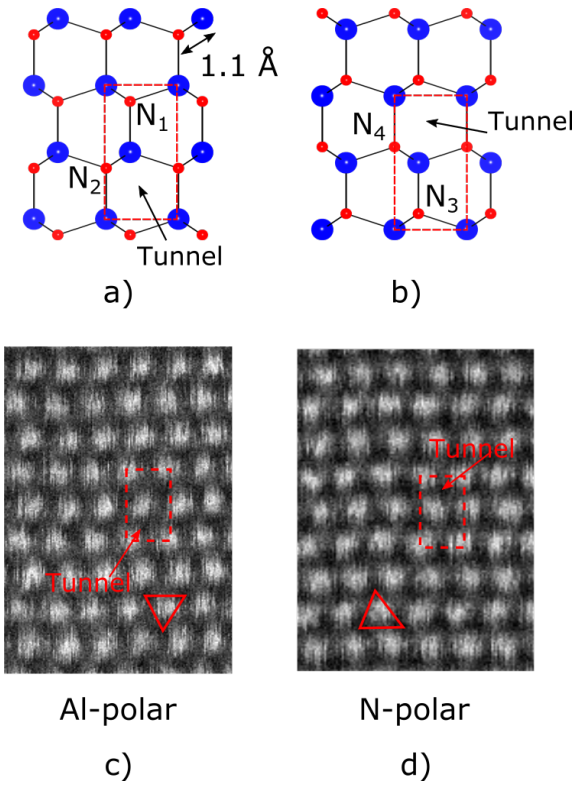

Figure 1.16.: Determination of wurtzite (AlN) polarity in HAADF-STEM images by locating tunnel positions. a) and b) AlN balls-and-sticks schemes in the [11$\bar{2}$0] projection in Al-polar and N-polar orientations. AlN unit cells are shown in red dashed rectangulars. N_1, N_2 and N_3, N_4 indicate the positions of N atomic columns. c) and d) Experimental HAADF-STEM images of AlN in the [11$\bar{2}$0] projection. The tunnel positions are indicated by arrows on both schematic and experimental images. Red triangles are constructed by connecting the tunnel positions around Al atomic column.

columns separately in a STEM mode of the FEI Titan 80-300 microscope, that we use in this work. As it is shown in fig. 1.16 (a) and (b), for Al-polar AlN N atomic columns are located either on the N_1 or N_2 sites, while for N-polar AlN, N atomic columns are located on N_3 or N_4 sites. On the experimental images N atomic columns give a broad diffuse contrast and therefore it is hard to locate on which site the N-column is located and thus determine the polarity of the film. (fig. 1.16 (c) and (d)) Rouviere et.al. [53] have suggested an easier and more precise method, which implies comparing the contrast of areas below and above the Al atomic column. In the case of Al-polar AlN, the area below Al atomic column is a tunnel and above it – N atomic column in N_1 site. In the case of N-polar AlN the situation is reversed and the sequence is: N-column on N_3site, Al column, the tunnel. Therefore, by locating the tunnel positions on the experimental images we are able to determine the polarity of the film. In order to make it more representative, we

can connect the tunnel positions around one Al atoms. Then, the vertices of the resulting triangle will be facing down for Al-polar AlN, and facing up for N-polar AlN.
High-resolution HAADF-STEM and EELS investigations, presented in this work, are performed with NION Ultrastem microscope operating at 200 kV with a cold FEG as an electron source the probe correction system, providing the spatial resolution 0.7 Åand energy resolution (full-width-at-half-maximum of a zero-loss peak) of EELS measurements of 0.28 eV. The values of convergence and collection semi-angles remained constant for each experiment and are 28 mrad and 24 mrad, respectively. In this case, the spatial resolution is sufficient to resolve Al and N atomic columns separately and polarity of AlN films can directly analyzed. EELS measurement are performed with a fast acquisition mode (171.15 spectra/sec) and low probe current (50-80 pA) conditions during acquisition. This allows to suppress the effect of strong radiation damage of the specimen while maintaining high spatial resolution, however decreased signal-to-noise ratio during acquisition of the EELS spectra. The EELS data evaluation is made with Gatan Microscopy Suite software (ver. 3.11).

1.3. Sample growth by metal organic vapor phase epitaxy (MOVPE)

Metal-organic vapor phase epitaxy (MOVPE), also know as metal-organic chemical vapor deposition (MOCVD), nowadays is a most widely used technique for epitaxial growth of III-V and II-IV semiconductor compounds. The structures grown by MOVPE are used for wide range of electronic and optoelectronic devices, such as light emission diodes (LEDs), lasers, solar cells, high electron mobility transistors (HEMT) e t.c. MOVPE has several advantages as compared to other epitaxy methods. It allows to obtain hetero-epitaxial structures with abrupt interfaces and a high degree of uniformity. The MOVPE technic is highly versatile, which makes it suitable for production of almost every type of III-V and II-IV compounds and alloys. This, together with the possibility to achieve high growth rates and large-scale production, makes MOVPE indispensable for industrial applications.
In this section we will first briefly discuss the principal theoretical aspects of MOVPE method, such as thermodynamic driving force of growth and kinetic processes taking place during deposition. For more detailed information the reader is invited to specialized literature given in ref. [54, 55]. Then we will underline specific issues concerning the MOVPE growth of group III-nitride semiconductors and, finally, specify the experimental conditions used in our studies.

1.3.1. Theoretical principles of MOVPE

Very general consideration of MOVPE growth implies a following categorization of growth limiting processes, depending on the temperature [56]: surface kinetics lim-

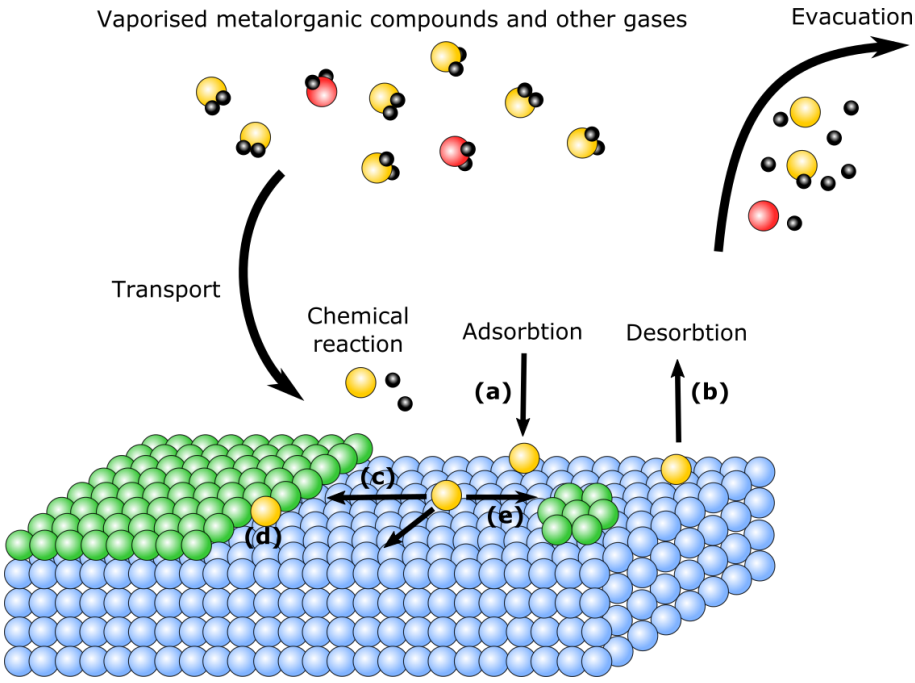

Figure 1.17.: Simplified representation of basic processes of MOVPE growth. For detailed explanation of individual steps see text.

ited growth, mass transport limited growth and thermodynamically limited growth. Let us now briefly discuss each of these factors, influencing the growth process in MOVPE. The general schematic representation of the processes occurring during MOVPE growth is given in fig. 1.17, to which we will refer in the course of following description.

1) Thermodynamically limited growth Thermodynamic limits the maximum growth rate of the system and determines the driving force of the growth process. During MOVPE growth vapor and condensed phases, including solid phases of the growing material are in thermodynamical equilibrium. A thermodynamical system is in equilibrium when the Gibbs free energy G is at minimum. The change of a free energy of a thermodynamic system with respect to the change in the number of atoms or molecules of the species, that are added to the system, is called the chemical potential μ. Therefore, in terms of chemical potentials μ of each component of the system, the equilibrium condition of the minimum of Gibbs free energy will be: [54]

$$\Delta\mu = \mu^i_{vapor} - \mu^i_{solid} = 0$$

During growth the vapor phase is transformed into a solid, i.e. the equilibrium condition is not satisfied. Therefore a non-equilibrium situation at which $\Delta\mu \gg 0$ (supersaturation) is created that drives the system to produce the solid. The phase transformation driving the growth will stop when the system again reaches the equilibrium state with $\Delta\mu = 0$.

The maximum quantity of this solid that can be produced is the amount that would establish equilibrium ($\Delta\mu = 0$) and thus is fundamentally limited by thermodynamics.
For an ideal gas mixture the difference in chemical potentials is: [54]

$$\Delta\mu = RTln\frac{p}{p_0},$$

where and p – is the partial pressure of the gas, and p_0– is the equilibrium or saturated vapor pressure.
The phase transition from gaseous to solid state is an exothermic process, therefore its rate decreases as the temperature grows.
In hetero-epitaxial growth, when the material of the film and substrate are different, the change in surface free energies of substrate and film play an important role, as they modify the difference in chemical potential driving the growth.

$$\Delta\mu^* = \Delta\mu - \Delta\gamma,$$

where $\Delta\gamma = \gamma_f + \gamma_{if} - \gamma_s$ and γ_f and γ_s – are the surface free energies of film and substrate respectively, γ_{if} – the surface free energy of the interface including the contribution of strain. The impact of surface free energies imply, for example, that if the contribution of strain is significant and the free energy of the interface γ_{if} is higher than free energies of the film and the substrate, the driving force for crystal growth disappears ($\Delta\mu^* = \Delta\mu - \Delta\gamma \leq 0$) and growth will not occur even at supersaturated conditions. On the other hand, if the free energy of film is smaller than free energy of substrate ($\gamma_f < \gamma_s$) and the strain and the interface free energy is negligible, the total surface free energy $\gamma \leq 0$ and the growth may occur even in undersaturated conditions. [57]
In the thermodynamically limited regime the growth rate may be limited by the reactant depletion on the vapor/surface interface, by surface desorption or re-evaporation.

2) Mass transport limited growth In the medium temperature range the growth rate is limited by mass transport, that governs the access of volatile precursors to the substrate and their diffusion throughout the vaporized boundary layer. Mass transport is closely linked to hydrodynamics, that controls the transport of precursors by the carrier gas towards the growing solid/vapor interface. The diffusion rate during mass transport does not depend on the substrate temperature, but mainly on the partial pressure of the input gases and the configuration of the MOVPE growth reactor, that defines the distribution of vortex and laminar flows within the chamber.
The mass transport limited mode is generally favored for the growth of III-V alloys, as it is cancels out the influence of temperature on the kinetic processes on the surface and, therefore, on the growth rate, and only depends on the flow rates of the gaseous species.

3) Kinetically limited Kinetics approach the actual processes and reactions that take place between two thermodynamical equilibrium states of a system with a minimum Gibbs free energy. These reactions occurring during MOVPE growth may be subdivided in two main categories: homogeneous and heterogeneous reactions.
Homogeneous reactions are chemical reactions between species within the gas phase. This includes the pyrolysis (decomposition at elevated temperatures) of cation and anion source molecules into ad-atoms.
Heterogeneous reactions – reactions that take place at the solid interface and involve interaction of vapor with the surface in solid phase.
Heterogeneous reactions include adsorption (fig.1.17(a)) desorption (fig.1.17(b)) of atoms from the surface.
Adsorption implies that a chemical bond is formed between the adsorbate and the surface. When the molecule reaches the surface it may be physisorbed — meaning that it binds to the surface only by weak, van der Waals forces. The physisorbed molecules can then either desorb or find a site where they can form a chemical bond to the surface as a result of surface migration. As a result of adsorption and migration, atoms incorporate into proper growth sites such as surface steps (fig.1.17(c)), kinks (fig.1.17(d)) or form independent clusters (islands) on the surface (fig.1.17(e)).
The rates of all kinetic reactions is product of concentration and the rate constant, that increase with the temperature T , following the Arrhenius law:

$$k = Ae^{-\frac{E_a}{RT}},$$

where E_a– is activation energy of the reaction.
Therefore, at a low temperature regime the growth rate is limited by low rate of chemical reactions, as well as low rate of surface migration and incorporation of atoms into lattice.

1.3.2. MOVPE growth of group-III nitrides

For the MOVPE growth of III-nitrides, and, particularily GaN and AlN which are the focus of this work, the metallic atoms are supplied in a form of metalorganic precursors: of trimethyl- and triethyl-gallium for Ga atoms, and trimethyl-aluminium for Al atoms. Ammonia gas (NH_3) is usually favored as a source of nitrogen atoms. [58]
In a simplified representation, the pyrolysis reaction of supplied metalorganic precursors of the group III elements (R_3III), taking place in III-N MOVPE growth is the following [59]:

$$R_3III(g) + 3/2H_2(g) \rightarrow III(g) + 3\,RH(g)$$

The reaction at the substrate surface that forms a binary nitride is:

$$III(g) + NH_3(g) \rightarrow III{-}N(s) + 3/2H_2(g)$$

From the thermodynamical predictions, NH_3 decomposes into H_2 and N_2 at a temperature above 300 °C, however it was shown that in the typical MOVPE growth environment decomposition rate of NH_3 is smaller and higher temperatures are required to promote ammonia decomposition. [60] Therefore, the decomposition reaction of NH_3 is:

$$NH_3(g) \rightarrow (1-\alpha)NH_3(g) + \alpha/2N_2(g) + 3\alpha/2H_2(g),$$

where α– is a mole fraction of decomposed NH3 at growth temperature.
One of the major problems in MOVPE growth of III-nitride compounds is related to high volatility of N species. At elevated temperatures, which are generally required for efficient ammonia decomposition and the growth of good quality GaN and AlN layers, the desorption rate N atoms from the growth surface increases. [61] It will result in lower N partial pressure and, in case of GaN, in formation of second liquid phase on the surface – GaN droplets. Therefore, in MOVPE growth of III-group-nitrides it is important to maintain particularly high V/III molar ratios of the supplied precursors.

1.3.3. Experimental set-up

Unless stated differently, all the samples, discussed in this work, are grown in a vertical MOVPE reactor built in CRHEA. C-plane 2" sapphire substrates are set onto a rotating graphite susceptor, which provides the surface homogeneity during deposition. The susceptor is heated by induction and the temperature is controlled by thermocouple. The rate of temperature ramp is fixed at 80 °C/min.
For in-situ control of the growth process, a reactor is equipped with laser reflectometry (LR) setup with the wave length of 633 nm. When the growing layers are mirror-like, the LR signal consists of periodic and constant amplitude oscillations with a period corresponding to a thickness variation of $\lambda/2n$ where n is the refractive index of the deposited material. The decrease of the LR indicates the surface roughening.
The growth is performed at atmosphere pressure. A mixture of H_2 and N_2 acts as a carrier gas and NH_3 gas is used as the N source. The flow rates of NH_3, H_2 and N_2 are 3.5, 5.0 and 3.0 slm respectively and are kept constant throughout all experiments.
Additionally, in some experiments a Si_xN_y coating is deposited by introduction of SiH_4 gas with the flow rate of 50 sccm. TMGa and TMAl are used for supply of Ga and Al atoms. Specific information on the substrate temperature during deposition, flow rates of metalorganic precursors and V/III ratios, as well as details on heteroepitaxial structures, are given in the respective chapters.

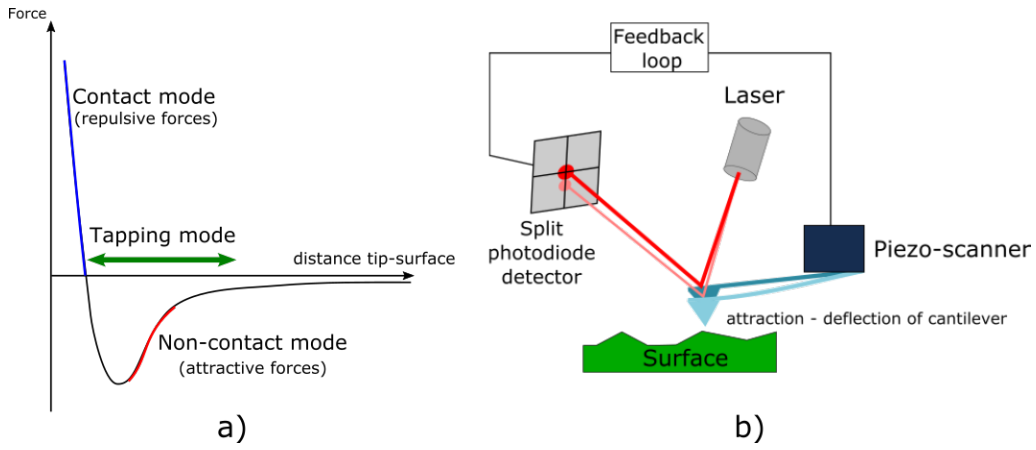

Figure 1.18.: Basic principle of AFM. a) Force response curve, illustrating the principle modes of AFM measurements. b) Scheme of AFM measuring system.

1.4. Atomic force microscopy

Atomic force microscopy (AFM) is a technique used for surface analysis of the material. The main principle of AFM is based on interaction forces between the sample surface and the sharp tip and the end of the cantilever, that provokes the deflection of the cantilever from its initial position. The length of the cantilever is usually 100-200 micrometers and the tip radius varies from 5 to 60 nm. Fig.1.18 (a) shows a schematic of a force response curve as a function of the distance between the tip of the cantilever and the sample surface. When the tip is approaching the surface the attractive Van der Waals force starts to act and the cantilever tip is deflecting towards the surface. This measurement mode is called “non-contact” mode. As the distance between tip and surface decreases, the Van der Waals force gradually increases until it reaches its maximum and the repulsive electrostatic forces start to act between the tip and the sample surface. The repulsive force increases very steeply as the tip further approaches the sample surface. The measurement mode in a repulsive force regime is called “contact” mode. The intermediate mode, when the sample is oscillating close to the sample surface, is called “tapping mode”. This mode allows to avoid sample and tip damage, often caused by using a contact mode, and allows to obtain higher vertical resolution and scanning speed than in a “non-contact” mode. [62]
In a “tapping” mode the cantilever is oscillating near to its resonance frequency with an amplitude of 20-100 nm. When the tip of cantilever encounters the variation of height on the surface caused by its roughness, it deflects from its initial amplitude of oscillation changes. This deflection is sensed by the detection system, schematically shown on fig.1.18 (b). The solid-state laser light reflects from the back of the cantilever and the reflection is detected by the segmented photodiode position sensitive detector (PSD). When the cantilever bends, the intensity of the reflected laser beam on the center of PSD decreases. The electronic feedback control system

applies the respective voltage to piezoelectric vertical scanner to keep the amplitude of cantilever oscillations constant. thus creating a "derivative" image of the surface. The computer system saves the values of amplitude variations of the cantilever and then software processes it into "topographic" image of the surface.
Lateral resolution of the AFM strongly depends on curvature and sidewalls angles of the cantilever tip and usually is about 1 to 5 nm. The vertical resolution is determined by the vertical scanner movement and may be less than 1 A in a "tapping" mode.
In our work we analyze the roughness of the sample surface. One of the most common measures to quantify the roughness of a surface is the Root Mean Square (RMS) Roughness given by the standard deviation of Z values from within a scanned area:

$$RMS = \sqrt{\frac{\sum_{i=1}^{N}(Z_i - Z_{ave})^2}{N}},$$

where Z_{ave}– average Z value within the given area, and N – number of points.
In this work AFM measurements are performed in tapping mode, using a VEECO NanoScope IV. For data processing WSxM software was used. [63]

1.5. X-ray photo-electron spectroscopy

X-ray photo-electron spectroscopy (XPS) is a non-destructive method used for analysis of chemical composition of the surface layer (1-100 Å). In this work we applied this method to analyze the chemistry of the surface of sapphire substrate, after it was annealed at high temperature in NH_3 gas flow. The main principle of XPS is based on the photoemission effect. The sample surface is irradiated with a high-energy monochromatic X-ray beam in ultra-high vacuum environment (UHV). An X-ray photon excites the electron from the core-level of an atom on the surface and the kinetic energy (KE) of the excited electron is measured by the the spectrometer. The binding energy (BE) – energy required to remove the electron from the core-level of an atom – is the characteristic value for each electron orbital of the element. It can be deduced from the measured kinetic energy of the excited electron as:

$$BE = h\nu - KE$$

where $h\nu$ – energy of x-ray photon. Therefore, the XPS spectral lines identifies the shell of a chemical element from which the electron was ejected. The binding energy depends on the chemical element, the electron orbital and the local environment of the atom from with the electron was emitted. This implies the binding energy change if the local chemistry and bonding of the element changes – this effect is called chemical shift of the binding energies.
Although the analysis of absolute elemental concentrations from XPS spectra is complicated as it depends on many factors, it is possible to estimate the relative

elemental concentration: [64, 65]

$$\frac{n_1}{n_2} = \frac{I_1}{I_2} \cdot \frac{S_2}{S_1},$$

where $S_1$and S_2– are the atomic sensitivity factors (ASF), which were empirically determined.
In this work X-ray photoemission spectra were recorded using a XPS Thermo Scientific Kα system equipped with an Al Kα monochromatic source with energy $h\nu = 1486.6$ eV. The size of sampled area was $30\mu m$. We observed strong charging effect due to the insulating behavior of sapphire substate, causing a substantial shift of the binding energies. To minimize the charging effect during spectra acquisition, we used a charge compensation – dual-beam flood source that couples low energy ion beams with low energy electrons. Spectra analysis, that included the background extraction of the analyzed peaks and the estimation of relative atomic concentration of the elements, was performed with the ThermoFischer software.

2. Sapphire nitridation

2.1. State of the art and motivation

Nitridation of the sapphire substrate was first suggested by Kawakami et al. [8]. These authors considered nitridation as an approach to reduce the lattice mismatch between Al_2O_3 and epitaxially grown AlN layers, by creating a "buffer layer" via chemical conversion of sapphire surface under NH_3 flow. In their work they have shown an improvement of the morphology of AlN layers grown on $\alpha - Al_2O_3$ substrates nitridated at 1200 °C during 3 minutes. This research has been followed by numerous other publications showing a remarkable improvement of crystalline, optical and electrical properties of AlN, GaN and InN epitaxial films, grown by MOVPE or molecular-beam epitaxy (MBE), when sapphire substrates are nitridated. [66, 67, 68, 69, 70]
As it was mentioned above, nitridation is the chemical conversion of Al_2O_3 surface through the interaction with active N atoms. The N atoms may be provided by dissociation of NH_3 at elevated temperatures in the case of MOVPE and HVPE growth [71, 72]. In the case of MBE growth, apart from using NH_3 as a source of N, nitrogen plasma generated by radio frequency (rf) [73] or electron cyclotron resonance (ECR) [74] can be used. Regardless of the source of nitrogen atoms, nitridation is described by a coupled diffusion process, where inward diffusing N atoms occupy vacant O sites formed by outward diffusion of O atoms. Such atomic mechanism was also proved to be energetically favorable by *ab-initio* calculations. [75, 76]
According to Dwikusuma et al. [71], nitridation of solid Al_2O_3 follows the reaction:

$$Al_2O_3(s) + 2\,NH_3(g) \longleftrightarrow 2AlN(s) + 3H_2O(g)$$

XPS studies of nitridated sapphire surface reveal N-O bonds along with N-Al bonds and suggest that the resulting layer consists of aluminum-oxynitride, rather than pure AlN, due to incomplete substitution of O atoms by N atoms. [69, 77, 78, 71, 79] However, despite the number of studies conducted on the nitridation layers, there is still a lack of agreement between researchers on the microstructure of nitridated sapphire surface and the results are controversial. Uchida and Hashimoto et.al, for example, suggest that the aluminum-oxynitride layer, formed during ammonia nitridation in MOVPE reactor, is amorphous [69, 77]. Other authors suggest that nitridation with N plasma in MBE reactor at lower temperatures (200 – 400 °C) results in a well-defined cubic AlN phase. [80, 81, 82] Recent reports on the layer obtained by ammonia nitridation in MOVPE reactor show the formation of a struc-

ture similar to hexagonal wurtzite AlN phase. [83, 84] The reported thickness of the layers, generated by sapphire nitridation, varies from 1 monolayer of surface nitride [73] up to 200 nm of crystalline AlN [72].
Despite of these discrepancies there is, however, a general agreement on the fact that nitridation conditions, such as temperature, total pressure and duration of nitridation, influence the morphology of the nitridation layer itself, as well as the characteristics of the epitaxial films grown on top of it. It was shown that increasing the temperature or the duration of the nitridation process may result in the formation of three-dimensional protrusions on the sapphire surface. [69, 77, 78, 73, 80] Moreover, Keller et. al. [66], Grandjean and Widmann [67, 85] have demonstrated that structural, luminescence and electrical properties of GaN films grown by MOVPE and MBE are sensitive to the duration and temperature conditions of pre-growth nitridation. Most importantly, the polarity of the epitaxial GaN, AlN and InN films was also shown to depend on the initial nitridation conditions. [86, 87, 88, 89, 79]
Hence, to control structural, electrical and optical properties of III-nitrde layers on sapphire, it is of great importance to understand the processes taking place during the initial growth stages and to conduct a detailed study, based on rigorous structural analysis, of the formed nitridation layers at the atomic scale.
In this chapter we attempt to clarify the described uncertainties and to gain better understanding of the properties of the layers, generated by nitridation, with the focus on the ammonia nitridation in MOVPE growth reactor. As a starting point for our investigations, we chose the temperature $T_{nitr} = 800$ °C, as it was reported that the morphological changes of sapphire surface due to chemical reaction between NH_3 and Al_2O_3 occur at temperatures above 800 °C for ammonia nitridation in MOVPE reactor. [68, 79] Then we gradually increased the experimental temperature up to 1080 °C and varied the process time between 0 and 60 minutes, to investigate the role of the temperature and duration of the nitridation on the chemical composition, morphology and microstructure of the nitridation layers.

2.2. Experiments and results

To study the influence of temperature and time of nitridation on the evolution of sapphire surface, the substrates are annealed in different regimes. Fig. 2.1 is the schematic representation of the nitridation procedure, where T_{nitr} is the temperature, and t – the duration of nitridation. For convenience we name the samples, described in this section, with capital Latin letters. The annealing conditions for each sample, such as temperature T_{nitr} and duration t, are given in table 2.1.
We use two different nitridation processes. In the case of samples A-I, NH_3 gas is introduced in the reactor as soon as the temperature reaches T_{nitr}. Samples J-M are annealed in NH_3 flow while the temperature is rising from room temperature (RT) to 1080 °C with a rate of 80 °C/min. Sample J is obtained by terminating the nitridation when the temperature reaches 1080 °C and we will consider it as nitridated at 1080 °C for "0 minutes". The samples K-M are kept under NH_3 flow

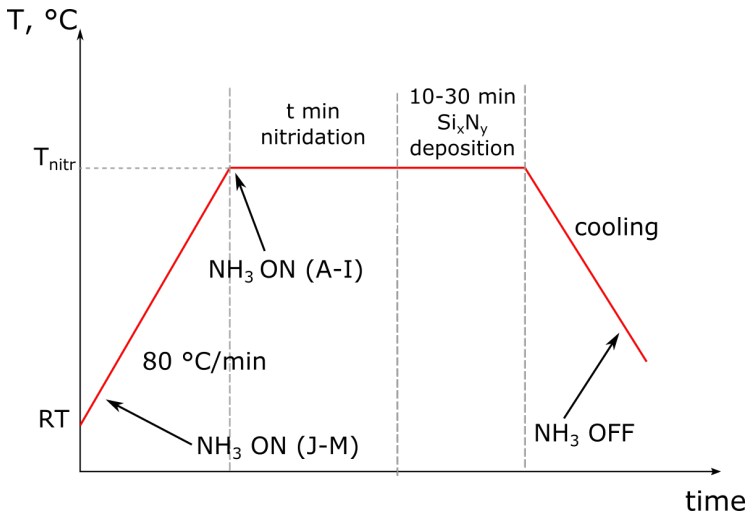

Figure 2.1.: Schematic representation of nitridation process in terms of temperature T versus process time.

Sample	T_{nitr}, **°C**	t, **min**	**Comments**
A	800	10	TheNH_3 flow introduced at T_{nitr}
B	800	30	The NH_3 flow introduced at T_{nitr}
C	800	60	The NH_3 flow introduced atT_{nitr}
D	850	10	The NH_3 flow introduced at T_{nitr}
E	850	30	The NH_3 flow introduced at T_{nitr}
F	850	60	The NH_3 flow introduced at T_{nitr}
G	900	10	The NH_3 flow introduced at T_{nitr}
H	950	10	The NH_3flow introduced at T_{nitr}
I	1000	10	TheNH_3 flow introduced at T_{nitr}
J	1080	0	The NH_3 flow introduced at RT
K	1080	3	The NH_3 flow introduced at RT
L	1080	7	The NH_3 flow introduced at RT
M	1080	30	The NH_3 flow introduced at RT

Table 2.1.: Experimental nitridation conditions for the samples, discussed in this work.

during 3, 7 and 30 minutes respectively after the temperature reaches 1080 °C. After nitridation the samples are analyzed by AFM, ex-situ XPS, high-resolution TEM and scanning TEM. To avoid possible degradation of the layers after exposure to air or during TEM specimen preparation samples, used for TEM analysis, were capped with a thin amorphous Si_xN_y film. The Si_xN_y film is deposited at T_{nitr} for 10-30 minutes after the respective nitridation procedure.

2.2.1. Morphology of the nitridation layer

Fig. 2.2 shows the results of AFM measurements of samples A, B and C, nitridated at 800 °C for 10, 30 and 60 minutes respectively. The view-graph on fig. 2.2 (a) shows the dependence of the surface roughness (RMS) as a function of duration of nitridation. To emphasize the effect of the NH_3 gas flow on the morphology of the sapphire substrate, we consider the roughness parameter of the sapphire substrate, annealed at high temperature (1080 °C) during 60 minutes in a mixed flow of H_2 and N_2 gases without NH_3, which is indicated by a "star". The sapphire substrate annealed at high temperatures without NH_3 exhibits a homogeneous surface with significantly lower roughness parameter (fig.2.2 (b)), while the surface of the sapphire substrate, annealed under NH_3 flow at 800 °C for 10 minutes contains hills and pits, which reach up to 200 nm in lateral dimensions (fig.2.2 (c)). With increasing nitridation time the large patches seen in fig. 2.2 (c) transform into smaller islands with average lateral dimension of 20-40 nm and a height of 1.5-2 nm (fig. 2.2 (d)). The density of these islands decreases from $1.06 \times 10^{10} cm^{-2}$ after 30 minutes of nitridation to values of $0.69 \times 10^{10} cm^{-2}$ after 60 minutes (fig. 2.2 (e)). This is accompanied by an increase of the surface roughness parameter in the time interval between 10 and 30 minutes, but a a slight decrease between 30 and 60 minutes of nitridation. (fig. 2.2 (a))

After nitridation the samples were transferred ex-situ to the XPS chamber. A detailed description of the set-up and the applied conditions is given in 1.5. Although the samples are transferred into a vacuum chamber for the XPS measurements, contamination with carbon compounds, as well as the oxidation of the surface cannot be completely avoided. Therefore, a quantitative analysis of oxygen and nitrogen atomic concentrations is not feasible. Fig. 2.2 (f) shows the N 1s core-level peak measurements of sapphire substrate nitridated at 800 °C for 10, 30 and 60 minutes. The spectrum of a sapphire substrate before the nitridation is shown as a reference. The N 1s peak rises above the noise level in the spectrum of the sample, nitridated for 10 minutes. The intensity of the peak increases with increasing nitridation time. Charging caused by the insulating sapphire substrate results in a shift of the binding energies of the investigated elements. Since the shift fluctuates within each measurement, we are not able to estimate it by recalibration. Therefore we consider the slight shift of several meV of the N 1s peak maximum on the fig. 2.2 (f) as a shift caused by charging, rather than as a chemical shift caused by changes in the local bonding environment of N atoms (i.e corresponding to N-O, N-Al or N-N bonds). Fig. 2.2 (g) shows the integrated atomic concentration of N in our speci-

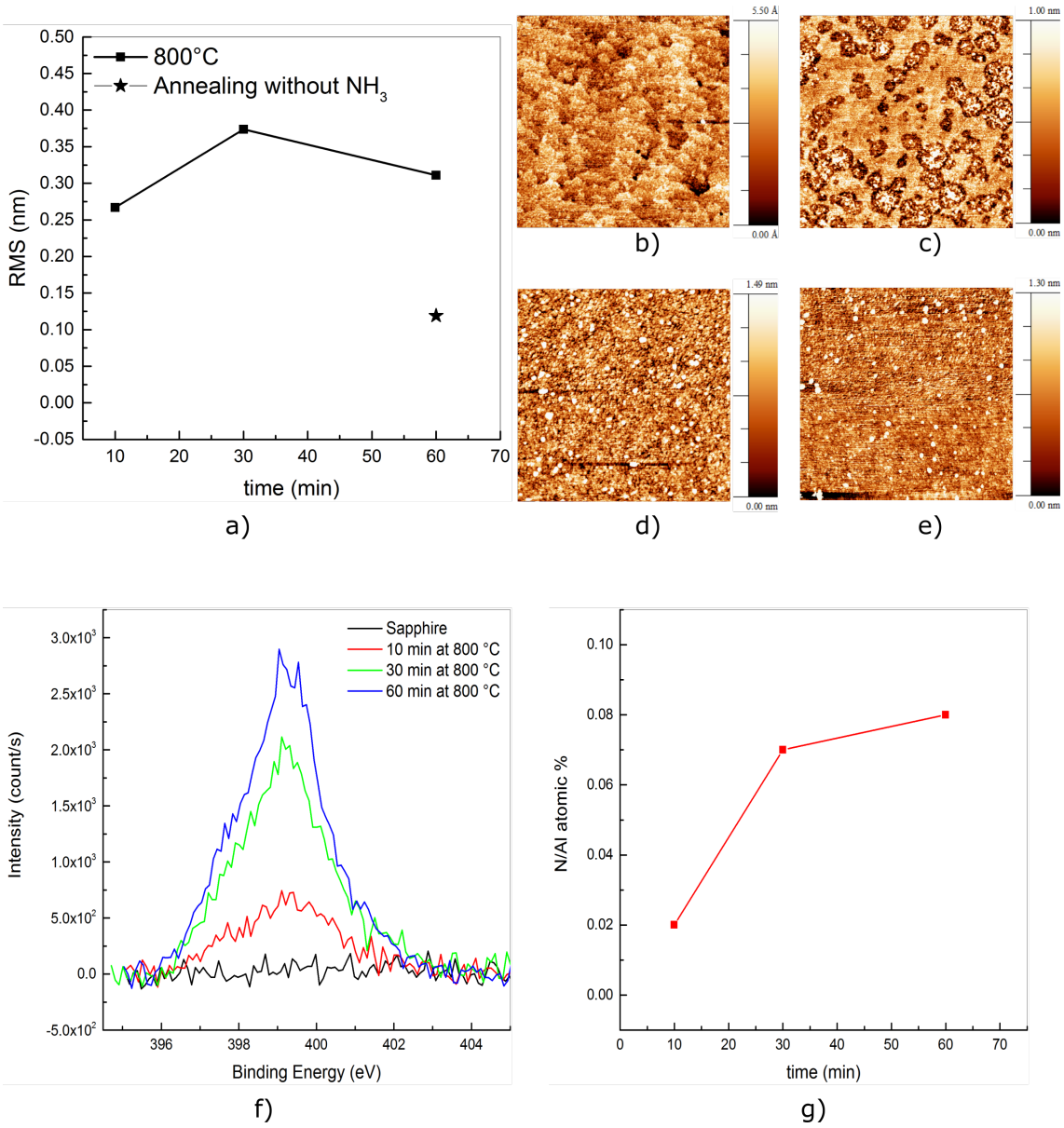

Figure 2.2.: AFM and XPS analysis of the samples A-C (T_{nitr} = 800 °C). a) Surface roughness parameter as a function of annealing time.("Star" denotes the RMS parameter of sapphire substrate, annealed at 1080 °C without NH_3 gas); b) AFM image of the surface of the sample, annealed without NH_3; c) - e) AFM images of the surface of sample A, B and C, respectively. The area size of all topological images is $1 \times 1\,\mu m$. f) N 1s peak arising from the sapphire surface nitridated at 800 °C for 10, 30 and 60 minutes. (The black line corresponds to spectrum of non-nitridated sapphire); g) Integrated atomic concentration of N on nitridated sapphire surface, relative to atomic concentration of Al.

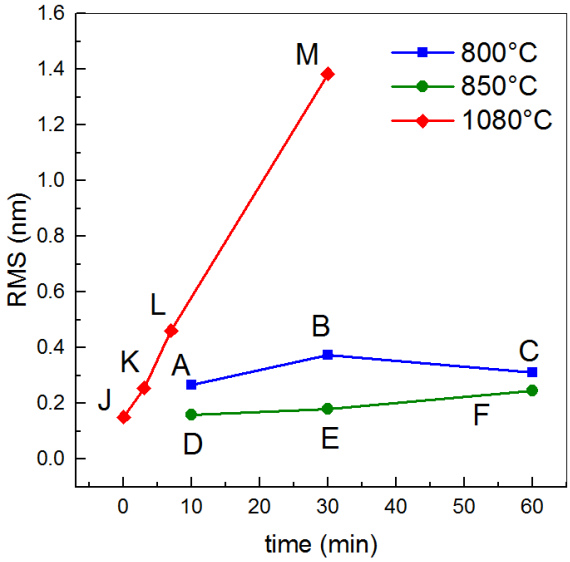

Figure 2.3.: Sapphire surface roughness parameter as dependent on the time nitridation for T_{nitr} =800 °C, 850 °C and 1080 °C. The surface roughness is higher during nitridation at 800 °C, than at first stages (0-10 minutes) of nitridation at 850 °C and 1080 °C. For nitridation at T_{nitr} =1080 °C, the surface roughness increases steeply with time, while it stays almost constant at a nitridation temperature of T_{nitr} =850 °C.

mens normalized to the integrated atomic concentration of Al, which originates from theAl_2O_3 substrate and may be considered as constant in our experiments. The relative concentration of nitrogen increases abruptly between 10 and 30 minutes, but remains almost constant between 30 and 60 minutes.

We will now follow this process and see how the structural transformation of the sapphire surface proceeds as we increase the temperature and the duration of the annealing under NH_3 flow. Figure 2.3 shows the evolution of the roughness parameter of the nitridated surface with nitridation time for 800 °C (samples A-C), 850 °C (D-F) and 1080 °C (J-M). The surface roughness of sapphire nitridated at 850 °C is reduced when compared to the roughness of sapphire substrate nitridated at 800 °C. The AFM image (fig. 2.4 (a)) shows, that the surface after 10 minutes of ammonia annealing at 850 °C exhibits a smooth step-like morphology, very different from the morphology of sample A, annealed at 800 °C (fig. 2.2 (a)). The surface morphology and roughness does not change significantly between 10 and 60 minutes of annealing under NH_3 flow at 850 °C. (fig. 2.4 (b))

The roughness value of sample J, which was continuously nitridated when ramping the temperature from RT to 1080 °C, is close to the roughness value of samples D - F, nitridated at 850 °C, and lower than that of samples A - C, nitridated at 800 °C. The morphology of the surface looks also similar to the surface of sapphire nitridated at 850 °C. (fig. 2.4 (d))

However, as soon as the temperature reaches 1080 °C and the nitridation continues,

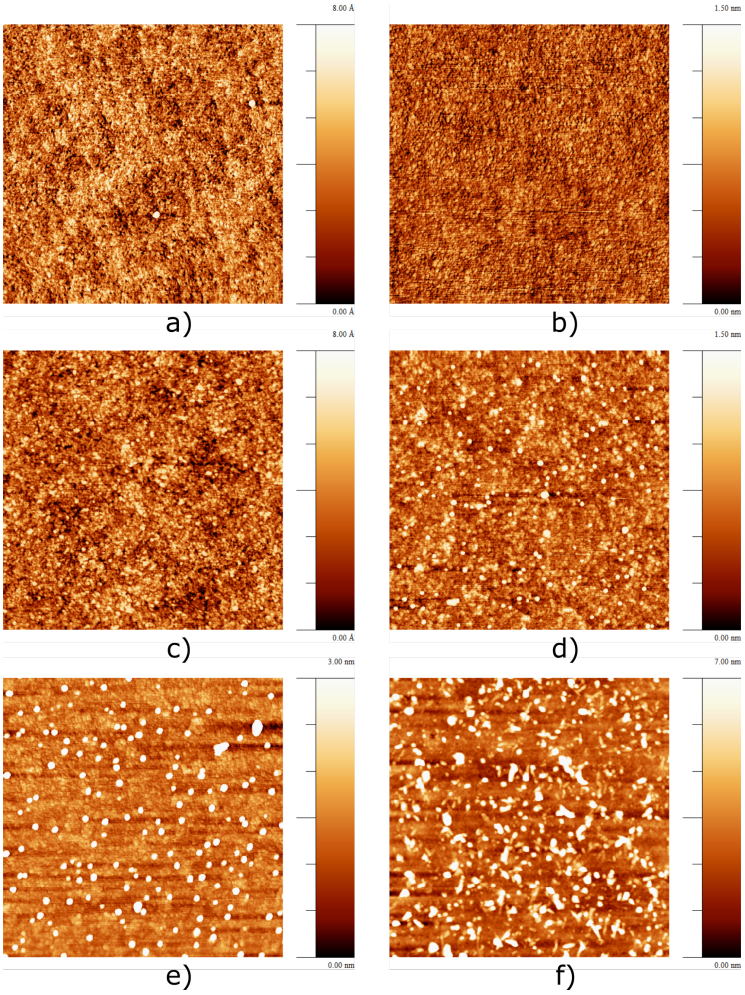

Figure 2.4.: Topological AFM images of sapphire surface nitridated at 850 °C and 1080 °C. a) Sample D (10 min. at 850 °C). The surface exhibits smooth, step-like morphology; b) Sample F (60 min. at 850 °C); c) Sample J (0 min. at 1080 °C); d) Sample K (3 min. at 1080 °C). Small islands are distinguished on the surface; e) Sample L (7 min. at 1080 °C) The size and height of islands increase (note the difference in Z-scale); f) Sample M (30 min. at 1080 °C). The density and size of islands increased, so that closely separated islands appear as one on the AFM image. (The area size of all topological images is $1 \times 1 \mu m$.)

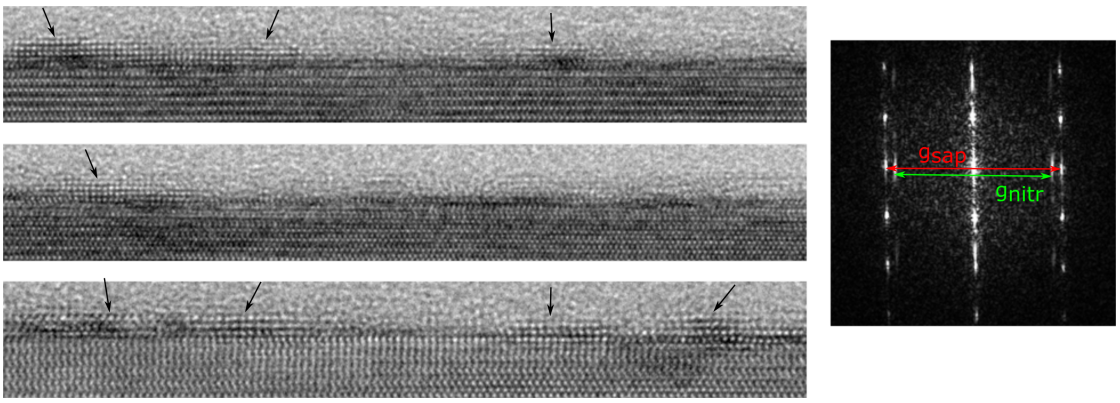

Figure 2.5.: Cross-sectional HRTEM image of sample A in $[10\bar{1}0]_{Al_2O_3}$ projection. Black arrows point on small crystalline regions of foreign structure on sapphire surface. On the right side the Fourier transformation of the image is shown: g_{sap} and g_{nitr} represent the reciprocal distance between $(11\bar{2}0)$ planes of sapphire and respective planes of crystalline structure, formed by nitridation.

the RMS parameter increases steeply with the time of nitridation. AFM image on fig. 2.4 (d) shows that after 3 minutes of annealing in NH_3 at 1080 °C the surface morphology contains an array of well separated islands with a height up to 5 nm and density of approximately $1.1 \times 10^{10} cm^{-2}$. Further increase of the nitridation time up to 7 and then 30 minutes at 1080 °C leads to an increases in both the height and the width of the islands. The density of islands also increases and is approximately $1.7 \times 10^{10} cm^{-2}$ for sample L. On the image of the sample M (2.4 (f)) closely situated islands are no longer resolved as separate, but appear on the AFM image as one large island.

Let us now turn to the TEM analysis of the nitridated sapphire. Several different areas of the surface of the sample A are shown on fig. 2.5 in $[10\bar{1}0]$ projection of Al_2O_3. In some areas, a contrast clearly distinct from that of the sapphire substrate is revealed. These contrast features are randomly distributed along the surface, having a height between 1 to 3 monolayers and lateral extension from 1 nm to up to 10 nm. They appear as well-defined streaks in Fourier transformations of these images (fig. 2.5 (b)). The distance between the $(11\bar{2}0)$ planes of Al_2O_3 is $d^{Al_2O_3}_{(11\bar{2}0)} = \frac{2}{g_{sap}} = 2.4$ Å, which agrees well with the theoretical value $d^{Al_2O_3}_{(11\bar{2}0)} = 2.379$Å(see 1.1). The spacing d_{nitr} of these planes in the unknown material in the given projection is deduced from the distance between corresponding reflections g_{nitr}: $d_{nitr} = \frac{2}{g_{nitr}} = 2.7$Å.

Fig. 2.6 (a) shows a cross-sectional image in the $[11\bar{2}0]$ projection of the sapphire surface, nitridated at 850 °C for 10 minutes (D). We observe 4-6 atomic planes of a crystalline film with an atomically abrupt interface with the sapphire substrate. A bright field plan view TEM image in many-beam conditions in the [0001] projection of Al_2O_3 is shown in fig. 2.6 (b). A two-dimensional translational Moiré pattern, that results from the superposition of the lattice of Al_2O_3 substrate and lattice of

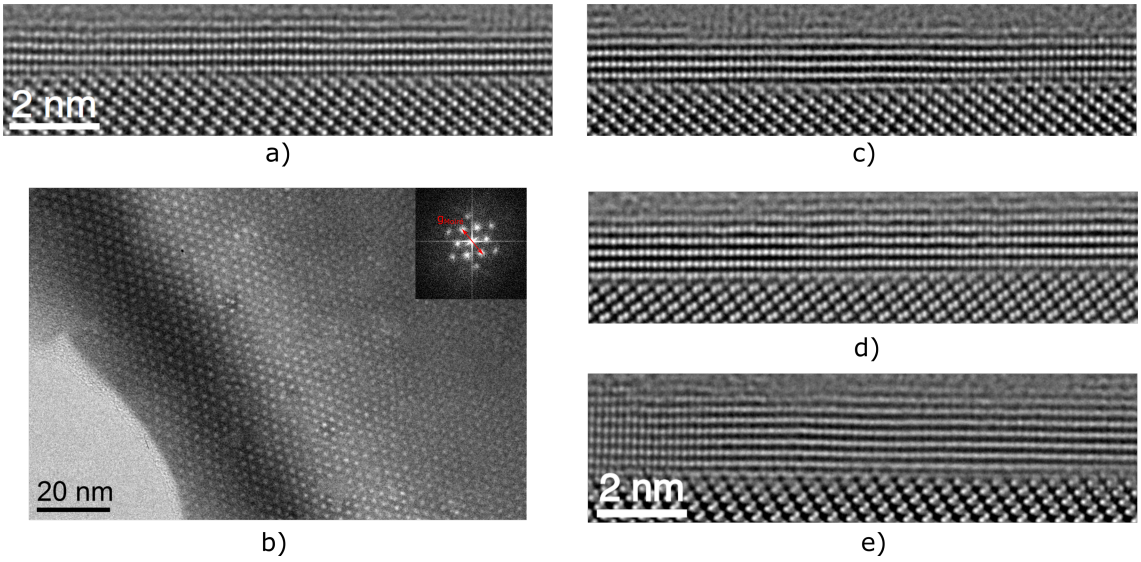

Figure 2.6.: TEM analysis of sample nitridated at 850 °C – 1000 °C. a) Sample D: Cross-sectional HRTEM image along $[11\bar{2}0]$ projection of Al_2O_3. 4-6 monolayers of continuous crystalline film are clearly observed. b) Sample D: Bright-field plan view image in [0001] projection. Moiré pattern due to double diffraction by Al_2O_3 and AlN is visible all over the surface, indicating complete coverage of sapphire surface by nitridation layer. Fourier transformed image in the corner shows the distance between reflections, appeared as a result of double diffraction. The reciprocal distance g_M represent the distance between planes of Moiré pattern. c) Sample G (10 min. at 900 °C) ; d) Sample H (10 min. at 950 °C); e) Sample I (10 min. at 1000 °C) The thickness of the film increases by 3-4 atomic planes between 850 °C and 1000 °C, but no significant morphological changes occur.

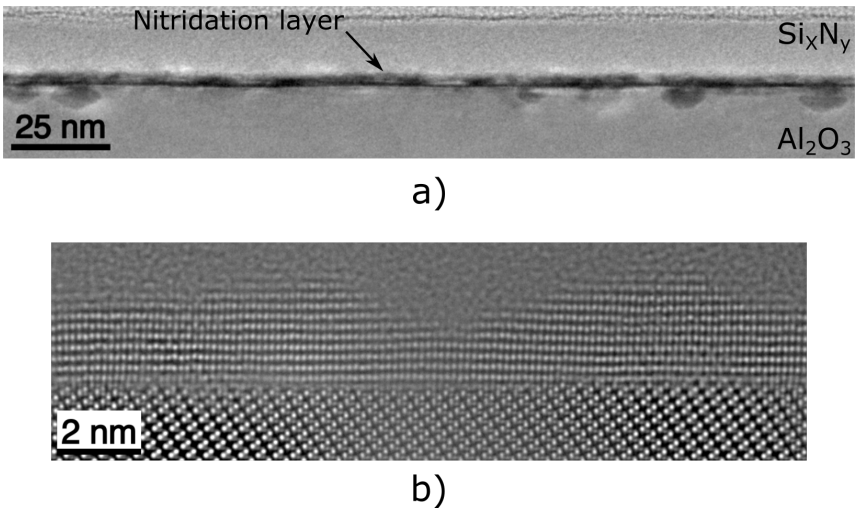

Figure 2.7.: TEM analysis of sample J. a) Bright-field TEM image in $[11\bar{2}0]_{Al_2O_3}$ projection. The nitridation layer, covering the surface, is clearly distinct. Below the nitridation film, hexagonal features with reduced contrast are present. b) HRTEM image in $[11\bar{2}0]_{Al_2O_3}$ projection. The thickness of the film is not uniform and varies between 4-5 ML to 10-12 ML.

nitridation layer in the [0001] orientation, is seen. For the sample D the Moiré pattern is continuous and not interrupted. This proves that the crystalline film, observed on 2.6 (a), is continuous and covers the whole surface of the sapphire substrate.

Fig. 2.6 (c) - (e) shows cross-sectional images of samples, that were nitridated for 10 minutes at 900 °C, 950 °C and 1000 °C , in the $[11\bar{2}0]$ projection of Al_2O_3. The thickness of the crystalline film on sapphire increases by 1-2 atomic planes as we raise the temperature by 50 °C, i.e. it increases approximately by 4-5 monolayers when increasing the temperature from 850 °C and 1000 °C and keeping the same nitridation duration.

The results of the TEM analysis of the sapphire surface, that was nitridated during the heating from RT up to 1080 °C (sample J) are presented in fig. 2.7. Figure 2.7(a) shows a TEM bright-field image under many-beam conditions in $[11\bar{2}0]$ projection of Al_2O_3. The nitridation layer can be identified by a reduced intensity from the sapphire substrate and is 3-4 nm thick. On top of the nitridation film we observe the amorphous Si_xN_y protective film. The nitridation layer possesses homogeneous morphology and thickness within the field of view of 430 nm. Close to the sapphire surface we observe dark features that exhibit hexagonal shape in the given projection. The width of these objects is 8-10 nm and the depth within the surface is about 5-7 nm. The HRTEM image in $[11\bar{2}0]$ projection of Al_2O_3 is given on 2.7 (b). Compared to the surface of the sample, nitridated at 1000 °C (fig.2.6 (c)), we notice that the surface appears more rough and bumpy. The layer thickness fluctuates between 4-5 ML and 10-12 ML .

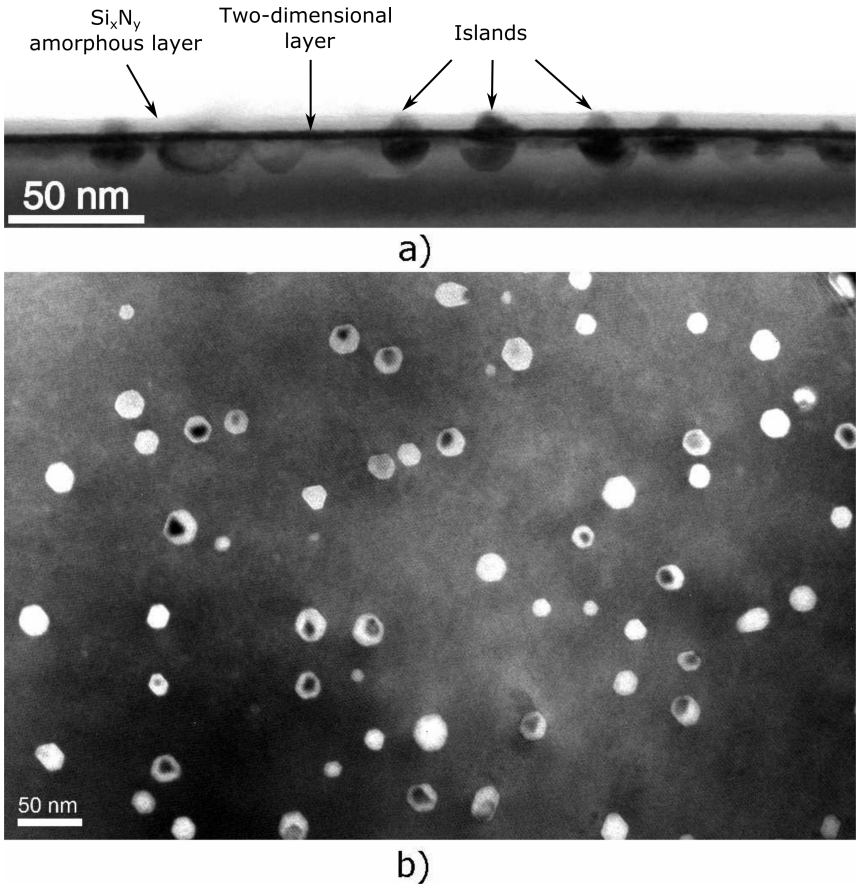

Figure 2.8.: Bright field TEM images of sample M. a) Cross-sectional bright field TEM image of the sapphire surface under many-beam conditions. Pyramidal islands are visible on the surface along with the two-dimensional thin layer. Each island is associated with hexagonal-shaped void in sapphire. b) Plan-view TEM image (many-beam conditions). Voids in sapphire appear as white hexagons. The islands appear as polygonal black features on top of white voids. Voids without islands are also present.

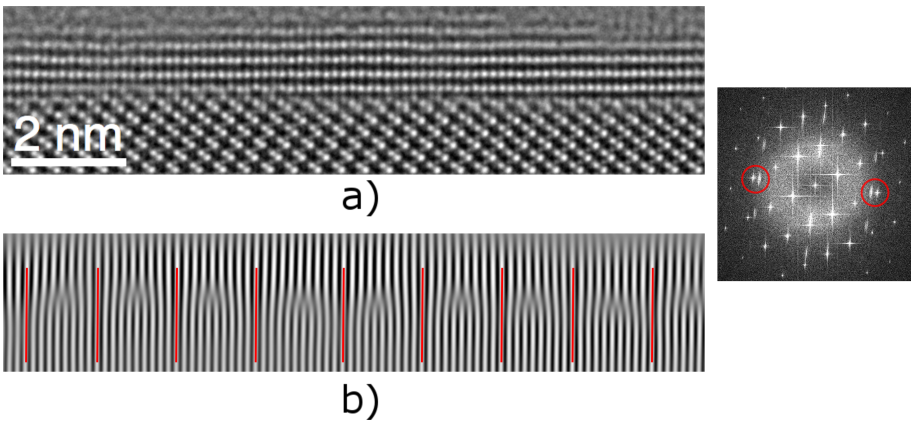

Figure 2.9.: Analysis of misfit dislocations in nitridation film on sapphire substrate. a) High-resolution TEM images along the $[11\bar{2}0]_{Al_2O_3}$ projection of sample D. b) Fourier-filtering of the image (a) using reciprocal lattice spots, shown on the right on Fourier transformed image. Red lines denote coinciding planes of nitridation film and sapphire substrate. Extra half planes in sapphire between coinciding planes indicate misfit dislocations.

Figure 2.8 (a) a shows cross-sectional bright field TEM image of the sapphire surface, that was heated in NH_3 gas flow from RT to 1080 °C and then kept at 1080 °C for 30 minutes (sample M). We observe that the hexagonal features on the sapphire surface have increased in size and have now reached 25 nm in width and 10-15 nm in height. On the plan-view bright field image in many-beam conditions along the [0001] projection these features also exhibit hexagonal geometry and appear in white contrast. This means that the material of the substrate below these regions was completely removed during the TEM specimen preparation, indicating that the thickness of these regions is lower than the thickness of the neighboring areas without the hexagonal objects. Therefore we assume that these hexagonal shaped objects are hollow and designate them as "voids" within the sapphire substrate. On cross-sectional and plan-view images we see that on top of some of these voids pyramidal islands have formed. The dimensions of these islands agree well with the islands observed on the AFM image on fig. 2.4 (f). In conclusion, we find that the nitridation layer transforms from a homogeneously two-dimensional, as observed for samples D-I, nitridated at lower temperatures (between 850 and 1000 °C), as well as for the sample J (0 minutes nitridation at 1080 °C), into a heterogeneous layer, where the two-dimensional layer coexists with three-dimensional islands.

2.2.2. Strain state of the nitridation layer on sapphire substrate

Fig. 2.9 displays a cross sectional micrograph of sample D in $[11\bar{2}0]$ projection of Al_2O_3 along with its Fourier filtered image, using reciprocal lattice spots corresponding to the $(10\bar{1}0)$ sapphire lattice planes and to the lattice plane of the nitridation layer perpendicular to the interface (see the Fourier transform image). It reveals

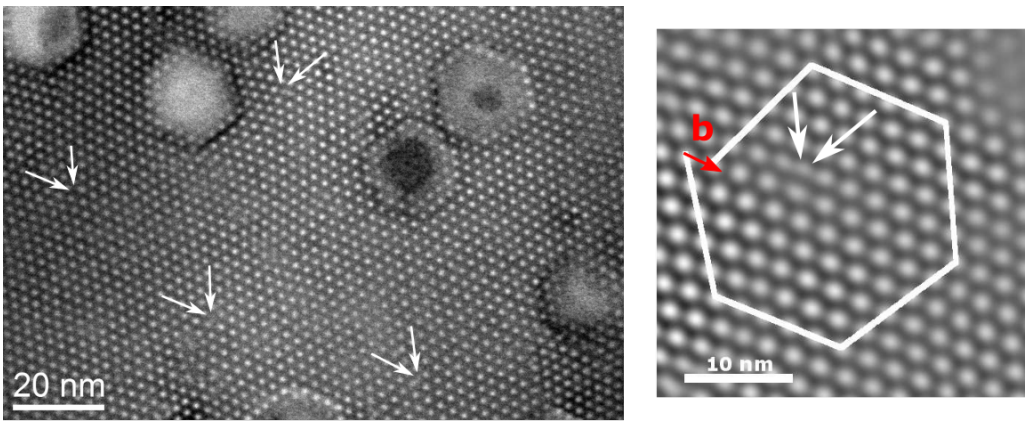

Figure 2.10.: Analysis of threading dislocations in nitridation film on sapphire substrate.a) Bright-field plan view image in [0001] projection under many-beam conditions of sample M. White arrows depict two terminating Moiré fringes, indicating a position of threading dislocation. b) Fourier filtered image of a magnified area containing the threading dislocation. The burgers circuit drawn around it determines the edge component of the Burgers vector.

a regular arrangement of misfit dislocations at the interface, indicating that the crystalline layer, generated by nitridation is, at least partially, relaxed. Basing on averaging of more than 200 planes, we conclude that an Al_2O_3 plane is inserted each 9/10 sapphire planes.
The Moiré fringes observed on the images 2.6 (b) and 2.10 (a) have spacings of $D^D_{eff} = 2.5$ nm. $D^M_{eff} = 2.27$ nm for the samples D, nitridated at 850 °C for 10 minutes, and M, nitridated at 1080 °C for 30 minutes. Locations where fringes of the Moiré pattern terminate, correspond to threading dislocations with an *a*-component. They are indicated with white arrows in fig. 2.10 (a) and (b). The absolute edge component of its Burgers vector is obtained by drawing a Burgers circuit around the dislocation: $\mathbf{b_{edge}} = 1/3 < 11\bar{2}0 >$. We have not observed a *c*-component of threading dislocation on cross-sectional images, therefore we assume that mainly *a*-type threading dislocations are present. We are thus able to determine the density of threading dislocations directly at the interface between substrate and nitridation layer. The density of threading dislocations found here is $1.5 \times 10^{11} \mathrm{cm}^{-2}$.

2.2.3. Atomic structure of the nitridation film

On the cross-sectional HRTEM images in the $[10\bar{1}0]$ projection of Al_2O_3 (fig. 2.11) we can distinguish between herring-bone contrast of sapphire substrate in $[10\bar{1}0]$ projection and zig-zag contrast, corresponding to the wurtzite in $[11\bar{2}0]$ projection. Considering wurtzite structure in the $[11\bar{2}0]$ projection, we are able to analyze the polarity of the nitridation layer directly from the high-resolution TEM images, applying the imaging conditions described in details in 1.2.7. Under these imaging

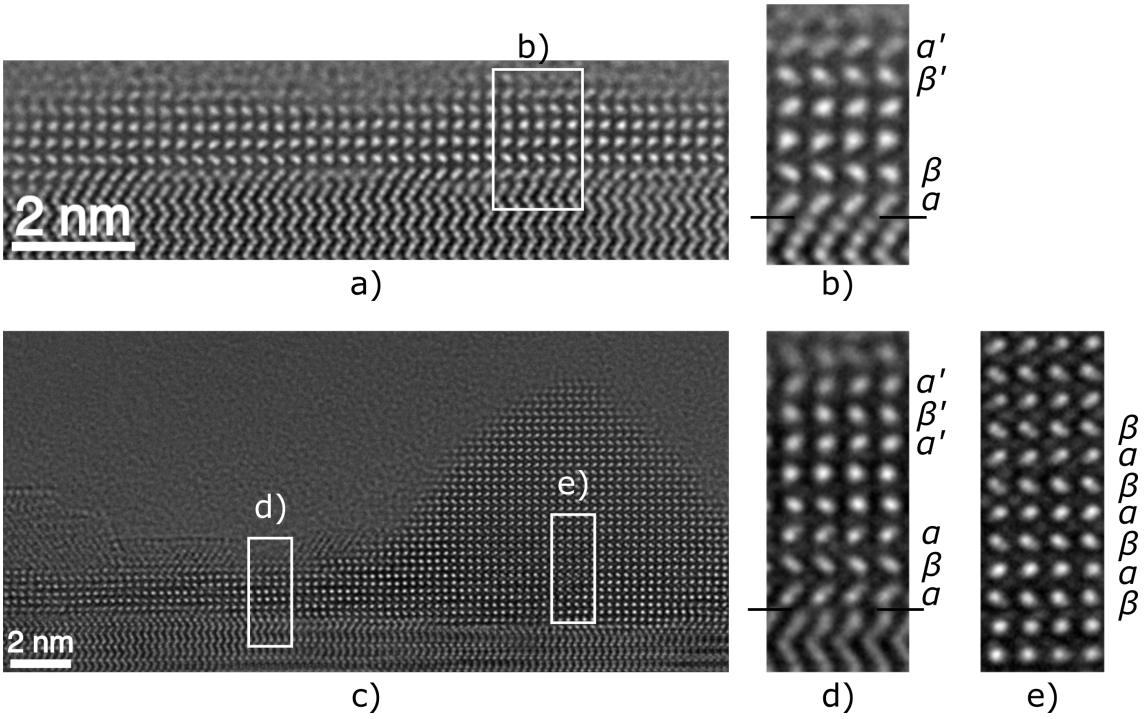

Figure 2.11.: Comparison of atomic structure of nitridation layer, formed at T_{nitr} =900 ℃ and T_{nitr} =1080 ℃. a), c) High-resolution TEM images along the $[10\bar{1}0]$ projection of Al_2O_3 for samples D and M, respectively. b), d), e) Magnified images of areas of nitridation layer, framed in white rectangles on a) and c), respectively, where the polarity and the lattice stacking can be distinguished. On b) and d) lattice stacking is indicated as ...$\alpha\beta$... for the first N-polar monolayers, and ...$\alpha'\beta$'... for the topmost Al-polar monolayers. Two monolayers in between, mediating the change of polarity, violate the stacking sequence. In e) no violation in stacking sequence is present and the layer is Al-polar from the interface.

conditions the anion (O or N) atomic columns appear grayish, while cation (Al or Ga) atomic columns appear at higher intensity.
Fig. 2.11 (a) shows a high-resolution cross-section TEM image of the nitridation layer, generated after 10 min of nitridation at 900 °C (sample G) and 2.11 (b) is a magnified image of its microstructure.The interface between the Al_2O_3 substrate and the wurtzite nitridation layer is indicated by black separating lines. The first and second monolayer above the interface have a N-polarity. In the next two monolayers the pattern of atomic columns has a triangular shape, and Al and N atomic columns cannot be distinguished. Thus, a polarity cannot be assigned for these monolayers. The two topmost monolayers are instead Al-polar. The inversion of the polarity appears together with a discontinuity in the stacking sequence: the first two monolayers follow the sequence $\alpha\beta$, as expected for the wurtzite structure, and end with a β-stacked layer. For the 3rd and 4th monolayers the triangular shape of the contrast does not allow to determine the stacking sequence, however the 5th monolayer is β'-stacked, and not α-stacked as expected by the order. Therefore, the two monolayers, mediating the polarity inversion, introduce an error in the stacking sequence. Since the polarity is switched from the N-polar to Al-polar within these two monolayers, we will designate the 3rd and 4th monolayers as a planar inversion domain boundary (IDB).
On fig. 2.11 (c) is shown a region of heterogeneous nitridation layer, formed after 30 minutes of nitriding at 1080 °C (sample M), in the $[11\bar{2}0]$ projection of wurtzite. The atomic structure of the two-dimensional nitridation layer displayed on the magnified image on fig. 2.11 (d) essentially follows the atomic structure of sample G, observed previously on fig. 2.11 (b): the first three monolayers are N-polar, the 4th and 5th monolayers have roundish contrast and the polarity can no be assigned, starting from the 6th monolayer the film has an Al-polarity. Again, as it is shown on fig. 2.11 (d), the switch of the polarity from N- to Al-polar concurs with a discontinuity in the wurtzite stacking sequence. Fig. 2.11 (e) shows a magnified detail from the center of the three-dimensional island. The island has also a wurtzite structure but exhibits an Al polarity from the third monolayer above the interface. The determination of the polarity of the first two monolayers is not possible. Neither the stacking discontinuity nor the polarity inversion are observed in this case.
Additionally, we performed a HAADF-STEM analysis of both two-dimensional layer and three-dimensional islands (fig.2.12 (a) and (d)). HAADF-STEM measurements were performed with FEI Titan 80-300, whose spatial resolution in STEM mode is not sufficient to resolve Al and N atomic columns separately (the bond length of Al-N dumbbell in $[11\bar{2}0]$ projection is 1.1 Å). Therefore, we used the method of polarity determination by locating tunnel positions, described in 1.2.7, and independently confirmed that the island has a Al-polarity starting directly from the interface, and the continuous layer has a N-polarity at the interface. (see fig. 2.12 (b) and (e))
We have analyzed the HAADF-intensity profiles, normalized to background, along the c-direction. The interface between the sapphire substrate and the nitridation layer on both images appears at lower intensity due to a high density of misfit

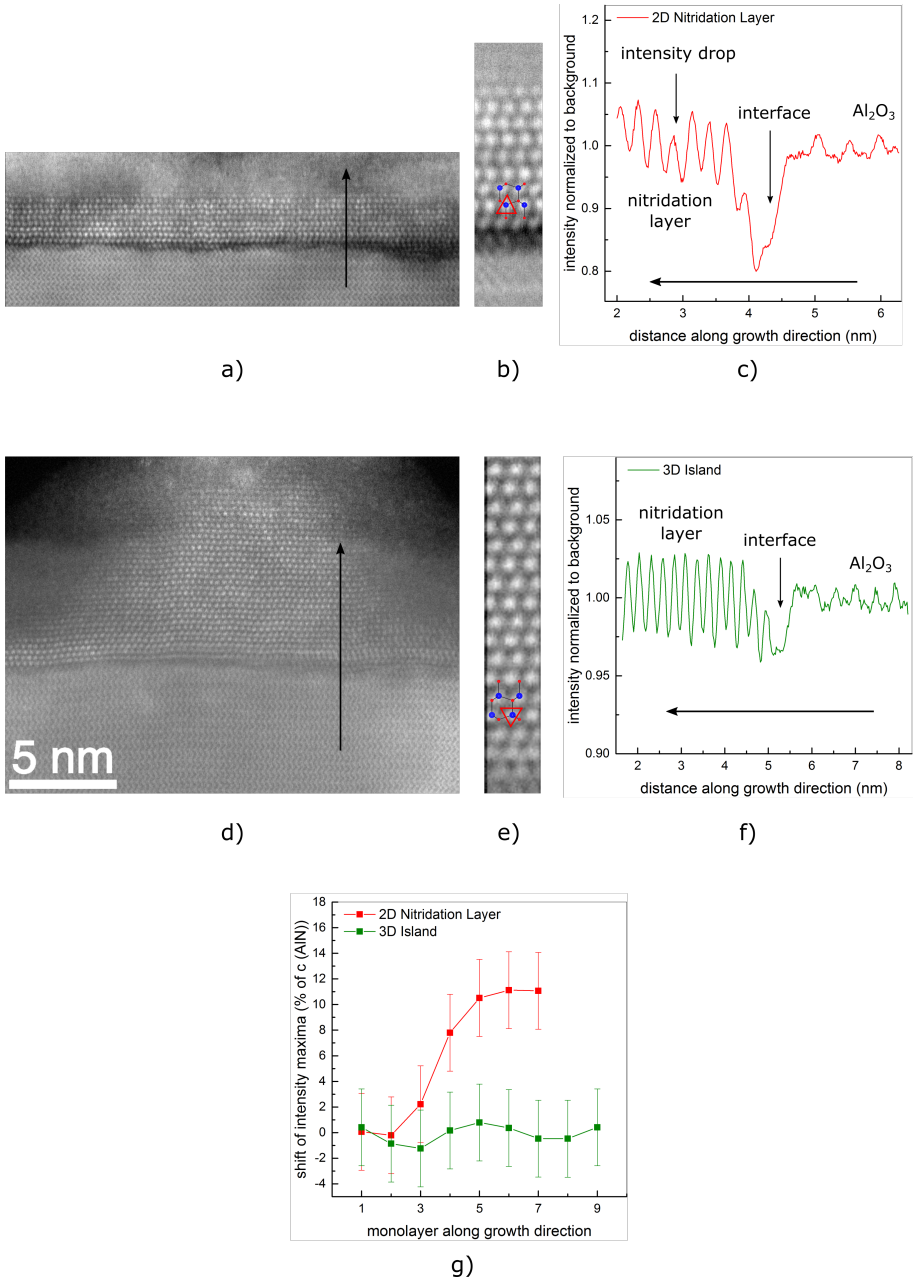

Figure 2.12.: Comparison of two-dimensional nitridation layer and three-dimensional island by HAADF-STEM analysis. a), d) HAADF-STEM images along $[10\bar{1}0]$ projection of Al_2O_3 of two-dimensional layer and three-dimensional island on nitridation film. b), e) Images, composed of superimposed patches from a) and d). Polarity of the layer is confirmed by determining tunneling positions located at vertices of red triangles. c), f) Normalized HAADF-intensity profiles along the direction, denoted by black arrows on a) and d). g) Comparison of displacements of the out-of-plane lattice planes (c) along [0001] direction with respect to the AlN lattice for two-dimensional layer (red curve) and three-dimensional island (green curve).

dislocation located at it. For the two-dimensional layer the normalized intensity profile is shown on fig. 2.12 (c). It reveals the drop of the intensity in the 5th monolayer above the interface. The intensity profile of the three-dimensional island is regular along the growth direction and does not exhibit a similar drop of the intensity (fig. 2.12 (f)).
HAADF-STEM contrast pattern reveals a weighted-average position of the atomic columns. We located the positions of intensity maxima and calculated the average distance between monolayers along the *c*-direction. Afterwards we designated the first two monolayers as reference "AlN" lattice and calculated the cumulative shift of the intensity maxima along the growth direction (i.e *c*-direction) with respect to the reference lattice. The results of this analysis for the three-dimensional island and two-dimensional nitridation layer are plotted on the view graph on fig. 2.12 (g). The two-dimensional nitridation layer exhibits a relative shift of the intensity maxima of approximately 12 % between the second and the fifth monolayers, while the three-dimensional island do not exhibit any substantial displacement of intensity maxima.
To summarize our HRTEM and HAADF-STEM analysis, we have observed that the continuous two-dimensional layer of the nitridation film contains a planar IDB, which inverts the polarity from N- to Al-polarity and is associated with the following characteristic features: a discontinuity in the wurtzite stacking sequence, a relative displacement of the HAADF-STEM intensity maxima along growth direction by approximately 12%, and a reduced HAADF-intensity. The three-dimensional islands do not exhibit any of these characteristic features and have Al-polarity starting from the interface.

2.2.4. Stability of the nitridation layer

In this part we consider the morphological changes of the layer, formed by the nitridation process in MOVPE reactor, caused by post-process annealing under various temperature and ambiance conditions outside the growth reactor.

Post-annealing and ex-situ observations

In this experiment, we perform a post-annealing of sample A, nitridated at 850 °C during 10 minutes. The annealing experiment is carried out in a home-built quartz growth cell. The setup of the growth cell is described in Ref. [90]. Fig. 2.13 shows a schematic representation of the annealing process. The cell with the sample inside is first pumped out overnight at room temperature. Afterwards the temperature is increased to 350 °C and the samples are baked in vacuum during 60 minutes (step I). After the baking, the cell is filled up with N_2 gas till the pressure in the cell becomes P = 800 mbar. During step II the samples temperature is increased up to 1080 °C with a rate of 20 °C/min. The samples are then kept at 1080 °C and annealed for 60 minutes (step III), then cooled down. We perform two experiments with different annealing ambiance. In the first experiment the annealing is done in

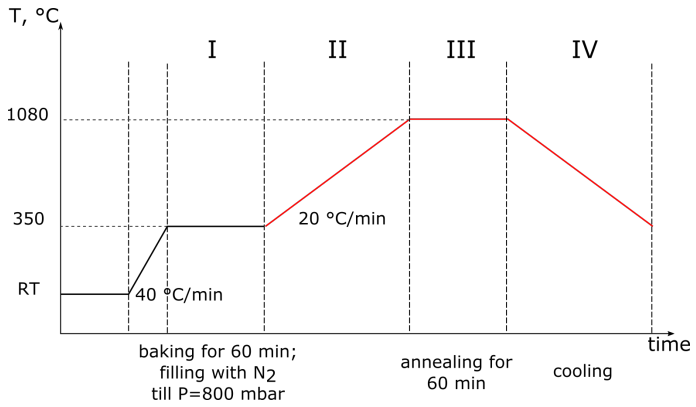

Figure 2.13.: Schematic representation of ex-situ annealing process in terms of temperature T versus process time.

N_2 ambient with a partial pressure P = 800 mbar. In the second experiment a NH_3 gas flow is introduced in the reactor chamber during steps II-IV with a flow rate of 0.5-1 slm during step II (temperature ramp) and 1.1 slm during step III (annealing). After the annealing, the samples are prepared to electron transparency in plan-view observation geometry and examined by HAADF-STEM and conventional TEM. The results are shown in figures 2.14 and 2.15.
Fig. 2.14 (a) is the HAADF-STEM image in low magnification of the sample D before post-process annealing. The HAADF-STEM images of the nitridated sapphire surface after annealing in N_2 and N_2+NH_3 ambiance are shown on the fig.2.14 (b) and (c) respectively. On the surface of the sample, annealed under theNH_3 gas flow, we observe dark faceted voids (fig. 2.14 (c) and (d)), while no such voids are observed on the surface of the sample before annealing (2.14 (a)) or after annealing without NH_3 flow (2.14 (b)). The density of these voids is approximately 1×10^{10}cm^{-2}and their size is about 5-10 nm (fig. 2.14 (d)).
Fig. 2.15(a) and (c) show bright-field TEM images of the nitridated sapphire in [0001] projection of Al_2O_3 after annealing. Fig.2.15(b) and (d) are corresponding images Bragg-filtered using the reflections due to double diffraction, which reveal the Moiré pattern. The presence of the the Moiré fringes pattern in both annealing cases indicates the presence of the nitridation layer. However, the pattern appears to be patched and damaged in the fig. 2.15 (c) and (d), corresponding to the annealing procedure without NH_3, as compared to the Moiré pattern of the sample annealed with the NH_3 flow. This fact might indicate a partial degradation of the nitridation layer when it is annealed at high temperatures without additional NH_3 supply.

Post-annealing of the nitridated sapphire and in-situ TEM observations

In this experiment we study the transformation of the nitridation layer of sample J (30 minutes nitridation at 1080 °C) in-situ in the TEM during an annealing in a vacuum environment. For the details on experimental set-up see 1.2.7. The pressure

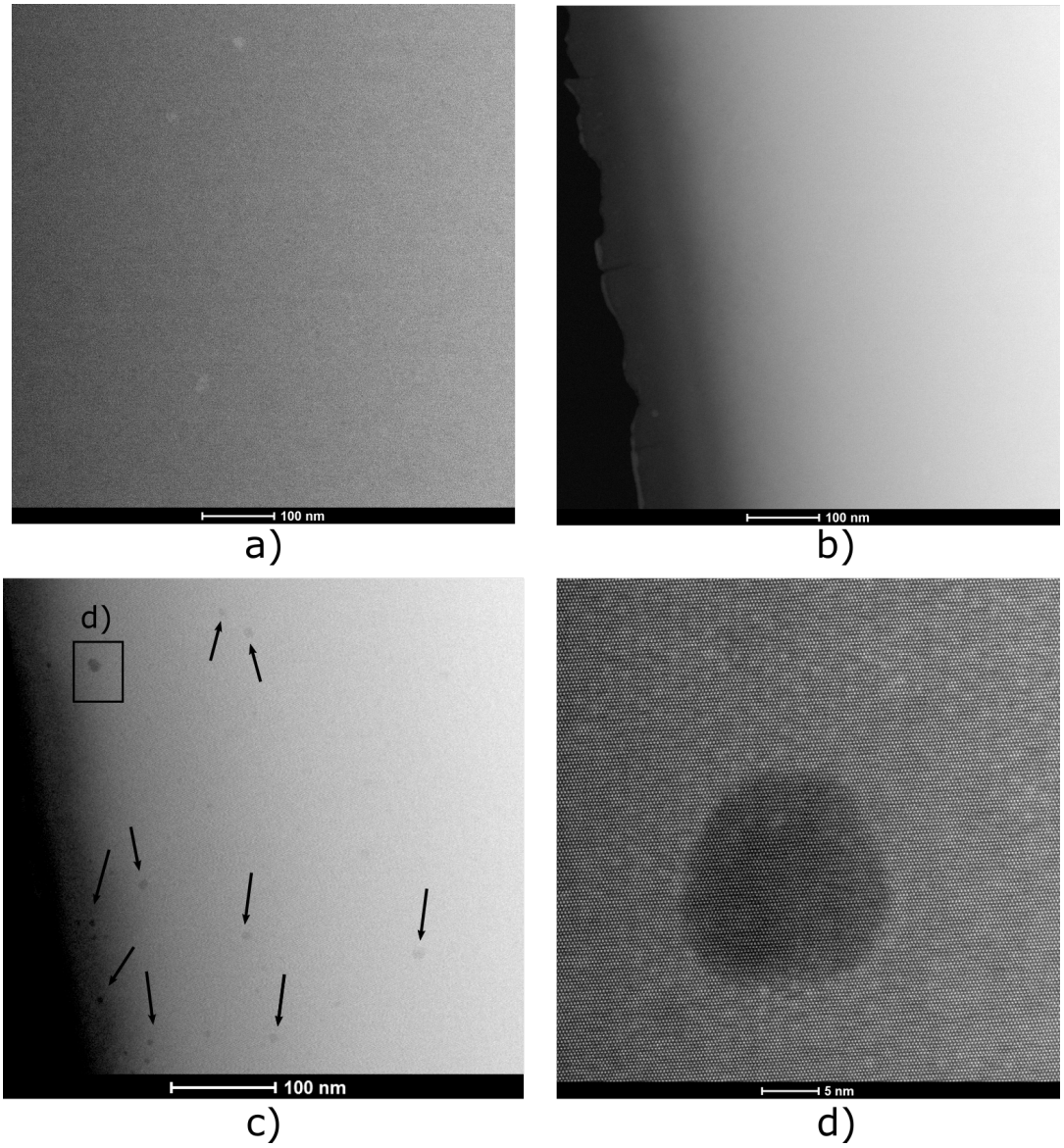

Figure 2.14.: HAADF-STEM plan-view images of the nitridated sapphire surface of sample D before and after ex-situ annealing at T =1080 °C in different annealing environment. a) Before ex-situ annealing: homogeneous, smooth surface, no dark contrast of voids is visible. b) After annealing under N_2 gas: no voids present. d) After annealing in N_2+NH_3: dark facetted voids 5-10 nm in size are present all over the surface with density of $1 \times 10^{10}\text{cm}^{-2}$. e) Magnified imaged of the area with a void: Moiré fringes from remaining nitridation film are visible next to the void.

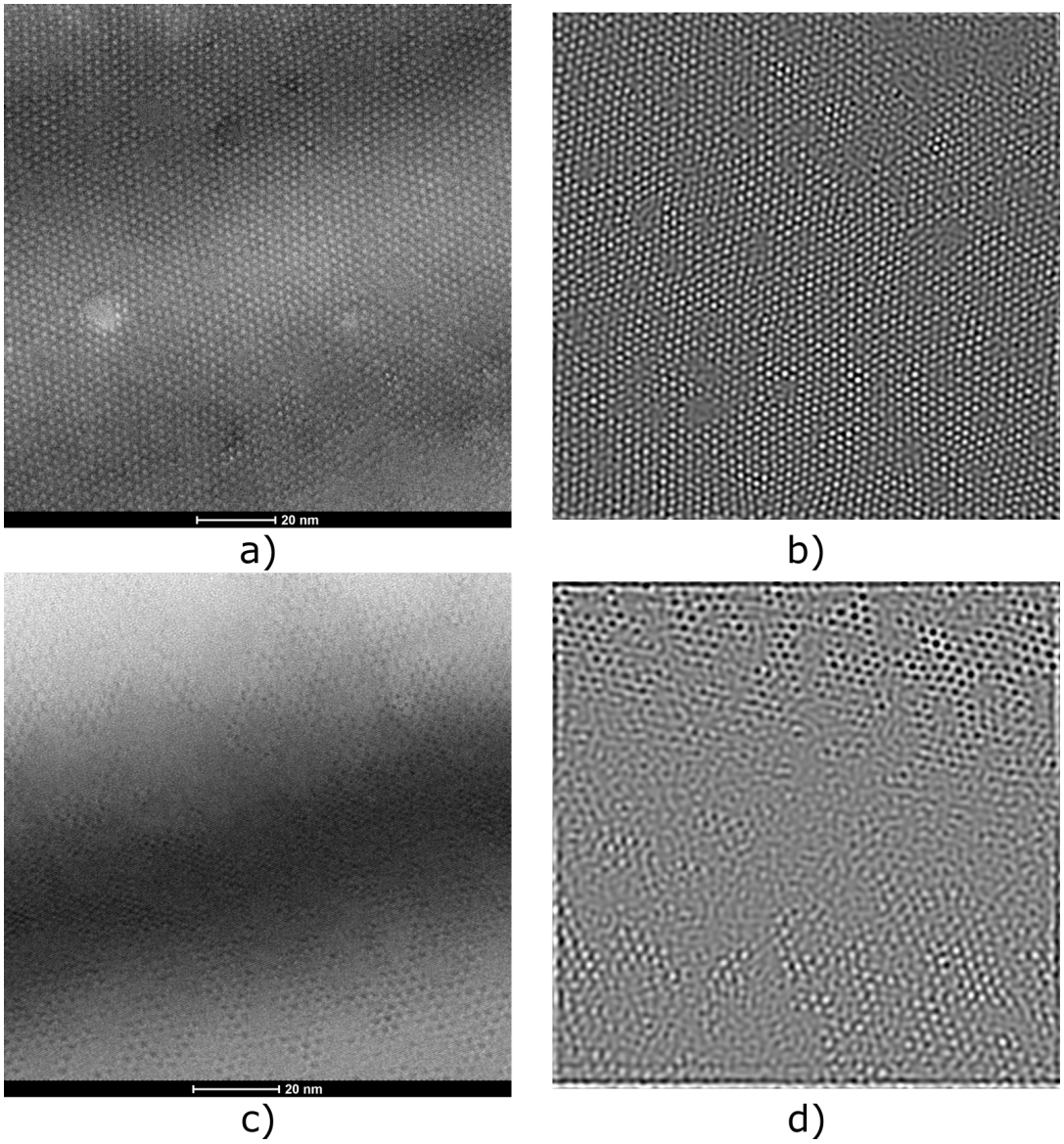

Figure 2.15.: TEM plan-view images of the nitridated sapphire surface of sample D after ex-situ annealing at T =1080 °C in different annealing environment. a), c) Bright-field TEM images under many-beam conditions along [0001] projection of sample D surface after being annealed under N_2+NH_3 and N_2 gas, respectively. b), e) Corresponding Bragg-filtered images, revealing Moiré pattern. On image d) Moiré pattern is patched, which indicates partial decomposition of nitridation layer.

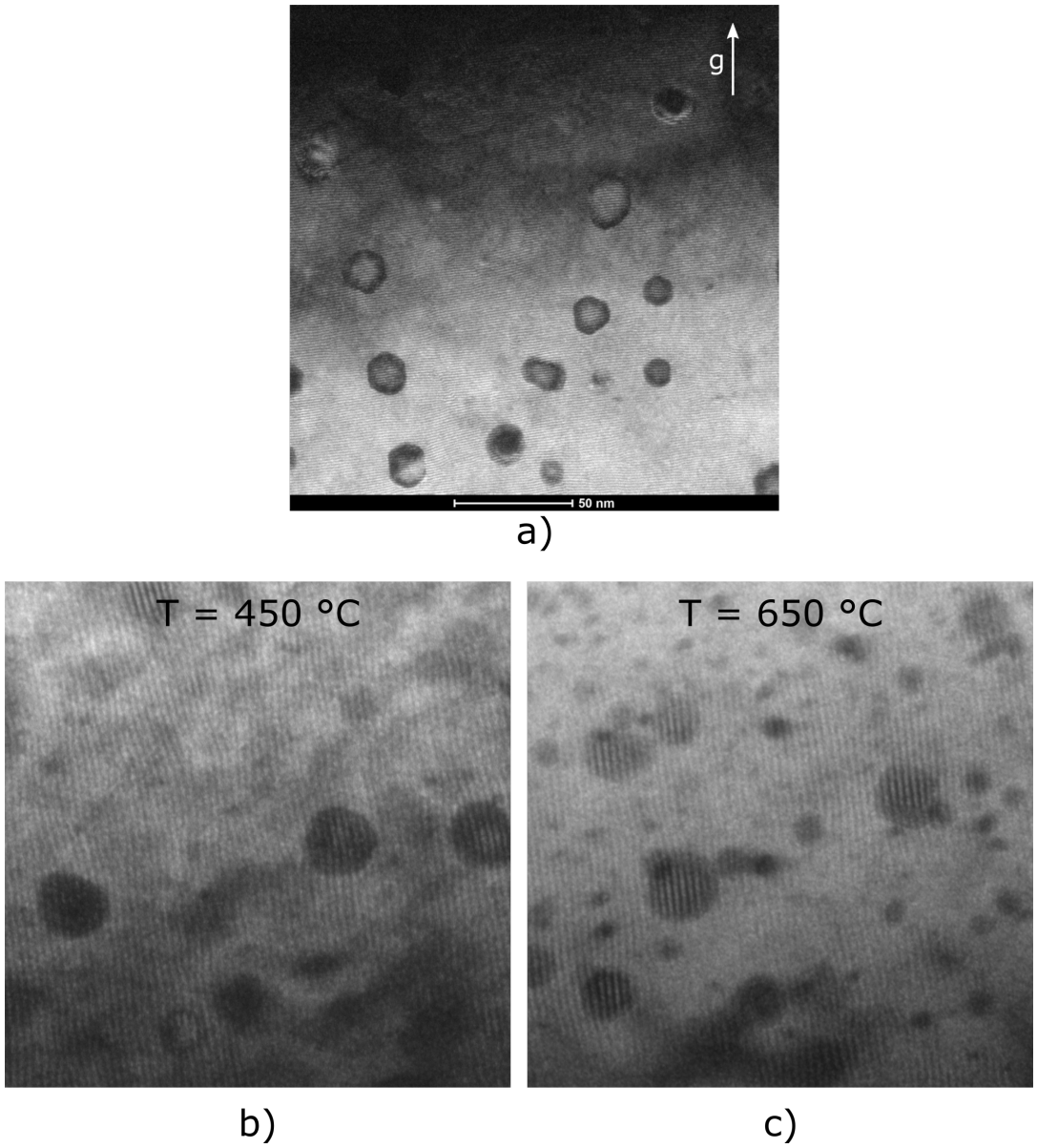

Figure 2.16.: Dark-field plan-view images along [0001] projection of surface of sample M before and after in-situ vacuum annealing. a) Before post-annealing. Dark-facetted voids are present and Moiré pattern is observed all over the surface. b) and c) In-situ observation after annealing temperature reaches T =450 °C and 650 °C, respectively. Moireé pattern is still observed on the surface and above hexagonal voids.

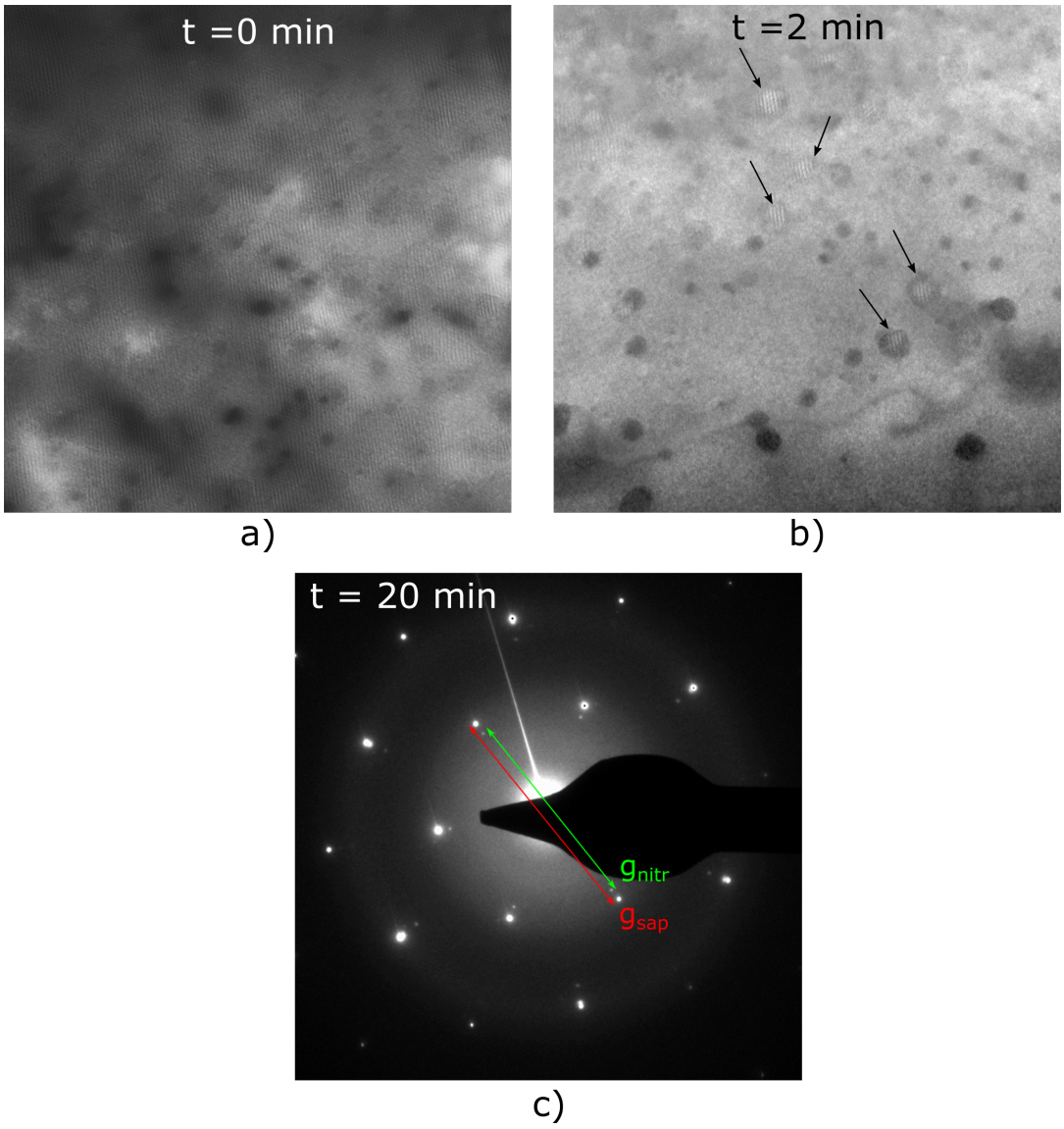

Figure 2.17.: Dark-field plan-view images along [0001] projection of surface of sample M annealed in vacuum at T =850 °C. a) After annealing temperature reaches 850 °C. Moiré pattern is still visible on the whole surface. b) Annealed for $t = 2$ min at 850 °C. Moiré fringes are mainly present above the voids (indicated by black arrows) and not visible on the surface in between voids. c) Diffraction pattern of the surface the after being annealed for $t = 20$ min at 850 °C. Reflection from nitridation film planes are visible next to reflection from sapphire planes.

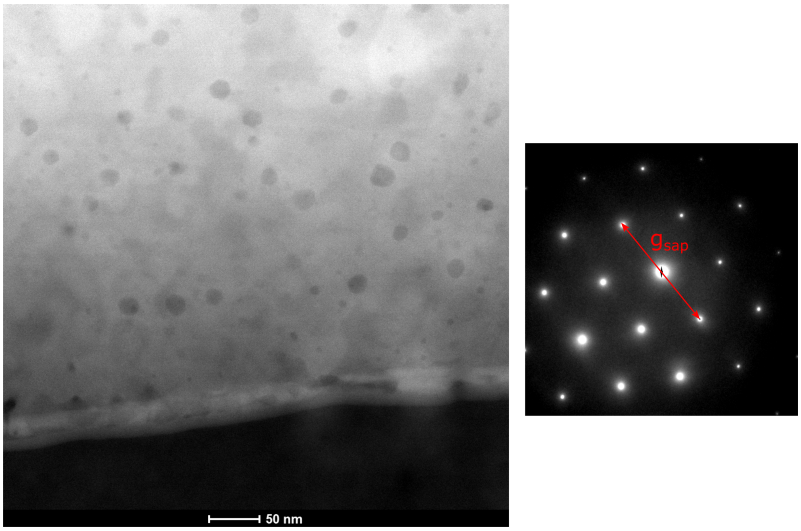

Figure 2.18.: In-situ In-situ observation of surface of sample M after annealing temperature reaches T =1000 °C. a) HAADF-STEM image of the surface of sample M after annealing temperature reaches T = 1000 °C. Moiré fringes are not revealed on the surface. b) Diffraction pattern obtained at same annealing temperature. Only reflections from sapphire planes are present.

during the experiment is P = 0 mbar as no gas was introduced into the heating cell. The electron-transparent 20 µm x10 µm lamella is heated under these conditions from RT up to 1000 °C. Figure 2.16 (a) shows a dark field plan-view TEM image of the specimen before the start of the annealing. We observe the dark faceted voids and Moiré planes, as we have seen before on fig. 2.8 (b) and 2.10 (b). This observation confirms the existence of the nitridation layer on sapphire substrate at the beginning of the experiment.
Fig. 2.16 (b) and (c) show plan-view dark field images of the surface made at T = 450 °C and 650 °C. We see that the Moiré fringes, characteristic of the nitridation layer, remains present in these temperatures. We proceed by increasing the temperature further up to 850 °C. The sample is subsequently kept at this temperature for approximately 20 minutes. Figures 2.17 (a) and (b) show the dark field TEM plan-view images of the nitridated sapphire surface right after the temperature T reached 850 °C ($t = t_0$) and 2 minutes later. We see that after 2 minutes of keeping the specimen in vacuum at 850 °C the Moiré fringes pattern partially disappears. The Moiré pattern remains visible only above the regions of dark faceted voids (marked by black arrows on the fig. 2.17 (b)) and not on the surface in between them. The diffraction pattern image of the specimen in (0001) projection taken after 20 minutes of annealing at 850 °C reveals reflections corresponding to the nitridation layer planes. The in-plane lattice parameter of the nitridation layer is $d_{nitr} = \frac{2}{g_{nitr}} = 2.7$Å, which agrees well with our previous observations for the nitridation layer on sapphire substrate.
We then continue by raising the temperature up to 1000 °C. As seen on the HAADF-

STEM image (fig.2.18 (a)) the Moiré fringes disappear all over the surface, including the regions above the voids. The diffraction image in [0001] projection (fig.2.18 (b)) contains only reflections from the sapphire substrate and no additional reflections from the nitridation layer, as we have observed previously.

2.3. Discussion

2.3.1. Summary and discussion

In this chapter we have analyzed in detail the process of sapphire substrate nitridation under ammonia flow in the MOVPE reactor chamber. Let us now summarize our main findings and propose a tentative description of the nitridation process from the structural point of view based on our observations.

Nitridation layer: morphology

We have shown that 10 minutes of annealing under NH_3 gas flow at 800 °C result in roughening of the sapphire surface, which is not observed if the sapphire substrate is annealed without NH_3 gas. This indicates that the reaction between NH_3 gas and solid Al_2O_3 substrate has started and causes a structural and chemical transformations of the as-received sapphire substrate surface. The transformation results in the formation of a nitridated thin film , as proven by the presence of an N 1s signal in the XPS spectra. HRTEM images show that the sapphire surface is partly

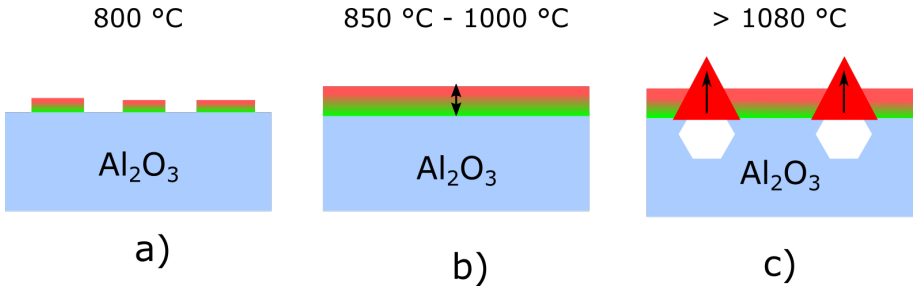

Figure 2.19.: Schematic representation of the nitridation process.(Green color and downwards pointing arrow denote N-polarity; Red color and upwards pointing arrow denote metal-polarity.) a) Initial stage at 800 °C: non-homogeneous formation of aluminum-oxynitride nucleation sites; b) Nitridation within the temperature range 850 °C –1000 °C: coalescence of the nucleation sites and formation of continuous two-dimensional aluminum-oxynitride film. This film induces the inversion from N-polarity at the interface with the sapphire substrate to Al-polarity at the top monolayers. c) Nitridation at the temperature above 1080 °C: three-dimensional Al-polar AlN islands form along with the two-dimensional aluminum-oxynitride film. The islands are located above the hexagonal voids in the sapphire substrate.

covered by a crystalline layer which is 2-4 monolayers thick (see the schematic representation in 2.19 (a)). The in-plane lattice spacing of $d_{nitr} = 2.7$Åagrees well with that between $(10\bar{1}0)$ planes of wurtzite AlN: $d_{\mathrm{AlN}} = 2.695$ Å(see 1.1). As a starting point for a more detailed model and for the sake of simplicity we may stick to the assumption that the layer is close to hexagonal wurtzite AlN, as it was suggested by the previous work of Vennéguès et.al. and Seelmann-Eggebert. [83, 84]
With increasing the nitridation time the chemical transformation to a crystalline layer with atomic structure similar to AlN proceeds and the number of crystalline nucleation sites grows, as it is suggested by the raise of N 1s integrated intensity on fig. 2.2 (g). As we increase the temperature to 850 °C , we find the sapphire surface fully covered by a 1-2 nm of smooth continuous crystalline film after 10 minutes of nitridation , according to HRTEM cross-section and plan-view observations (2.19 (b)). The AFM images show a homogeneous surface, smoother than the sapphire surface nitridated at 800 °C.
Based on these observations we propose that nitridation does not transform the sapphire surface layer by layer, but through non-homogeneous nucleation and growth of a foreign phase at the sapphire surface. With increasing time and temperature, the size and density of nuclei increases and they start to coalesce with each other resulting in a homogeneous smooth surface. Since nucleation and growth are thermally activated processes the rate of the transformation process depends on the temperature and is faster at 850 °C that at 800 °C. The initial stage of surface transformation, by non-homogeneous nucleation of crystalline areas, that could exclusively be observed at 800 °C, is already completed after 10 minutes of nitridation at 850 °C.
The TEM observations show that the layers, formed by nitridation for 10 minutes within the temperature range between 850 °C and 1000 °C, exhibits a very similar morphology, i.e. they are smooth continuous crystalline films, and their thicknesses increase by approximately 3-4 ML .
The orientation relation between the observed nitridation film on sapphire substrate does not depend on the environmental conditions and corresponds to the relation that is usually observed with AlN, heteropitaxially deposited on Al_2O_3substrate, resulting in a 30 ° rotation between the two hexagonal lattices:

$$[0001]_{\mathrm{Al_2O_3}} \Longleftrightarrow [0001]_{\mathrm{AlN}},$$

$$[10\bar{1}0]_{\mathrm{Al_2O_3}} \Longleftrightarrow [11\bar{2}0]_{\mathrm{AlN}},$$

$$[11\bar{2}0]_{\mathrm{Al_2O_3}} \Longleftrightarrow [10\bar{1}0]_{\mathrm{AlN}}.$$

The morphology of the nitridated sapphire surface changes drastically at temperatures above 1000 °C. While the surface roughness of the sapphire substrate continuously nitridated during temperature ramping from RT to 1080 °C is comparable with that of the sample, nitridated at lower temperatures (e.g. at 850 °C), the roughness

increases steeply with further annealing in ammonia flow. After three minutes of nitridation at 1080 ℃ the smooth purely two-dimensional surface transforms into a surface characterized by three-dimensional islands (2.19 (c)). As the time of nitridation at 1080 ℃ increases further, the surface roughness continues to increase, as does the dimension of the islands.

Strain state of the nitridation layer

On the cross-sectional Fourier filtered image we have observed a misfit dislocation network with inserted lattice planes in the sapphire substrate with a frequency of 9/10 planes. If we consider the nitridation layer consisting of AlN, full relaxation of AlN on Al_2O_3 should fulfill the following condition : every m planes of AlN should coincide with (m+1) plane of :

$$m \times d_{\mathrm{AlN}} = (m+1) \times d_{\mathrm{Al_2O_3}}$$

The spacing between $(10\bar{1}0)$ planes of AlN is $d_{\mathrm{AlN}} = 2.695$ Å, the spacing between $(11\bar{2}0)$ planes of Al_2O_3 is $d_{\mathrm{Al_2O_3}} = 2.379$ Å. Then $m = 7.55$, which means one additional plane in Al_2O_3 every $(m+1) = 8.55$ planes. Therefore, the observed additional plane every 9/10 sapphire planes is not sufficient for the full relaxation of AlN on Al_2O_3.
The predicted misfit of the AlN film on Al_2O_3 is:

$$\delta = \frac{d_{\mathrm{Al_2O_3}} - d_{\mathrm{AlN}}}{d_{AlN}} = -0.117$$

From the plan view images of the sample, nitridated at low temperature and time, and the sample, nitridated at high temperature for extended time (sample D and M, respectively, see fig.2.10), we have estimated the average effective distance between the Moiré fringes: $D^D_{eff} = 2.5$ nm, $D^M_{eff} = 2.27$ nm.
The calculated value for the distance between Moiré fringes, caused by the relaxed AlN film on Al_3O_3 substrate, according to eq. 1.25 is:

$$D = \frac{d_{\mathrm{AlN}} d_{\mathrm{Al_2O_3}}}{d_{\mathrm{AlN}} - d_{\mathrm{Al_2O_3}}} = 2.029\, nm$$

Knowing the effective D_{eff} for the samples D and M (we can find the effective in-plane lattice parameter d^{eff}_{nitr} of the film on top of the sapphire substrate generated by nitridation process at different conditions: $d^D_{nitr} = 2.629$ Å, $d^M_{nitr} = 2.658$Å, and we can estimate the effective misfit in our experimental structure using the equation:

$$\delta_{eff} = \frac{d_{\mathrm{Al_2O_3}} - d_{nitr}}{d_{nitr}}$$

The value of the effective misfit is found to be $\delta^D_{eff} = -0.095$ for the nitridation film generated after 10 minutes at 850 °C and $\delta^M_{eff} = -0.105$ for the nitridation film after

30 minutes of nitridation at 1080 °C. If we assume the observed nitridation film to be an AlN layer, the degree of relaxation as compared to the relaxed wurtzite AlN on Al_2O_3 substrate, increases from $\frac{\delta^D_{eff}}{\delta} \times 100\% = 81\%$ for the film, formed in the beginning of nitridation to $\frac{\delta^M_{eff}}{\delta} \times 100\% = 89\%$ for the film that was kept under NH_3 during 30 minutes at high temperature. This result indicates that the morphological transformations observed at high temperatures and extended nitridation time, are accompanied by additional plastic relaxation of the nitridation film.
Apart from misfit dislocations, we observe high density ($1.5 \times 10^{11}\text{cm}^{-2}$) of *a*-type threading dislocations. This means, that dominant crystal defects in III-nitride films, observed by some researchers on the initial stages of buffer layer growth [91], are forming already on the stage of nitridation, i.e. during chemical transformation of the sapphire substrate at high temperatures.
A residual compressive strain is still present in the nitridation film even after 30 minutes of sapphire nitridation at 1080 °C. A possible explanation may come from the assumption that nitridation film does not consist of AlN but rather of an intermediate aluminum-oxynitride phase with an unknown stoichiometry. This assumption is triggred by numerous reports on the XPS studies of chemical composition of the sapphire surface after nitridation, where the original N 1s signal peak was fitted by two Gaussian peaks, corresponding to components related to Al-N bonds and to N-O bonds.

Stability

We have shown that high temperature annealing of the nitridation layer without NH_3 (i.e. without source of atomic nitrogen) results in partial degradation of the nitridation film. This observation was supported by in-situ TEM observation during annealing in vacuum atmosphere of the heterogeneous nitridation layer, formed as a result of nitridation at 1080 °C during 30 minutes, as described in section 2.2.4. We have shown that the two-dimensional layer, containing the planar IDB, and covering sapphire surface in between hexagonal voids, starts to degrade as soon as T reaches 850 °C and completely vanishes after 2 minutes of annealing at 850 °C. The layer above the hexagonal voids (i.e. Al-polar islands) is by far more stable and remains intact at significantly higher temperatures. It disappears completely at temperatures beyond 1000 °C.
We have also observed that nitridation at temperatures above 1000 °C promotes the formation of voids in the sapphire surface, that have hexagonal shape in $[10\bar{1}0]$ and [0001] projections of sapphire (see fig.2.7). It is important to note, that the nitridation film still appears to be continuous and uninterrupted, despite of the presence of voids near the interface between sapphire and nitridation film. Moreover, the three-dimensional crystalline Al-polar islands are exclusively observed above the regions with voids.
In the post-annealling experiments performed with the nitridated sapphire substrate in home-built quartz growth cell at 1080 °C, we observed that the hexagonal voids

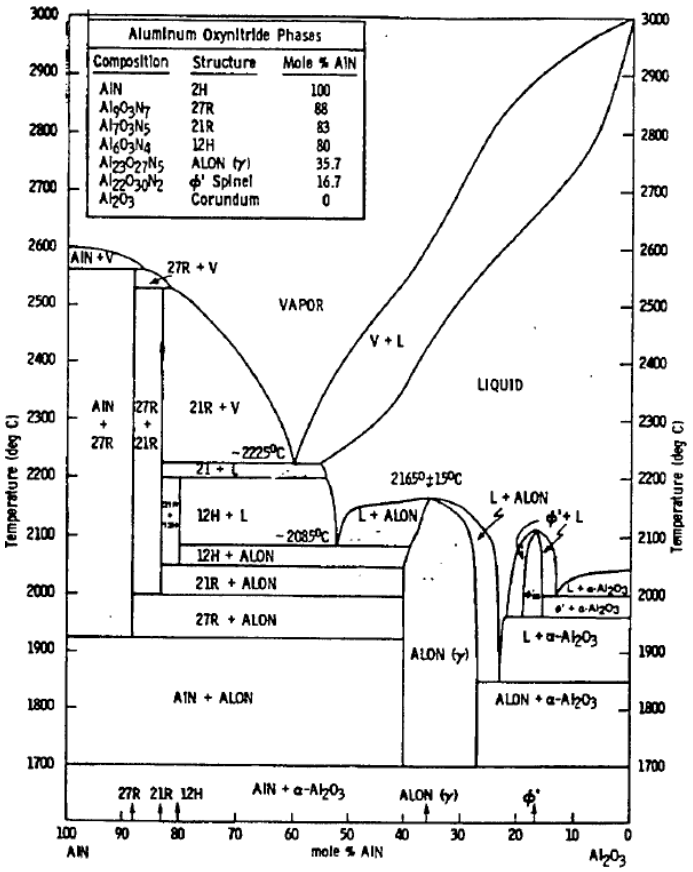

Figure 2.20.: Phase diagram of the Al_2O_3−AlN pseudo-binary system. [92]

are formed on the surface when NH_3 gas flow is present in the annealing chamber, and do not form when only pure N_2 is present. We suggest that in our nitridation experiments, hydrogen, a by-product of NH_3 dissociation, may act as the reducing agent and thus cause sapphire decomposition and voids formation. Since Moiré fringes are sometimes observed above the voids, we suppose that hydrogen may diffuse towards sapphire surface through the formed nitridation film, however the exact mechanism of void formation remains unclear.

2.3.2. $Al_9O_3N_7$: structural model of the nitridation layer

As was already mentioned, at the atomic level, nitridation can be described as a process involving out-diffusion of oxygen and in-diffusion of nitrogen, resulting in substitution of oxygen atoms by nitrogen. Structurally, the substitution of nitrogen by oxygen in AlN or of oxygen by nitrogen in Al_2O_3 destabilizes the parent structures and results in the formation of new phases with different crystal structures and symmetry. Substitution of oxygen by nitrogen in Al_2O_3 causes a local charge imbalance at the substituted nitrogen site. This imbalance can be minimized by shifting the anion coordination around Al from six to four. Initially it may lead to

Phase (notation)	mol % AlN	Formula	Structure
2H	100	AlN	Hexagonal
27R	87.5	$Al_9O_3N_7$	Rhombohedral (polytype)
16H	85.7	$Al_8O_3N_6$	Hexagonal (polytype)
21R	83.3	$Al_7O_3N_5$	Rhombohedral (polytype)
γ-AlON	35.7	$Al_{23}O_{27}N_5$	Spinel
δ-AlON	10	$Al_{19}O_{27}N$	Spinel
Corundum	0	Al_2O_3	Corundum

Table 2.2.: Aluminum-oxynitride phases observed in the Al_2O_3-AlN pseudo binary system for various mole concentration of AlN. [93]

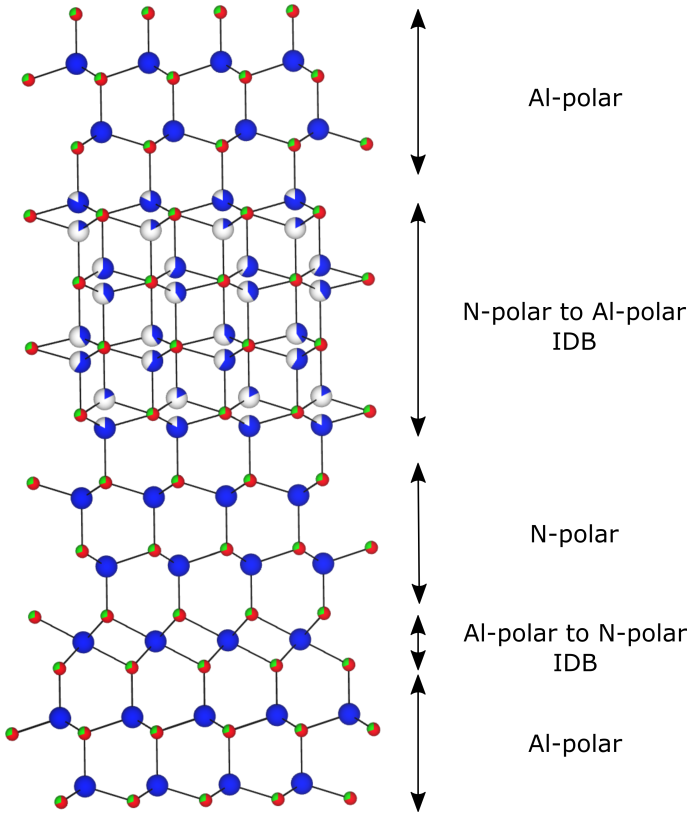

Figure 2.21.: Theoretical ball-and-stick model of $Al_9O_3N_7$. The anion positions (small balls) are filled with 70% N (denoted as red color) and 30% O (denoted as green color). The cation positions (big blue balls) are occupied by Al and Al vacancies, thus displayed with different filling ratios, where the Al content of the column is illustrated by the filled fraction of the circle.

the formation of a spinel-type structure, where the cations are distributed between octahedrally- and tetrahedrally-coordinated sites. The description of the formation of this phase was first shown by Goursat et al. [94] and later refined by Tabary et al. [95], based on the model suggested by McCauley et al. [96]. However, the phase diagram of the pseudo-binary system is not limited to the spinel-type phase and contains at least 13 different phases with various compositions of AlN, several of which are shown in tab.2.2. Figure 2.20 shows the experimental phase equilibrium diagram proposed by McCauley and Corbin. [92] There are two main phases distinguished by their structure in this diagram. The first group of compounds is located in the Al_2O_3-rich area of the diagram and is based on the defective spinel structure. In the AlN-rich region the compounds are aluminum nitride polytypoids. They crystallize as layered superstructures, based on the AlN wurtzite lattice with a large *c* lattice parameter. There are three main types of aluminum-oxynitride polytypoids on the AlN-rich region of pseudo-binary system of Al_2O_3-AlN : $Al_9O_3N_7$ (27R), $Al_7O_3N_5$ (21R) and $Al_6O_3N_4$ (16H). In the notation of Ramsdell, the polytypoid phases $Al_nO_3N_{n-2}$ are denoted as 2nH (where n – even and "H" stands for "Hexagonal" symmetry) and 3nR (n – odd, and "R" stands for "Rhombohedral" crystal symmetry).

Let us now consider the 21R and 27R rhombohedral phases. These phases have been synthesized in crystalline form and investigated by [97][98]. Both of these phases have a significantly large c-lattice parameter (5.7 nm and 7.2 nm, respectively) and a layered superstructure, based on wurtzite AlN. As an example, fig. 2.21 shows the structure of $Al_9O_3N_7$ as found by Asaka et al. The structure has two planar IDB and changes its polarity twice. The first inversion domain boundary inverts the "Al-polar" to "N/O-polar" and contains a lateral in-plane displacement. The second inversion domain boundary changes the polarity from "N/O-polar" to "Al-polar". It may be essentially described as two interpenetrating "N/O-polar" and "Al-polar" wurtzite type lattices, that share a common anion sub-lattice. The cation occupancy on the "N/O-polar" sub-lattice fades out along [0001] direction, while the cation occupancy on the "Al-polar" sub-lattice stepwise increases. The anion sites are randomly occupied by O and N atoms.

As we have shown, the nitridation process at the temperatures above 850 °C generates a relaxed smooth two-dimensional film at the sapphire surface, which has an in-plane lattice constant close to that of AlN and the known hetero-epitaxial relation of AlN on Al_2O_3. The atomic structure of the two-dimensional nitridation film is persisting, regardless of the temperature at which the film was formed. This film starts with N-polarity at the interface, as it is predicted by Di Felice and Northrup for the Al_2O_3/AlN interface under N-rich growth conditions. [99] The thickness of the nitridation layer is approximately 6-8 monolayers, the inversion of polarity from N-polar to Al-polar is observed after 2 monolayers on fig. 2.11 (b) and after 3 monolayers on fig. 2.11 (d). The planar inversion domain boundary comes along with the discontinuity in the wurtzite stacking sequence. Therefore we focus our attention to that part of the rhombohedral R27 ($Al_9O_3N_7$) phase which contains an

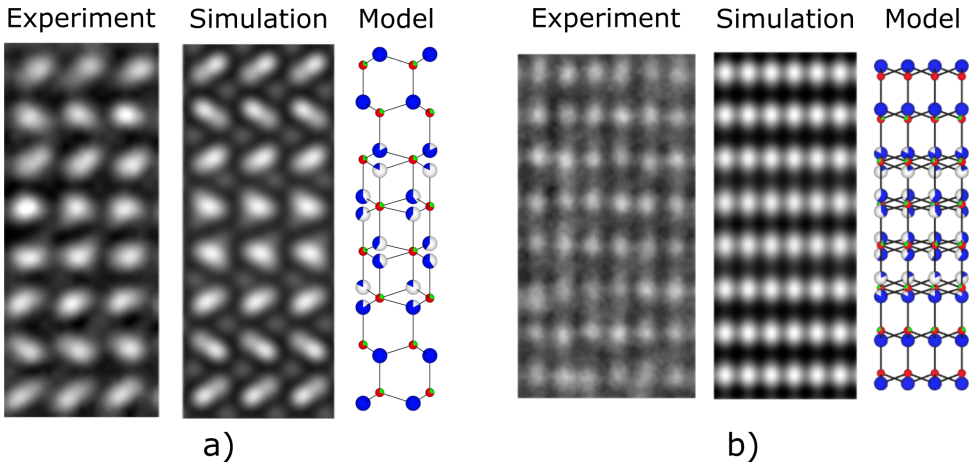

Figure 2.22.: Comparison of HRTEM images of nitridation layer with phase-contrast image simulation of $Al_9O_3N_7$ IDB model along two principal projections: a) $[11\bar{2}0]$; b)$[10\bar{1}0]$. Ball-and-stick models in respective projections are given next to image simulations.

inversion domain boundary changing the polarity from "N/O-polar" to "Al-polar" as observed on our experimental images of the nitridation layer.
We have performed TEM image simulations for phase-contrast imaging for AlN wurtzite structure with an $Al_9O_3N_7$ planar type IDB within (fig.2.24). HRTEM patterns are simulated with the multi-slice approach, using simulation parameters corresponding to the used experimental conditions. The simulated contrast patterns shown in this work are for the sample thicknesses between 4.5 and 5 nm. The results of these simulations are shown on fig.2.22 along $[11\bar{2}0]$ (fig. 2.22 (a)) and $[10\,\bar{1}_0]$ (fig. 2.22 (b)) projections of AlN together with the experimental HRTEM images of the sample M (30 minutes nitridation at 1080 °C). Comparing the experimental and simulation data in fig.2.22, we find nearly perfect agreement. In the $[11\bar{2}0]$ projection of AlN the third and the sixth monolayers of the IDB are hard to distinguish from pure AlN dumbbells on the HRTEM experimental images, because the N-polar cations at the lower interface and the Al-polar cations at the upper interface have a dominating occupation (approximately 83%). In the two central layers, both cationic positions have nearly equal occupancy (approximately 60% to approximately 40%), and two AlN dumbbells result in blurred round-shaped contrast, hence polarity cannot be determined.
We have also performed Z-contrast STEM imaging simulations. The structure used for the STEM simulations is shown in fig.2.23. It extends over 18 monolayers along the *c*-direction (four monolayers of the $Al_9O_3N_7$ IDB and seven monolayers of AlN on each side) (2.23 (a)) and 24 *a* lattice parameters in the direction of the electron beam (2.23 (b)). Cation sites in the four layers of inversion domain boundary (IDB) are statistically occupied within the depth of the supercell with either Al atoms or vacancies according to the average occupancy of the columns.

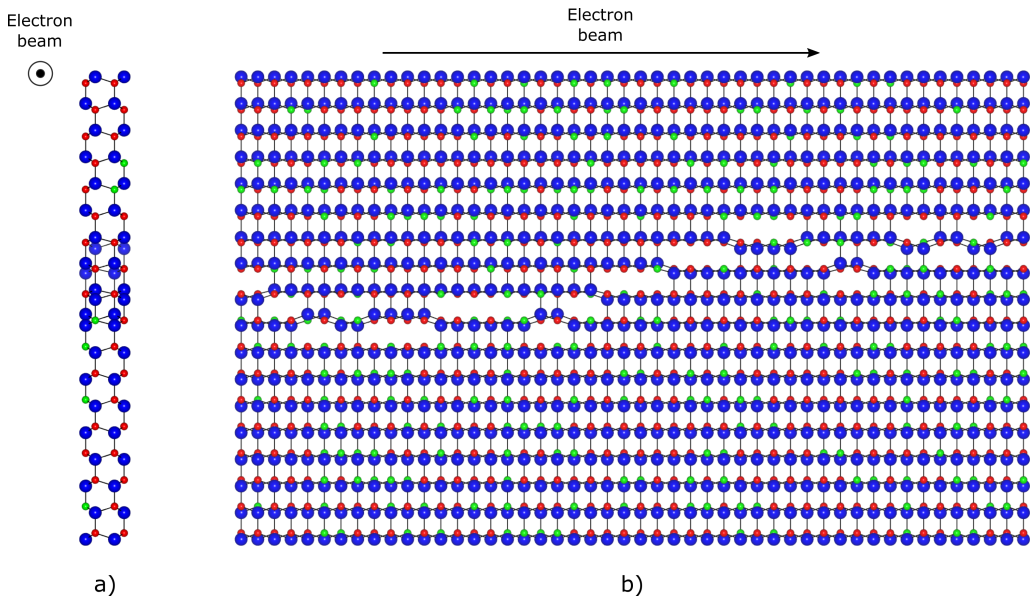

Figure 2.23.: The $Al_9O_3N_7$ super-cell, used for Z-contrast STEM simulations. a) Perpendicular to the direction of the electron beam; b) along the direction of the electron beam

For a quantitative comparison between simulated and experimental HAADF-STEM images we have estimated the thickness of the specimen in the investigated region by comparing it with HAADF-STEM simulations of AlN and Al_2O_3 for different thicknesses. According to frozen phonon simulations for AlN and Al_2O_3(see B), the experimental normalized intensity in the nitridation layer corresponds to approximately 13 nm of AlN, therefore for the analysis we used the simulated image of $Al_9O_3N_7$ structure within AlN with the thickness of 13 nm. The results of the HAADF-STEM simulation along with the experimental image are shown on fig.2.24 (a).
In the proposed structure, the IDB influences the distances of the lattice planes along the [0001] direction. The cationic positions of the "Al-polar" lattice are shifted against the "N/O-polar" lattice by approximately $c_{AlN}/4$ along [0001]. Therefore, we can evaluate the theoretical displacement of cationic positions with respect to a wurtzite-type AlN reference lattice in the N-polar part. We can also measure the shift of the HAADF-STEM intensity maxima obtained from the simulation and compare it to the shift measured in the respective experimental image (fig. 2.12). Figure 2.24 (b) shows the theoretical displacement of the cationic positions of the layer and the displacement of the contrast maxima in the simulated and the experimental STEM images for two-dimensional nitridation layer. The theoretical displacement predicts a shift of approximately 17% between the two polar lattices. The values obtained from simulated and experimental images agree well qualitatively with each other, however the measured experimental value is slightly lower than the theoretically predicted value (≈12%). We assume that this difference is

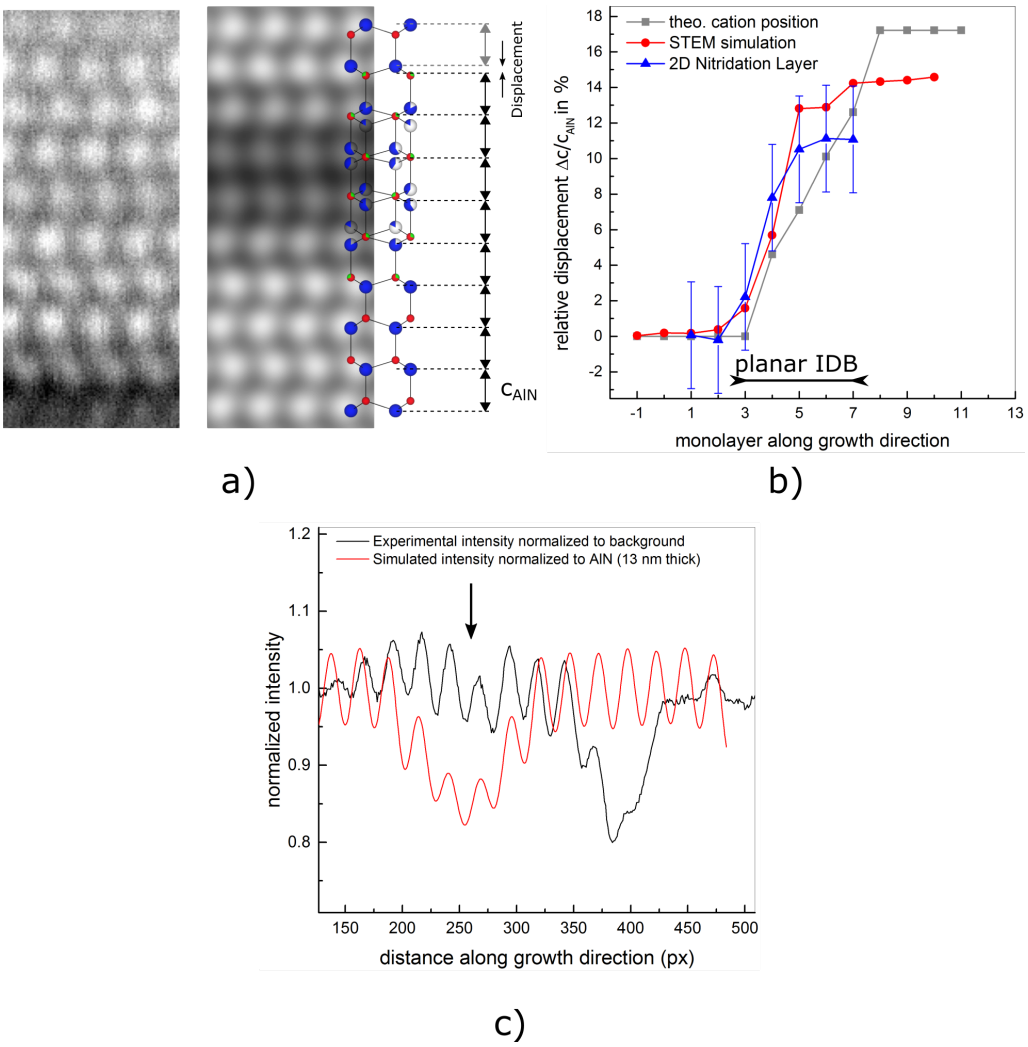

Figure 2.24.: Comparison of HAADF-STEM data of nitridation layer with Z-contrast image simulations for $Al_9O_3N_7$ IDB within AlN with the thickness of 13 nm. a) HAADF-STEM images along $[11\bar{2}0]$ direction. The ball-and-stick model is given next to image simulation. The weighted positions of the cations are marked by the dashed lines.The IDB affects the distances of the lattice planes along [0001] and result in out-of-plane displacement Δc. b) Analysis of out-of-plane displacement relative to c lattice parameter of AlN ($\Delta c/c_{\mathrm{AlN}}$) for the theoretical model of $Al_9O_3N_7$ IDB (gray), Z-contrast simulation image (red) and experimental image (blue). c) Comparison of normalized HAADF-intensity profiles of simulated and experimental images. Black arrow indicates the intensity drop at approximately 5th monolayer from the interface. The intensity drop is more pronounced in the simulated image.

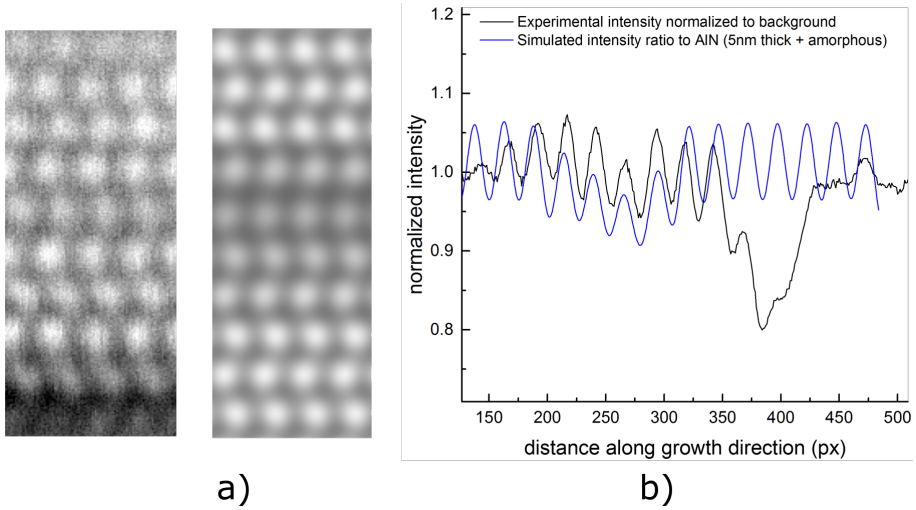

Figure 2.25.: Comparison of experimental HAADF-STEM data of nitridation layer with Z-contrast image simulations for $Al_9O_3N_7$ IDB within AlN with the thickness of 5 nm superimposed with homogeneous intensity, corresponding to the amorphous layer. a) HAADF-STEM images along $[11\bar{2}0]$ direction. b) Normalized HAADF-intensity profiles of experimental and simulation images. The value of the drop of simulated intensity at 5th monolayer from the interface agrees well with the experimentally observed intensity drop.

caused by the inhomogeneity in the thickness of the nitridation film. Due to the difference in thickness it can happen that along the observation direction the thickness of the N-polar reference lattice preceding IDB varies by 1-3 monolayers. This creates difficulties in choosing a reliable reference lattice for the evaluation of c lattice parameter displacements.

On the simulated HAADF-STEM images shown in Fig. 2.24, the reduced intensity of the IDB is caused by the reduced effective atomic number of Al-atoms, due to the statistical distribution of Al-atoms between the cation sites of "Al-polar" and "N/O-polar" sub-lattices. The intensity drop on the simulated image is more pronounced than on the experimental image, as it is seen on the intensity profiles, normalized to the background, on fig. 2.24 (c). We assume that the possible explanation for that is the amorphous layer covering the scanning area, that formed during the specimen preparation. This means, that the effective thickness of the specimen in that area is less than 13 nm and the additional intensity is caused by the presence of amorphous layer. On the fig. 2.25 is shown the result of the simulation for the 5 nm thick specimen, with the added homogeneous intensity of the amorphous layer. We observe the significant improvement in the agreement of the HAADF-contrast of the IDB in the experimental and simulated images.

Moreover, the presence of an amorphous layer may also contribute to the discrepancy observed between the measured and simulated values for c lattice parameter displacement. On the experimental image the amorphous layer above the scanned

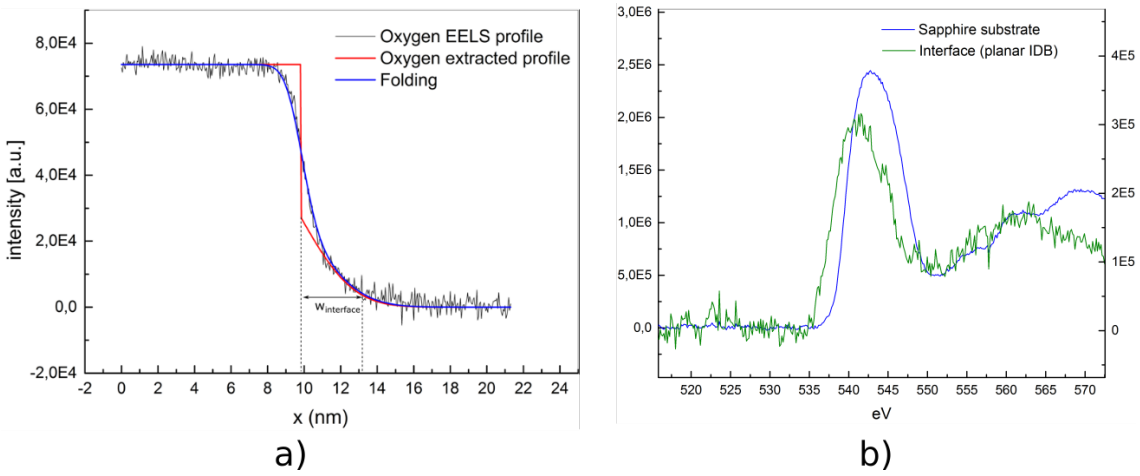

Figure 2.26.: EELS analysis of the nitridation layer at Al_2O_3/AlN interface. a) O K-edge EELS intensity profile across Al_2O_3/AlN interface. Black line corresponds to recorded intensity profile; blue -fitting of the raw profile; red – extracted O intensity signal. (for explanations see the text and A.2) b) Integrated O K-edge intensity within sapphire substrate (blue curve) and near the Al_2O_3/AlN interface. The shift of binding energies by 1.5 eV is observed.

area complicates the precise localization of intensity maxima, which results in relatively large standard deviation value (approximately, 3 %).
Based on these results, we conclude that HRTEM and HAADF-STEM observations of the continuous two-dimensional nitridation layer forming at the temperatures above 850 °C show good agreement with the phase-contrast and Z-contrast simulation of the theoretical model of rhombohedral aluminum-oxynitride – $Al_9O_3N_7$.
There are additional facts that support the hypothesis of aluminum-oxynitride formation during nitridation. First, *a*-lattice parameter of $Al_9O_3N_7$ is 3.06 Å, which is smaller than *a*-lattice parameter of AlN. The relaxation of $Al_9O_3N_7$ film on sapphire substrate will result in one additional plane every 9.55 planes in Al_2O_3, which is in a good agreement with the frequency of misfit dislocations that we observe in our experimental images. This suggests that formation of relaxed $Al_9O_3N_7$ film is more favorable under the nitridation conditions that we use in the experiment.
Additionally, we have used the electron energy-loss spectroscopy to investigate the oxygen composition near the Al_2O_3/AlN interface. In this case we investigated templates, where the initially nitridated sapphire substrate is overgrown by AlN layer at reduced temperatures. The detailed description of this structure and deposition conditions will be given in ch. 3.
The line profiles of oxygen K-edge signal, across the Al_2O_3/AlN interface is given on fig.2.26 (a). As described in 1.2.7, EELS measurements are conducted in a fast acquisition mode and a low probe current, in order to reduce the radiation damage of the specimen. The drawback of using such method is a relatively low spatial resolution, a signal delocalization and an overlapping of oxygen signal at

the interfacial area by the oxygen signal from the Al_2O_3 substrate. Therefore, it is difficult to locate oxygen on individual lattice planes at the interface.
The recorded oxygen signal can be described as a convolution of the effective oxygen distribution function ($F_0(x)$) and the measurement broadening characterized by Gaussian function ($G(x)$). Following the assumptions described in detail in appendix (see A.2) we extract the oxygen profiles (on fig. 2.26 shown by red curve). By applying the deconvolution procedure and extracting the effective oxygen signal based on our approximations, we estimate the diffusion length of oxygen atoms inside the Al-polar template to be $w_{interface} \approx 3.1$ nm (13 ML), as indicated on fig. 2.26. We have also analyzed individual spectra of O K-edges close to the interface, where nitridation layer is expected, and compared it with that in Al_2O_3. The extracted signals for O K-edges are shown on fig.2.26 (b). We observe a shift of O K-edge of about 1.5 eV to the lower binding energies within the area close to the interface, as compared to the O K-edge from the Al_2O_3 substrate. These observations may serve as an independent confirmation of oxygen incorporation at the Al_2O_3/AlN interface and suggest the presence of a $Al_9O_3N_7$ nitridation layer, which introduces the variations in local electronic configuration and bonding of oxygen atoms, resulting in the shift of binding energies.
However, we have shown that extended annealing in NH_3 gas flow at high temperature results in the formation of three-dimensional islands along with the two-dimensional layer. HRTEM and HAADF-STEM observations of three-dimensional islands do not show characteristic features that we observe on the simulated images of $Al_9O_3N_7$ model and experimental images of two-dimensional nitridation film: N- to Al-polarity inversion, reduced HAADF intensity or variations of the c lattice parameter along growth direction. Therefore, we assume that three-dimensional islands do not contain an aluminum-oxynitride $Al_9O_3N_7$ structure but consist instead of pure Al-polar AlN.

2.3.3. Conclusion

In this chapter we presented the rigorous structural analysis of the film, formed during nitridation process at different conditions. We showed that nitridation primarily results in the formation of an aluminum-oxynitride crystalline film, which form as well separated patches after 10 minutes of nitridation at 800 °C. This film transforms into a continuous film covering the whole sapphire surface when the temperature is increased to 850 °C. We showed that nitridation above 1000 °C drastically changes the morphology of the nitridation layer, resulting in an heterogeneous surface where three-dimensional islands of 10-20 nm height and density in the order of magnitude of $\sim 10^{11} cm^{-2}$ are present along with the two-dimensional nitridation layer, formed at lower temperatures.
Our HRTEM and STEM observations showed that the atomic structure of the nitridation layer significantly differs for these two types of surface morphologies. The aluminum-oxynitride two-dimensional nitridation film has N-polarity at the inter-

face, but contains a planar inversion domain boundary, which establishes Al-polarity at the top of the nitridation film. HRTEM and HAADF-STEM simulations of the proposed theoretical model of rhombohedral $Al_9O_3N_7$ showed excellent agreement with our experimental data for the two-dimensional nitridation film. The stability of the rhombohedral aluminum-oxynitride depends strongly on the growth environment and particularly on the ammonia supply.
The three-dimensional islands also establish Al-polarity of the nitridation layer and appear to be more stable under high temperature growth environment. The islands can be seen as a last step of reducing Al_2O_3 that follows the path through the AlON phase diagram from Al_2O_3 to AlN through the various $Al_xO_yN_z$ phases. Being Al-polar directly from the interface, they do not contain the unstable aluminum-oxynitride structure, responsible for polarity inversion, and thus we assume the islands to be pure AlN.
Therefore we conclude that the nitridation layer establishes Al-polarity at the end of the process, which does not depend directly on the annealing conditions applied. However the annealing conditions define the morphology and atomic structure of the nitridation layer resulting either in unstable $Al_9O_3N_7$ alone, or in an heterogeneous layer where unstable $Al_9O_3N_7$ is omni-present along with stable AlN islands. These findings enrich our understanding of the atomic structure and polarity of the nitridation layer and play a significant role in understanding the polarity control during subsequent deposition of III-nitrides films on the nitridated sapphire.

3. Impact of the low temperature buffer layer on polarity control in III-Nitrides

3.1. State of the art and motivation

The concept of introducing a buffer layer between sapphire substrate and the epitaxial GaN film was first suggested by Amano and Akasaki. [9] In their experiment they showed the improvement of crystallinity and optical properties of thick GaN films grown with the intermediate AlN buffer layer, deposited at low temperatures. Later on Nakamura applied thin GaN buffer layer grown at 600 °C which resulted in significantly increased Hall mobility, as compared to the films without buffer layer. [10]
The growth of a low temperature buffer layer in general proceeds in two steps: i) deposition of a thin epitaxial layer at low temperature (500° – 650°C) and (ii) annealing of the buffer layer at high temperature. Several researchers reported that the pre-treatment of the sapphire substrate, the thickness of the buffer layer and the annealing time are critical parameters that influence the morphology of the buffer layer itself and epitaxial films grown on top of it. [70, 100, 101]
Sumiya et.al. presented a detailed study on the dependence of the polarity of epitaxial films on the growth conditions, thickness and annealing time of the buffer layer. [102, 101]They have shown that films grown with buffer layer are initially metal-polar, however a switch to N-polar was observed when the buffer layer was annealed for too long time. Besides, they have shown that GaN films grown without buffer layer result in mixed polar films with N-polar inversion domains and exhibit rough surface morphology with hexagonal hillocks. Such morphology is an indication of N-polar films as it was confirmed by TEM observations by Rouviere et. al. [7].
Although these results are generally accepted and applied for engineering the polarity of III-nitride films, there is still lack of understanding of the fundamental atomic mechanism behind this process.
In this chapter we will study in detail GaN and AlN buffer layer deposited at low temperature on nitridated sapphire substrates and investigate their atomic structure and polarity of the layers. We will then investigate the structure of AlN layers grown without low temperature buffer layer, and conclude on the role of the buffer layer for polarity control in MOVPE growth of III-nitride films based on our analysis.

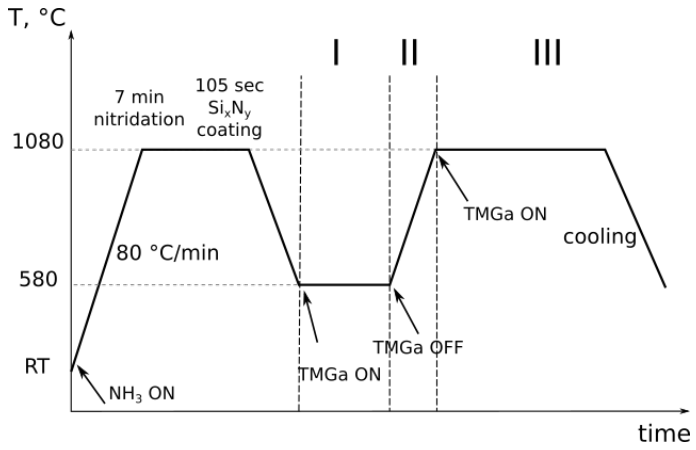

Figure 3.1.: Schematic time chart of the MOVPE growth process of GaN film versus temperature T.

3.2. Growth of III-Nitrides thick films with LT buffer layer

3.2.1. Polarity and atomic structure of GaN buffer layer

The growth procedure, described below, was optimized in previous experiments of the group and used as a standard growth recipe to achieve high-quality smooth metal polar GaN films with dislocation density in the $10^8\,cm^{-2}$ range. [103][58] Fig. 3.1 shows a schematic time chart of the main steps of GaN epi-layer growth process in terms of temperature T.

Before GaN deposition, the sapphire surface is nitridated by the flow of NH_3 gas. NH_3 is introduced at room temperature, and the sapphire surface is nitridated during the temperature ramp to 1080 °C with a rate of 80 °C/min up and then kept for 7 minutes at this temperature with NH_3 flowing (which corresponds to conditions of sample L from chapter 2). Then Si_xN_y is deposited onto the nitridation layer by introducing SiH_4 gas at the same temperature for 105 s with a flow rate of 50 sccm and a concentration $c = 250$ ppm.

The growth process of the GaN film after the pre-treatment of the sapphire surface includes three main steps, labeled as I—III on fig.3.1: deposition of a buffer layer at low temperature (I), annealing of the buffer layer (II), deposition of GaN at high temperature (III). The flow rates of trimethylgallium (TMGa) and NH_3 are 0.004 slm and 3.5 slm, respectively, which result in a V-III ratio of 16 000. An approximately 30-40 nm thin low temperature (LT) buffer layer is deposited at T = 580 °C on top of the nitridated sapphire.. After the deposition of the buffer layer, the TMGa flow is closed and the temperature is raised from 580°C up to 1080°C. This step requires 6-7 minutes and is assigned as “annealing”. After the annealing, when the temperature reaches T=1080 °C, the TMGa flow is started again and a $4\mu m$ GaN epi-layer is deposited at high temperature (HT).

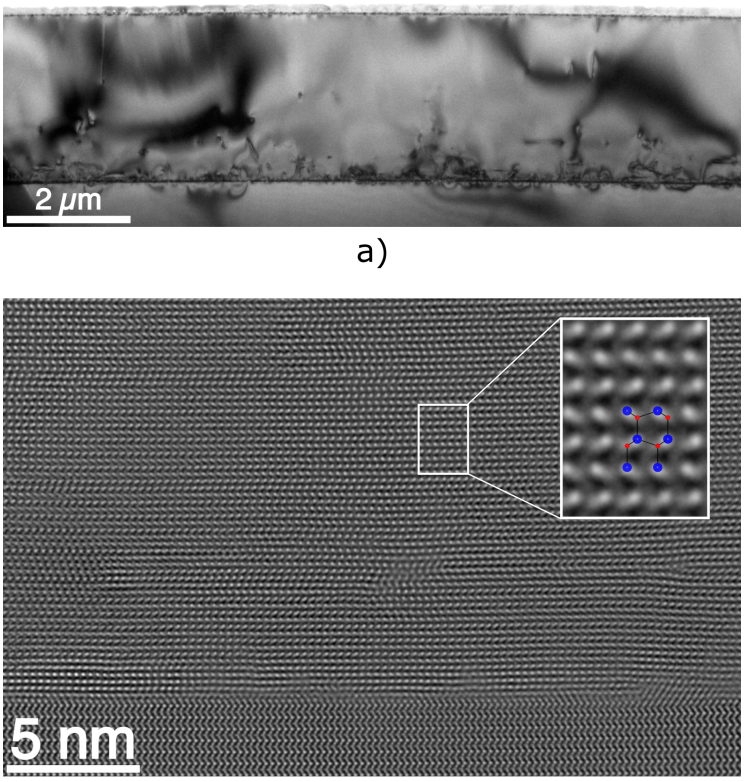

Figure 3.2.: Cross-sectional TEM observations of 4 µm thick GaN epi-layer. a) Bright-field image along [10$\bar{1}$0] direction. The layer is smooth which is characteristic for metal-polar films. b) HRTEM image along [11$\bar{2}$0] direction. Metal polarity of the layer is demonstrated on the inset.

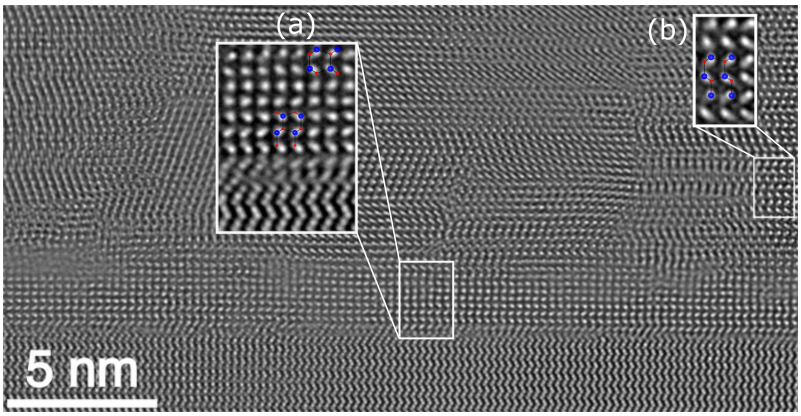

Figure 3.3.: HRTEM cross sectional image of as-deposited low temperature GaN buffer layer along[11$\bar{2}$0] projection. Magnified details on the insets (a) and (b) reveal the polarity and atomic structure of buffer layer.

A cross-sectional image of a 4 µm thick GaN film shown in fig. 3.2 (a) demonstrates that the surface of the resulting layer is smooth and without inversion domains. As it is shown on cross-section HRTEM along[11$\bar{2}$0] GaN projection (fig. 3.2 (b)) the layer is metal-polar, which is established already 10-15 nm above the interface to the sapphire substrate, i.e. within the thickness of low temperature buffer layer.
On the HRTEM image in [11$\bar{2}$0] (wurtzite) projection of the as-deposited GaN buffer layer (fig. 3.3) grains with zinc-blend and wurtzite symmetry can be distinguished. The first three monolayers above the sapphire substrate are N-polar. The polarity of the film switches to metal polarity after the 5th monolayer, as it is shown on inset (a) on fig. 3.3. Wurtzite grains in the middle of the layer have metal polarity (inset (b) on fig. 3.3).Taking into account the observations on the nitridation layer described in the previous chapter (2), we can state that the first 7-8 monolayers belong to the aluminum-oxynitride nitridation layer ($Al_9O_3N_7$). This suggests, that metal polarity of buffer layer is established through $Al_9O_3N_7$ nitridation layer.
Let us take a closer look at the atomic structure of low temperature GaN buffer layer.(fig. 3.4) The first three monolayers near the interface are N-polar, the following two monolayers do not exhibit the expected contrast of the wurtzite lattice, i.e the characteristic Al(GaN) dumbbell, and the pattern has blurred triangular shape. Starting from the sixth monolayer, the film has metal (Al or Ga) polarity. The discontinuity in the stacking sequence, characteristic to the planar inversion domain boundary, is present and shown on fig. 3.4: the first three monolayers follow the sequence $\alpha\beta\alpha$, as expected for the wurtzite lattice, which ends end with a α-stacked layer. The sixth Al-polar monolayer is also α'-stacked layer, instead of having the expected β-stacking. On the HAADF-STEM image (fig.3.4(b)) the GaN buffer layer is recognized by a higher intensity when compared to the Al_2O_3 substrate and the $Al_9O_3N_7$ nitridation layer, since Ga-atoms have higher atomic number than Al-atoms. The interface between the GaN buffer layer and the underlying nitridation layer is atomically abrupt. We may compare the HAADF-intensities across the interface $Al_2O_3/Al_9O_3N_7/GaN$ interface with the theoretically calculated HAADF-intensities of Al_2O_3, AlN and GaN as a function of simulation cell thickness (see B). For the typical thicknesses of TEM specimen of 20 nm, the theoretical value of $I_{\mathrm{GaN}}/I_{\mathrm{Al_2O_3}} \approx 3$ and the $I_{\mathrm{AlN}}/I_{\mathrm{Al_2O_3}} \approx 1$. These values agree well with the experimentally observed HAADF-intensities of GaN and nitridation layer, normalized to HAADF-intensity of sapphire substrate: $I_{GaN}/I_{\mathrm{Al_2O_3}} \approx 2.8$ and $I_{\mathrm{nitridation}}/I_{\mathrm{Al_2O_3}} \approx 0.9$ as it is seen on fig. 3.4 (c). We also observe 2 monolayers with a reduced HAADF-intensity after five monolayers of the nitridation layer, which are indicated by a small verical arrow on fig.3.4 (c). An analysis of the lattice displacements for the HAADF-STEM image of GaN buffer layer with respect to the AlN c lattice parameter (fig. 3.4(d)) reveals a shift of approximately 17% after the fourth monolayer. The shift is followed by a linear increase of the displacement, which matches the larger c lattice parameter of GaN as indicated by the theoretical curve for GaN on AlN (black line on fig. 3.4(d)).

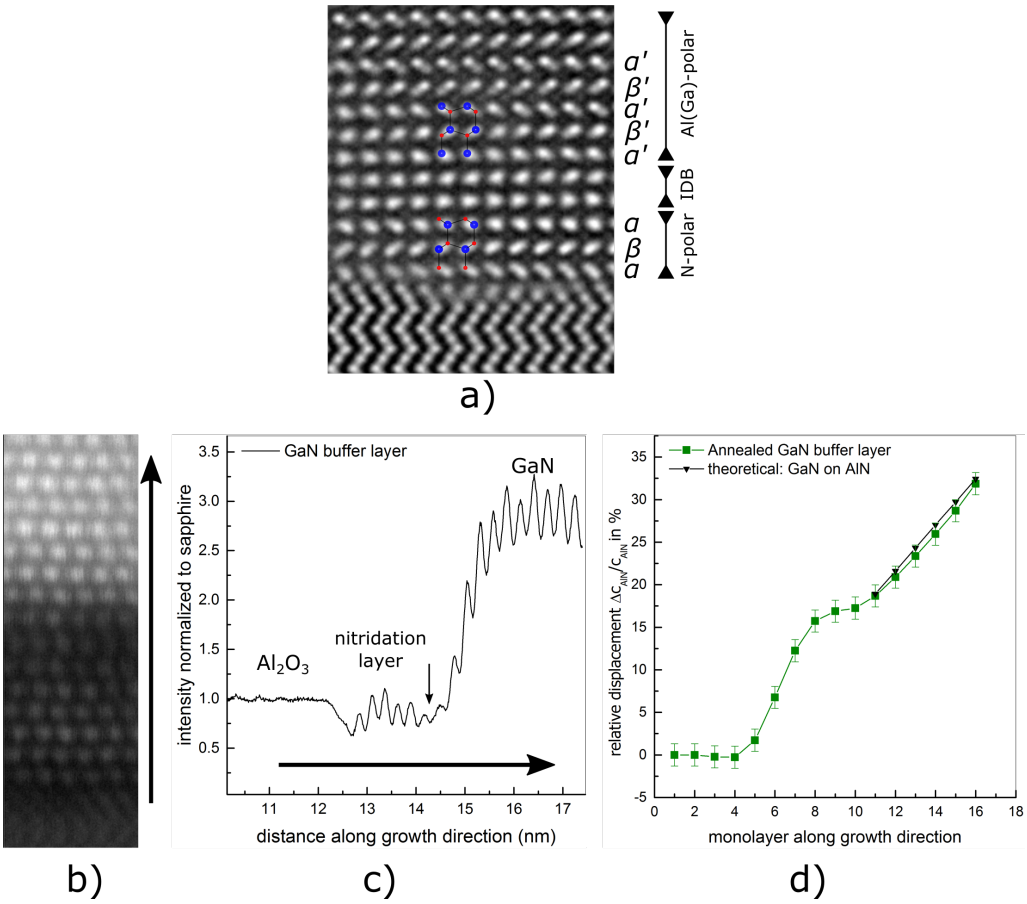

Figure 3.4.: HRTEM and HAADF-STEM analysis of a GaN buffer layer near the interface with the sapphire substrate. a) HRTEM image along $[11\bar{2}0]$ projection of GaN. The first three monolayers are N-polar and follow the stacking sequence $\alpha\beta\alpha$. From the 6th monolayer the layer has metal polarity and $\alpha'\beta'\alpha'$... stacking sequence. The 4th and 5th monolayers switch the polarity and introduce a discontinuity in the stacking sequence. b) HAADF-STEM image of GaN buffer layer along $[11\bar{2}0]$ GaN projection. Black arrow denotes the direction of intensity line-profile on (c). c) Line profile of normalized HAADF-intensity across the interface. Small arrow indicates monolayers with a reduced intensity between nitridation aluminum-oxynitride layer and GaN buffer layer. d) Displacement of c lattice parameter of GaN buffer layer along the growth direction relative to AlN lattice.

3.2.2. Polarity and atomic structure of AlN buffer layer[1]

The investigated metal-polar AlN templates are grown following a growth procedure, which has been optimized by previous experiments of the group of Z.Sitar of North Carolina State University. The growth is done in a low pressure vertical reactor at P = 27 mbar. Epi-ready *c*-plane sapphire substrates are first annealed in vacuum and then etched in H_2 at 1050 °C. The substrates are subsequently nitrided in NH_3 ambient with N_2 acting as a carrier gas during 4 minutes at 950 °C. The low-temperature AlN buffer layer is deposited at 650 °C with NH_3 and trimethylaluminum (TMAl) as a precursor. The V-III ratio is about 13 000. The buffer is then annealed in $NH_3 + N_2$ atmosphere during 15 minutes at 1050 °C. The thickness of the annealed buffer layer is expected to be around 20 nm. Afterwards, a 150–200 nm thick AlN film is grown at a temperature of 1100 °C with a V-III ratio of 2000 on top of the nitridated sapphire.
HRTEM image (fig. 3.5 (a)) shows the Al_2O_3/AlN interface projected on the AlN $[11\bar{2}0]$ orientation. The polarity of the film changes after 8 ML above the interface from N- to Al-polar. The assignment of the polarity of the two monolayers between N-polar and Al-polar AlN is not possible. The transition of the polarity comes along with the violation of the stacking sequence of a regular wurtzite lattice, which is assigned on fig. 3.5 by $\alpha\beta$ for the N-polar and α' β' for the Al-polar material. On the HAADF-STEM image 3.5 (b) the analysis of the polarity from the tunnel positions confirms the inversion from N- to Al-polarity independently from HRTEM. The reduced HAADF-intensity of the 9th and 10th monolayers is observed on the HAADF-STEM image (fig. 3.5 (a)) and on the corresponding line profile of normalized intensity across the interface of Al_2O_3/AlN (fig. 3.5 (c)). Figure 3.5 (d) shows the relative displacement of 17% of the intensity maxima in the experimental HAADF-STEM images for AlN buffer layer with respect to AlN *c* lattice parameter.

3.3. Growth of III-Nitrides thick films without LT buffer layer

In the following we will show results from a sample grown without low temperature buffer layer. The c-plane sapphire substrate surface preparation included annealing in vacuum and etching in H_2 at 1050 °C, followed by nitridation in NH_3 ambient with N_2 for 10 minutes at 1090 °C, repeating the conditions described in the previous section (3.2.2). Afterwards, a 150-200 nm of thick AlN layer was deposited at 1100 °C directly on the nitridated sapphire surface.
As we see on the HRTEM image shown in figure 3.6 (a) the layer is N-polar and no aluminum-oxynitride polarity inverting structure is observed. HAADF-STEM

[1]The data of HRTEM and HAADF-STEM investigations of AlN templates was contributed by Stefan Mohn. It is a result of his study of AlN templates grown on Al_2O_3 substrates by MOVPE and provided by Z.Sitar group from North Carolina State University. The results are published as a part of common work in [1].

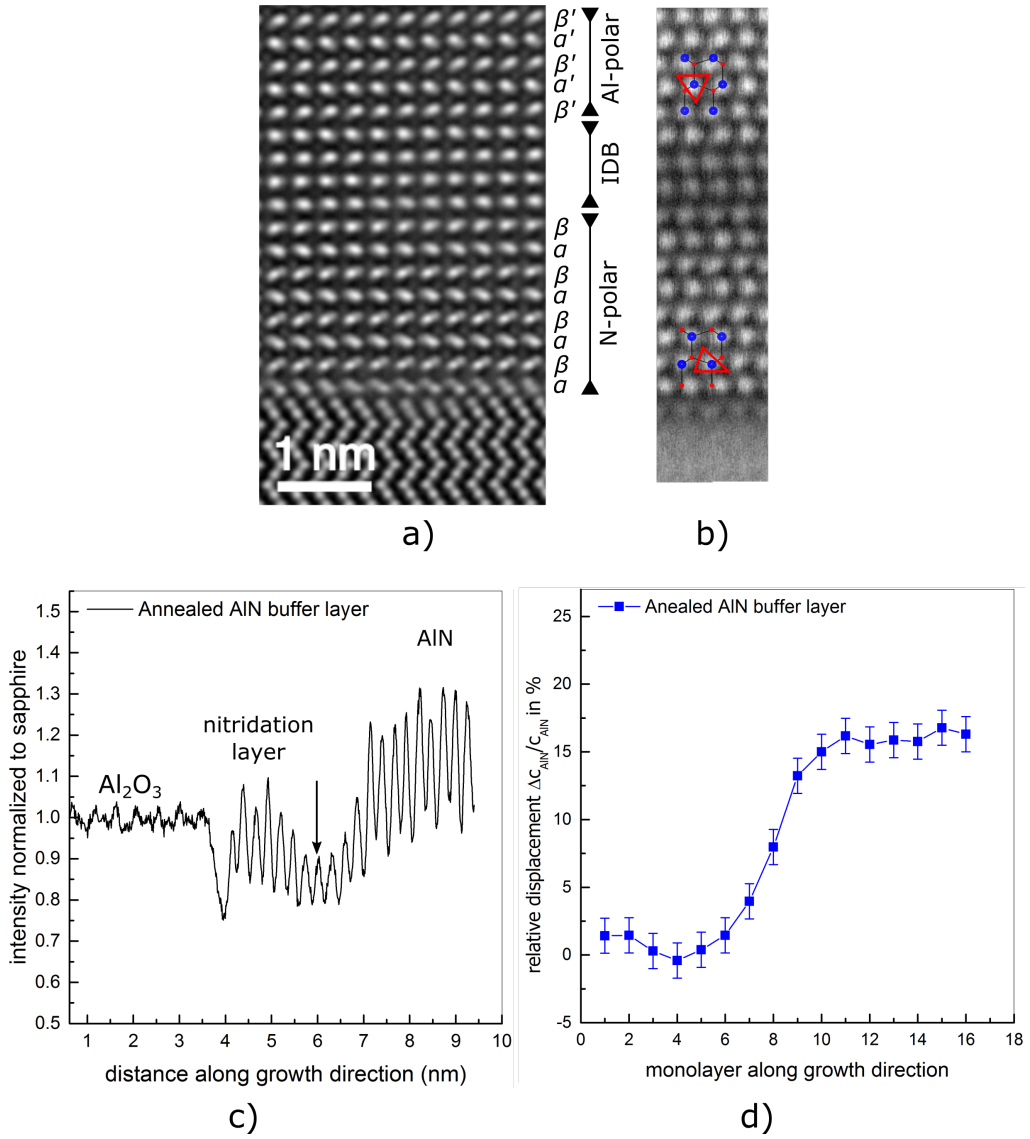

Figure 3.5.: HRTEM and HAADF-STEM analysis of low temperature AlN buffer layer of AlN near the interface with sapphire substrate. b) HRTEM image along along $[11\bar{2}0]$ projection of AlN. First 8 monolayers are N-polar and follow the stacking sequence $\alpha\beta\alpha\beta$.... From the 13th monoayer the layer has metal polarity and $\beta'\alpha'\beta'\alpha'$... stacking sequence. 9-12 monolayers invert the polarity and introduce a discontinuity in stacking sequence. b) HAADF-STEM image in $[11\bar{2}0]$ projection. Polarity of the layer is confirmed by determining tunneling positions, which are located at vertices of green triangles. c) Line profile of normalized HAADF-intensity across the interface. Arrow indicates monolayers with a reduced intensity between nitridation aluminum-oxynitride layer and AlN buffer. d) Displacement of c lattice parameter along the growth direction relative to AlN reference lattice. A relative increase of 17% is observed between 6th and 11th monolayer.

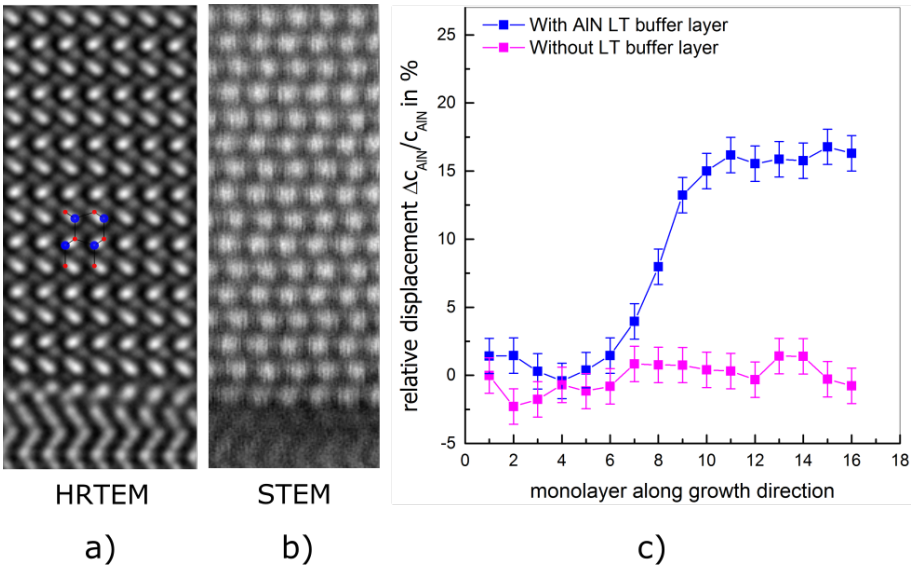

Figure 3.6.: Analysis of the microstructure of an AlN layer grown without low temperature buffer layer. a) HRTEM cross sectional images along the $[11\bar{2}0]$ projection. The layer is N-polar, no stacking discontinuity is present. b) HAADF-STEM image in $[11\bar{2}0]$ projection. The HAADF-intensity is even, no monolayers with reduced intensity is observed. c) Comparison of displacements of c lattice parameter along the growth direction relative to AlN reference lattice for AlN layer grown with (blue curve) and without (magenta curve) low temperature buffer layer. No relative increase of c lattice parameter is present in AlN grown without buffer layer.

observations confirm that the layer is N-polar. (3.6 (b)) On the HAADF-STEM image we do not observe monolayers with reduced intensity across the Al_2O_3/AlN interface (fig. 3.6 (c)). The measurement of the relative displacement of c lattice parameter shown on fig. 3.6(c) reveals no noticeable shift in the films without low temperature AlN layer, as compared to the shift of c lattice parameter of 17% observed earlier in the films with low temperature buffer layer.

3.4. Discussion

In this chapter we have performed a structural analysis of thick GaN and AlN epilayers grown on sapphire substrate with an intermediate low temperature buffer and without it.
Taking in account the main results shown in this chapter and the results from the previous chapter concerning sapphire nitridation (2), we may now consider the role that the low temperature buffer layer plays in establishing polarity in GaN/AlN films.
Earlier we have shown, that nitridation of the sapphire substrate at a temperatures above 850 °C results in the formation of a rhombohedral aluminum-oxynitride ($Al_9O_3N_7$) layer, the thickness of which depends on the annealing temperature and may vary between 5 and 10 monolayers. The nitridation layer contains a planar IDB, which promotes the inversion from N-polarity at the interface with the sapphire substrate to Al-polarity at the top, as schematically represented on 3.7 (a). Apart from

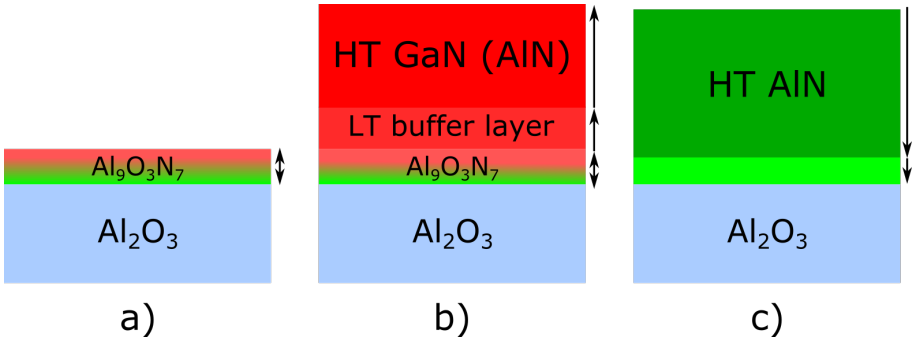

Figure 3.7.: Schematic representation of polarity control scenario in MOVPE growth of III-N layers. a) Initial sapphire annealing in NH_3 results in aluminum-oxynitride film, which induces the inversion from N polarity at the interface with the sapphire substrate to Al polarity at the top monolayers. b) Low temperature buffer layer (AlN or GaN) preserves metal polarity, established by nitridation film. Epitaxial film deposited over a buffer layer at high temperature is metal-polar. c) Epitaxial film deposited at high temperature directly on aluminum-oxynitride layer is N-polar, due to partial decomposition of polarity-inverting $Al_9O_3N_7$ layer. (Green color and downwards pointing arrow denote N-polarity; Red color and upwards pointing arrow denote metal-polarity.)

the inversion of polarity, the structure is characterized on HRTEM images by the disruption of the wurtzite stacking sequence. On HAADF-STEM images, the structure is characterized by a reduced intensity within the planar IDB and a relative displacement of the *c*-lattice parameter that reaches 15-20% as predicted by STEM simulations for the super-cell of $Al_9O_3N_7$ planar IDB surrounded by AlN.
In this chapter we have shown that a GaN buffer layer deposited at low temperature on a nitridated sapphire surface has metal polarity. The nitridation layer is still present and the interface between the nitridation layer and the GaN buffer layer is distinct on the HAADF-STEM images due to the difference in atomic numbers of Al and Ga. The planar IDB and the characteristic features of rhombohedral $Al_9O_3N_7$ are also observed. A similar behavior was observed in the case when low temperature AlN layer was deposited after nitridation: a rhombohedral aluminum-oxynitride film is observed within first 10 monolayers and followed by Al-polar AlN. Additionally, we have investigated AlN film, where the low temperature buffer deposition step is omitted and AlN is deposited at high temperature directly on the nitridated sapphire. We have shown that the AlN layer is N-polar in this case and none of the characteristic indications of $Al_9O_3N_7$ are observed in this case.
In conclusion, we have shown that low temperature buffer layer, deposited at relatively low temperatures (500 °C – 600 °C) on nitridated sapphire substrate, preserves the topmost Al-polar monolayers of $Al_9O_3N_7$ structure and inherits its metal polarity. The following high temperature deposition of thick AlN/GaN film over the buffer layer do not influence the established metal polarity. Since the polarity inverting structure of $Al_9O_3N_7$ is formed during the nitridation process, the material of the buffer layer do not influence this mechanism and both GaN and AlN buffer layers act in the same way (fig. 3.7 (b)). When the low temperature buffer layer is omitted and AlN film is deposited directly on the nitridated sapphire, we assume that planar inversion domain boundary of $Al_9O_3N_7$ dissolves in high-temperature epitaxial environments, thus establishing the N-polar monolayers of nitridation layer near sapphire interface. The AlN layer deposited on top of it inherits its polarity and results in predominantly N-polar AlN film. (see fig. 3.7 (c))
We have shown, that a low temperature buffer layer itself is not responsible for establishing metal or nitrogen polarity of the film, because the metal polarity is already established during the preceding step of nitridation. However, we may now apply our polarity control model to the results concerning the annealing of the buffer layer, described in literature. Sumiya et.al have shown that the annealing environment (V-III ratio, pressure, carrier gases) and its duration result in mixed polar and N-polar films. [102, 101]It is known, that an initially continuous buffer layer (schematically shown on 3.8) transforms into three-dimensional truncated pyramids during high-temperature annealing, as it is shown on 3.8 (a) and (c). [103, 100] In our experiment, the GaN buffer layer is annealed during temperature ramp (6-7 minutes) and is still present on top of the aluminum-oxynitride layer formed during nitridation and plays a protective role in preserving metal polarity. However, we suppose, that an increase in annealing duration or changing the annealing conditions

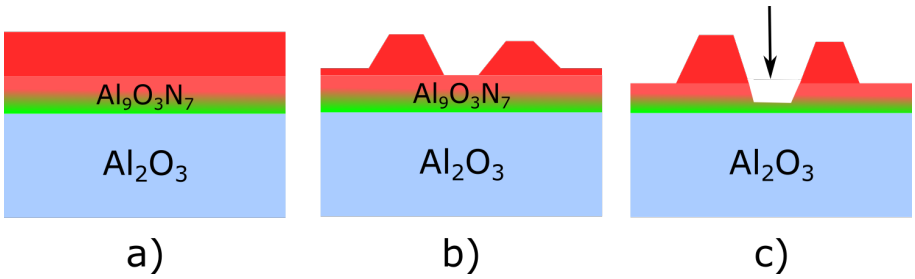

Figure 3.8.: Schematic representation of the effect of buffer layer annealing.(Color legend is the same as on 3.7) a) As-deposited low temperature buffer layer is continuous and completely covers nitridation layer. b) After annealing at high temperature buffer layer transforms into three-dimensional pyramids. c) Changing annealing conditions may enhance etching of buffer layer and partially reveal nitridation layer. During subsequent high temperature deposition N-polar inversion domains will grow on the areas, not protected by LT buffer layer. (shown by arrows).

may lead to the increased etching rate of the buffer layer and reveal the underlying $Al_9O_3N_7$ film (3.8 (d)). This will result in unwanted N-polar inversion domains, growing through the openings in buffer layer, which will consequently lead to mixed polar films with rough surface during the following deposition of epi-layer at high temperatures.

To summarize, the results presented in this chapter and in the previous one (2) have allowed us to propose a complete scenario of the establishment of N- and metal polarity in III-N heterostructures, grown on sapphire substrates. However, obtaining pure N-polar III-Nitride films is still challenging and our results may be useful for deepening the understanding of N-polar growth of III-nitride material. The next chapter is dedicated to the question how the polarity homogeneity of N-polar AlN films can be improved.

4. Influence of sapphire nitridation conditions on the polarity homogeneity in N-polar AlN films

4.1. Motivation

In the previous chapters we have shown that using methods such as sapphire nitridation and insertion of a low temperature buffer layer allows to grow smooth and inversion domain free metal-polar films. However, as it was shown by numerous authors N-polar films grown by MOVPE still can not approach a quality comparable to metal-polar films. N-polar films usually suffer from a rough surface morphology and the presence of inversion domains with metal polarity (ID). [7, 15, 16, 17] Since inversion domains have a negative impact on the electrical properties of the resulting devices, growth recipes allowing to suppress their formation are of major importance. Much effort has been devoted in the last years to reduce their density in N-polar AlN and GaN epitaxial films by changing the pre-growth treatment of the sapphire substrate [104], applying complex growth modulation techniques [88, 105, 106], or using miscut sapphire substrate [107]. The origin of inversion domains has been discussed in a number of papers however no conclusive model of their formation has been presented yet. The recipe generally applied for achieving N-polar films includes the preparation of sapphire surface by etching in a H_2 atmosphere at high temperatures (>1000 °C) and optionally sapphire nitridation at comparable temperatures. After that, an AlN film is deposited at temperatures typically above 1100 °C. Elevated growth temperatures are required in order to increase the surface migration of Al atoms and thus improve the crystalline quality of AlN films, as it was shown by Ohba et.al. [108]
In the previous chapters we have shown that deposition of AlN epitaxial film at high temperature on nitridated sapphire results in N-polar films due to the dissociation of the polarity inverting $Al_9O_3N_7$ structure formed during sapphire nitridation. In this chapter we will discuss the limitations of the proposed polarity control model and the particular problems arising in attempts to achieve pure N-polar AlN films with good crystalline quality. We will discuss the relation between the processes during nitridation of the sapphire substrate and the microstructure of N-polar AlN films grown by MOVPE.

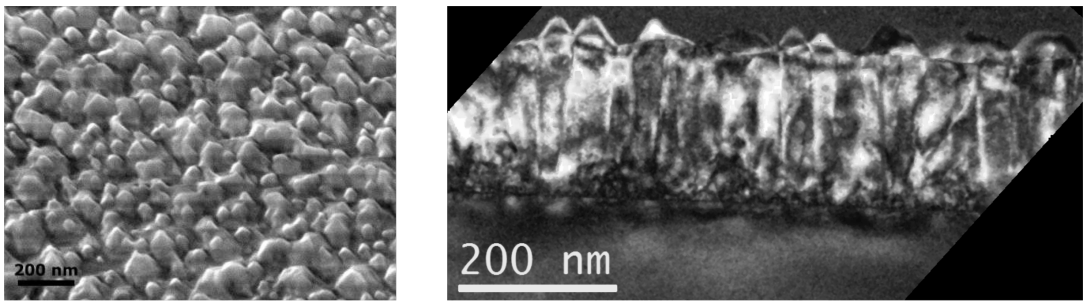

Figure 4.1.: AlN layer deposited at high temperature on sapphire substrate pre-nitridated for 30 minutes at 1080 °C ("excessive" nitridation). a) SEM image of the surface of as-grown AlN. b) Cross-sectional dark-field image in $[10\bar{1}0]_{\mathrm{AlN}}$ zone axis. Rough surface morphology is explained by high density of crystalline columns with pyramidal tips in AlN film.

4.2. Experiments and results

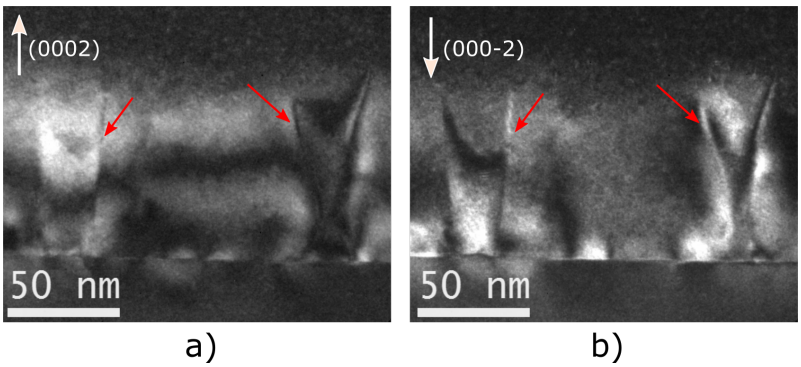

Figure 4.2.: Cross-sectional many-beam dark-field images along $[10\bar{1}0]_{\mathrm{AlN}}$ projection of N-polar AlN film grown on "excessively" nitridated sapphire substrate. a) g = (0002); b) g = $(000\bar{2})$. Red arrows are indicating contrast reversal characteristic for the presence of inversion domains.

In this chapter 200 nm thick AlN epitaxial films are deposited at 1080 °C on nitridated sapphire surface. The flow rate of TMAl during AlN layer deposition is 0.005 slm, the flow rate of NH_3 is 3.5 slm. The resulting V/III ratio is approximately 130 000. The total pressure in the reactor during the AlN deposition is 300 mbar. The growth rate of AlN films in this environment is estimated to be 0.138 µm/h. We first study the structural properties of AlN films, deposited on sapphire substrates, nitridated following the nitridation conditions of sample M from chapter 2, i.e. 30 minutes at 1080 °C. For convenience, we will refer to such nitridation conditions as "excessive" nitridation. Then we investigate an AlN layer, deposited on a sapphire substrate nitridated at 850 °C for 10 minutes, which corresponds to sample D ni-

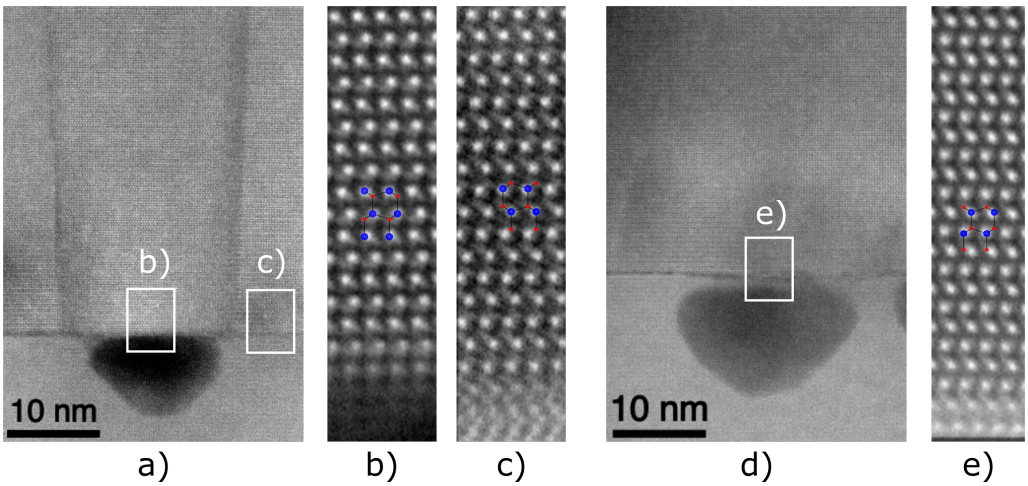

Figure 4.3.: HAADF-STEM images, along the [11$\bar{2}$0] projection, of the AlN layer, grown at 1080 °C on "excessively" nitridated sapphire substrate. a) Columnar inversion domain, situated above an hexagonal void in sapphire. b) High resolution HAADF-STEM image of the area over the void inside the inversion domain. The layer has an Al-polarity, which starts from first monolayer at the interface. c) High resolution HAADF-STEM image of the area inside the AlN matrix. The layer is N-polar. d) Hexagonal void in sapphire is not associated with an inversion domain. e) High resolution HAADF-STEM image showing N-polarity of the layer above the void on image (d). (On the magnified images (b), (c) and (e) the bright spot corresponds to Al-atom, and the grey-ish spot – to N-atom.)

tridation conditions from chapter 2. Similarly to the previous case, we will refer to such conditions as "moderate" nitridation.

Fig. 4.1(a) shows a SEM image of the AlN film deposited on "excessively" nitridated sapphire substrate. The layer exhibits a rough columnar morphology with numerous hillocks. Such morphology is usually associated with the presence of Al-polar inversion domains in N-polar films. [7, 15, 16, 17] The dark-field image in the [10$\bar{1}$0] zone axis (4.1 (b)) confirms the presence of crystalline columns with a "house-shaped" tips within the AlN layer. The width of the columns is 15-30 nm on average at the base and their side facets are inclined by 2-5° from the c-direction . Figure 4.2 shows the many-beam dark field images of the AlN film taken with g = (0002) (a) and g = (000$\bar{2}$) (b) in the [10$\bar{1}$0] zone axis. We observe inversion of contrast between the V-shaped domains and the surrounding matrix for both diffraction conditions. Such contrast reversal is a characteristic for the presence of inversion domains in non-centrosymmetric crystals, as it was discussed in sec. 1.2.3.

The HAADF-STEM image on fig. 4.3 (a) shows a V-shaped inversion domain within the AlN epitaxial film. The columnar domain is associated with an hexagonal void in the sapphire substrate. Figures 4.3 (b) and (c) show high-resolution HAADF-STEM images of magnified areas framed in white squares on fig. 4.3 (a) inside and outside the V-shaped column respectively. The high-resolution HAADF-STEM

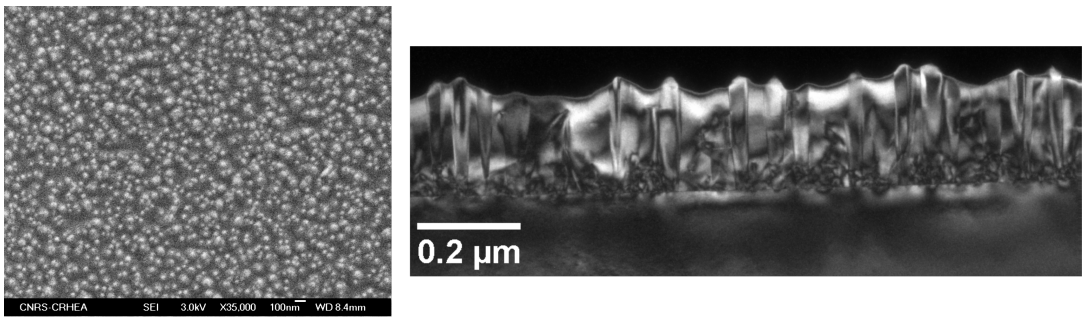

Figure 4.4.: AlN layer deposited at high temperature on sapphire substrate pre-nitridated for 10 minutes at 850 °C ("moderate" nitridation). a) SEM images of surface of as grown AlN layer. b) Cross-sectional many-beam dark-field image along $[11\bar{2}0]_{\mathrm{AlN}}$ projection, revealing the presence of crystalline columns in AlN layer.

images are acquired with the probe-corrected NION Ultrastem microscope, whose spatial resolution allows to identify Al and N atomic columns separately and thus directly determine polarity of the film. (see 1.2) Aluminum atomic columns appear with higher intensity, while nitrogen atomic columns appear with lower intensity, due to the difference in atomic numbers. The layer outside the V-shaped column (fig. 4.3 (c)) is N-polar, starting from the interface with the Al_2O_3 substrate. The V-shaped inversion domain is Al-polar from the first monolayer (Fig. 4.3 (b)). Note that not every void induces inversion domain, but we also observe voids with N-polar layer above it. (fig. 4.3 (d),(e)).
Fig. 4.4(a) shows an SEM image of the AlN film deposited on a "moderately" nitridated sapphire substrate. The resulting AlN film has a rough morphology with hillocks and tips, similar to the morphology of the previously studied sample. The dark-field image in $[11\bar{2}0]$ projection of AlN (fig. 4.4 (b)) reveals the presence of columnar domains in the AlN film grown on "excessively" nitridated sapphire substrate. The density of the domains estimated from TEM images is in the range of $10^{10} cm^{-2}$ and is comparable in both cases. The many-beam dark-field image taken with g = (0002) and g = $(000\bar{2})$ in the $[11\bar{2}0]$ zone axis, shown in fig. 4.5 (a), confirms that the columnar domains have a polarity different from the matrix. Note, that inversion domains are also associated with hexagonal voids near the interface within the sapphire substrate.(fig. 4.5 (b))

4.3. Discussion

In this chapter we have studied the microstructure of N-polar AlN layers grown on pre-nitridated sapphire substrates. On the TEM images presented in this chapter, we have seen that an epitaxial AlN layer deposited at 1080 °C on a sapphire substrate,

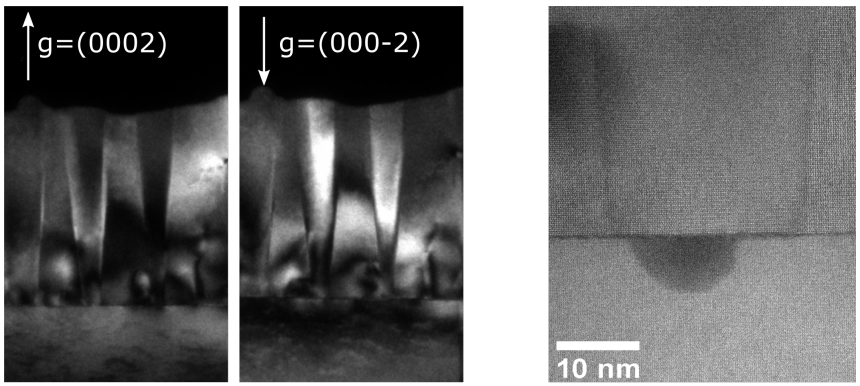

Figure 4.5.: Cross-sectional many-beam dark-field images along $[11\bar{2}0]$ projection of N-polar AlN film grown on "moderately" nitridated sapphire substrate (with g = (0002) and g = $(000\bar{2})$. b) HAADF-STEM image of the columnar inversion domain along the $[11\bar{2}0]$ projection of AlN. The domain is situated above an hexagonal void.

nitridated at the same temperature of 1080 °C for 30 minutes, is mainly N-polar but exhibits a high density of columnar Al-polar inversion domains present above hexagonal voids in sapphire. We have discussed in the previous chapter (see 3.3), that growth of AlN films directly on nitridated sapphire substrate at temperature higher than 1000 °C results in N-polar films, due to the dissociation of the polarity inverting $Al_9O_3N_7$ in high temperature growth environment.
Before we revise the mechanism proposed in 3, taking in consideration the results discussed in this chapter, let us now shortly recall the results, that we have discussed in chapter 2. We have shown that nitridation using these conditions (1080 °C, 30 minutes) results in a heterogeneous surface where two types of microstructures are observed. The sapphire surface is primarily covered with two-dimensional layer of aluminum-oxynitride, that converts the polarity of the nitridation layer from N-polar to Al-polar. (fig. 4.6 (a)) This layer is interrupted by three-dimensional AlN islands with a density of approximately $3 \times 10^{10} cm^{-2}$, which are observed exclusively above hexagonal voids in the sapphire substrate, i.e. at the sites where we have observed the Al-polar ID in epitaxial AlN layers. (fig. 4.6 (b)) These islands are Al-polar from the first monolayer and do not contain a planar inversion domain boundary. We observed by in-situ in TEM that three-dimensional islands are stable at high temperatures up to 1000 °C, while the two-dimensional $Al_9O_3N_7$ film dissociates completely at T > 850 °C when no active nitrogen is additionally supplied.
Therefore, we suggest that AlN islands, stable under high temperature growth conditions, promote Al-polar domains in the epitaxial AlN layer. Contrary the two-dimensional polarity-inverting monolayers of $Al_9O_3N_7$ decompose and induces N-polar AlN.(fig. 4.6 (c)) Hence, the layers result are heteropolar with a dominant N-polarity.

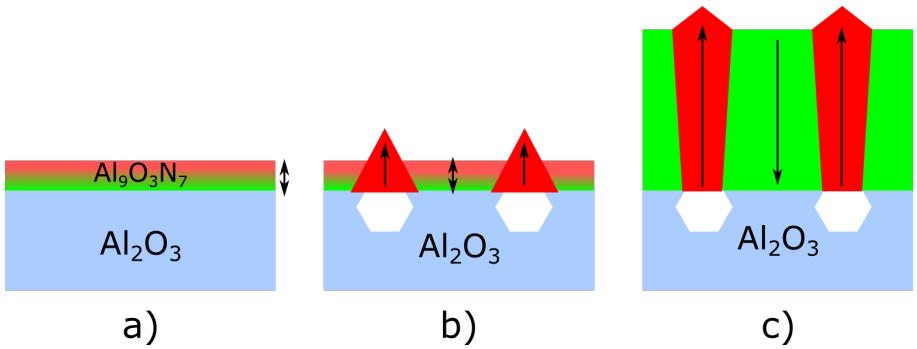

Figure 4.6.: Schematic representation of the formation mechanism of Al-polar inversion domains in N-polar AlN.(Green color and downwards pointing arrow denote N-polarity; Red color and upwards pointing arrow denote metal-polarity.) a) Initial sapphire annealing in NH_3 results in two-dimensional $Al_9O_3N_7$, which induces the inversion from N-polarity at the interface with the sapphire substrate to Al-polarity at the top monolayers. b) Excessive sapphire nitridation results in formation of stable Al-polar AlN islands above hexagonal voids in substrate in addition to $Al_9O_3N_7$ layer. c) During the high temperature growth, the AlN islands promote Al-polar domains in the layer, while the two-dimensional polarity-inverting $Al_9O_3N_7$ partially decomposes resulting in N-polarity.

Our results shed new light on the challenge to achieve homopolar layers in case of N-polar growth and suggest that, in the case of growing N-polar films, proper control of the nitridation process is more crucial than in the case of metal polar films. In fact, care should be taken in order to prevent the formation of AlN islands. To prove our hypothesis we modified the nitridation step in the growth procedure of AlN epitaxial film in order to prevent the formation of AlN hillocks during nitridation. We applied "moderate" nitridation conditions where the sapphire substrate is annealed at 850 °C for 10 minutes before AlN deposition. From the AFM and TEM analysis described in the chapter 2, we know that 10 minutes of sapphire nitridation at 850 °C results in a smooth two-dimensional $Al_9O_3N_7$ film with no AlN islands nor hexagonal voids present on the surface. On the SEM image of the resulting layer we observe that the morphology of the AlN surface is similar to that of the AlN films, deposited on "excessively" nitridated substrates. The density and the shape of the inversion domains is also comparable. Besides, we observe hexagonal voids underneath the sapphire surface, which are not present after nitridation, as shown earlier. This leads us to the assumption, that the effective time of nitridation is extended due to the continuous annealing under NH_3 during the temperature ramp from 850 °C to the AlN growth temperature of 1080 °C.
Moreover, we suggest that a slow growth rate of AlN may also favor the formation of inversion domains. In our experiments the growth rate is about 0.138 µm/h, while for AlN film with the density of inversion domains in the range of $10^8 cm^{-2}$, reported by Paduano et.al., the growth rate of AlN is 1.3 µm/h. [88] During the initial stages of the deposition process the slow growth rate results in an effective extension of

the nitridation process in time, since the sapphire surface will be exposed for longer time to the NH_3 flow at high temperature and therefore will be prone to formation of Al-polar AlN islands, resulting in Al-polar inversion domains in N-polar AlN film, even if initial nitridation is performed at lower temperatures.
An effect, described in the literature, that could explain the extension of the effective nitridation time, is caused by parasitic reactions in the gas atmosphere, leading to the formation of AlN particles, which in turn significantly reduces the growth rate of AlN during MOVPE. [109] The probability of the parasitic reaction pathways increases at high reactor pressures, high growth temperatures and high NH_3 flow rates. [110, 111]
In consequence we corroborate that the clue to achieve smooth homopolar N-polar AlN layers with low density of inversion domains, is to suppress the formation of Al-polar AlN islands, which form due to oxygen reduction in aluminum-oxynitride nitridation film during extended sapphire nitridation. It should be done primarily by proper adjustment in duration and temperature of the nitridation process. As a part of future work, it is important to consider the strategies to increase the deposition rate on the initial stages of the subsequent growth of AlN film. This might include lowering reactor pressure, modifying the V-III ratios (reducing the flow of NH_3 or increasing the flow of TMAl) and further increasing the growth temperature of AlN layer.

5. Intentional polarity inversion via annealing in oxygen-rich atmosphere

5.1. Motivation

In chapters 2 and 3 we have discussed the effect of polarity inversion from N- to metal-polarity in AlN and GaN layers epitaxially grown by MOVPE. We have shown that the inversion of the polarity occurs during the initial stage of sapphire nitridation, when the substitution of O atoms in Al_2O_3 by N atoms from NH_3 gas leads to formation of intermediate $Al_9O_3N_7$ phase from the phase diagram of $AlN - Al_2O_3$ system. This phase has a rhombohedral crystal structure and contains a planar inversion domain boundary, where the anions sites are equally distributed between N and O atoms.(for more details see sec. 2.3.2) We may now apply this knowledge about the mechanism behind the inversion of polarity to investigate the possibility of controlled inversion of polarity in AlN films by annealing it in oxygen-rich environment.

There were few reports discussing inversion of polarity of III-nitrides films by using oxygen. Adachi et.al. showed an improved quality in the polarity homogeneity of AlN layers grown by Ga-Al liquid phase epitaxy (LPE) by in-situ increasing the oxygen partial pressure. They performed HR-TEM and EDX investigations, showing an increased oxygen concentration inside the planar IDB. [112] Wong et.al. reported on the possibility of nitrogen to gallium polarity inversion in GaN layers by introducing an intermediate AlN-AlO_x layer, which they achieved by oxidizing the AlN layer in an UV-ozone reactor. However, the atomic structure of polarity inversion region was not investigated in this study. [113]

In this chapter we will attempt to switch the polarity of mixed-polar AlN epitaxial film with dominant N-polarity and Al-polar inversion domains, that we have discussed in the previous chapter. We will investigate the microstructure of the resulting layer by methods of high-resolution probe-corrected STEM and electron energy-loss spectroscopy.

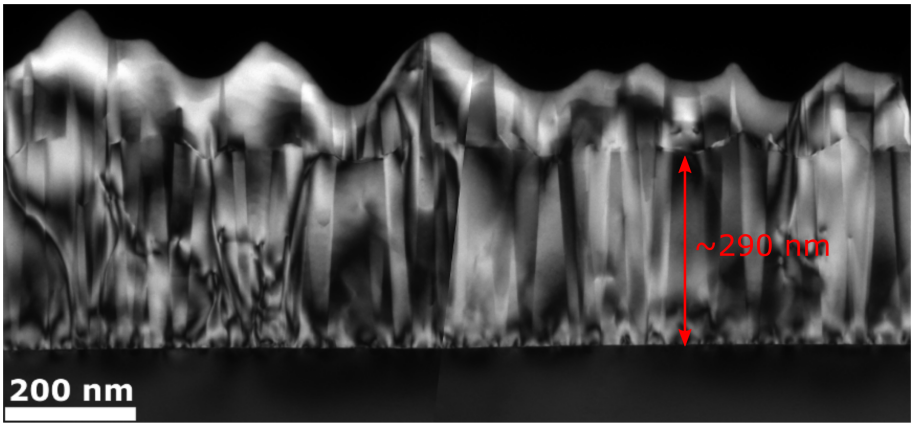

a)

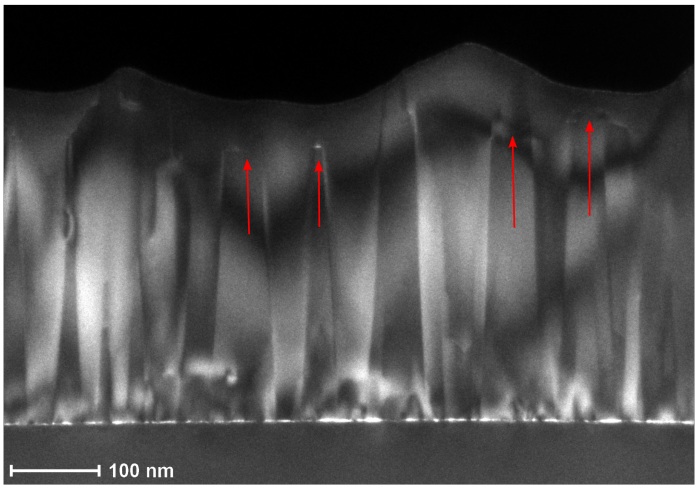

b)

Figure 5.1.: Dark-field cross-section image in two-beam conditions with g = (0002) of AlN layer grown in two steps with intermediate oxygen annealing. a) Overview image. Red arrow denotes the thickness of AlN layer, deposited during first step. The zig-zag boundary, that divides the AlN layer deposited before and after oxygen annealing step, is distinguishable. b) Magnified image showing columnar inversion domains. Red arrows point on the interruption of inclined IDBs.

5.2. Experiment and results

To study the mechanism of intentional polarity inversion by oxygen we grow a mixed polar AlN layer, following the procedure, described in the previous chapter (chapter 4). We nitridate a sapphire substrate for 30 minutes at 1080 °C in a NH_3 gas flow and then deposit 280 nm of AlN on top of it at the same temperature. After deposition of 280 nm of AlN the process is interrupted and the sample is transferred into a plasma-assisted molecular beam epitaxy (MBE) chamber. In this chamber the sample was heated up for 30 minutes under UHV conditions at a pressure of the order of 10^{-9} Torr. A flow of 0.2 sccm of oxygen and 420 W of RF power was used to generate active oxygen. The pressure in the chamber reached 10^{-6} Torr after 2 minutes of annealing under oxygen plasma and increased up to 6×10^{-6} Torr at the end of the annealing. After the annealing in oxygen plasma, the sample is transferred back to the MOCVD growth reactor, where it is overgrown with a 200 nm AlN film at 1080°C.

The dark-field cross-section TEM image in two-beam condition close to $[11\bar{2}0]$ zone axis ($g = (0002)$) shows the AlN layer at the end of the second growth step. (fig. 5.1 (a), (b)) We observe a zig-zag shaped boundary approximately at 250-300 nm away from the interface with sapphire. This may indicate structural changes in the AlN layer. As the thickness of the initially deposited AlN film is 280 nm, we can assume that this structural change corresponds to the step of growth interruption and surface oxidation. We therefore assume that the layer above the zig-zag boundary corresponds to the AlN film re-grown during the second growth step. The zig-zag boundary does not exhibit any particular preferred plane, but consists of varying curved, planar and faceted regions. Fig. 5.1 (b) shows a dark-field cross-section image with increased magnification. We observe characteristic abrupt contrast changes from bright to dark that sugest the presence of columnar inversion domains with inclined IDB, similar to those described in the previous chapter. We may notice that characteristic contrast of IDs is reduced in the upper part of the layer. Red arrows on the image point on the terminating inclined IDBs. This suggests that the upper layer contains less inversion domains and its polarity is more homogeneous as compared to the lower part of the layer.

Let us now turn to high-resolution HAADF-STEM images, acquired with the probe-corrected NION Ultrastem microscope, in order to resolve the microstructure of the zig-zag boundary and determine the polarity of the topmost AlN layer. Fig. 5.2 (a) shows a high resolution HAADF-STEM image in the $[11\bar{2}0]$ projection of the region with the faceted boundary between the AlN layers grown in the first and the second run. (see fig. 5.2 (c) for schematic representation of the investigated area). The layer below the boundary is N-polar and above it – Al-polar. The red dotted line indicate the boundary between two regions with different polarity. Fig. 5.2 (b) shows an area of two Al-polar columnar IDs with a N-polar material between them. Vertical red lines mark the inversion domain boundaries between N-polar matrix and Al-polar columnar ID. The horizontal red line indicates the planar region of the boundary between the layer grown before oxygen annealing and after it. The film

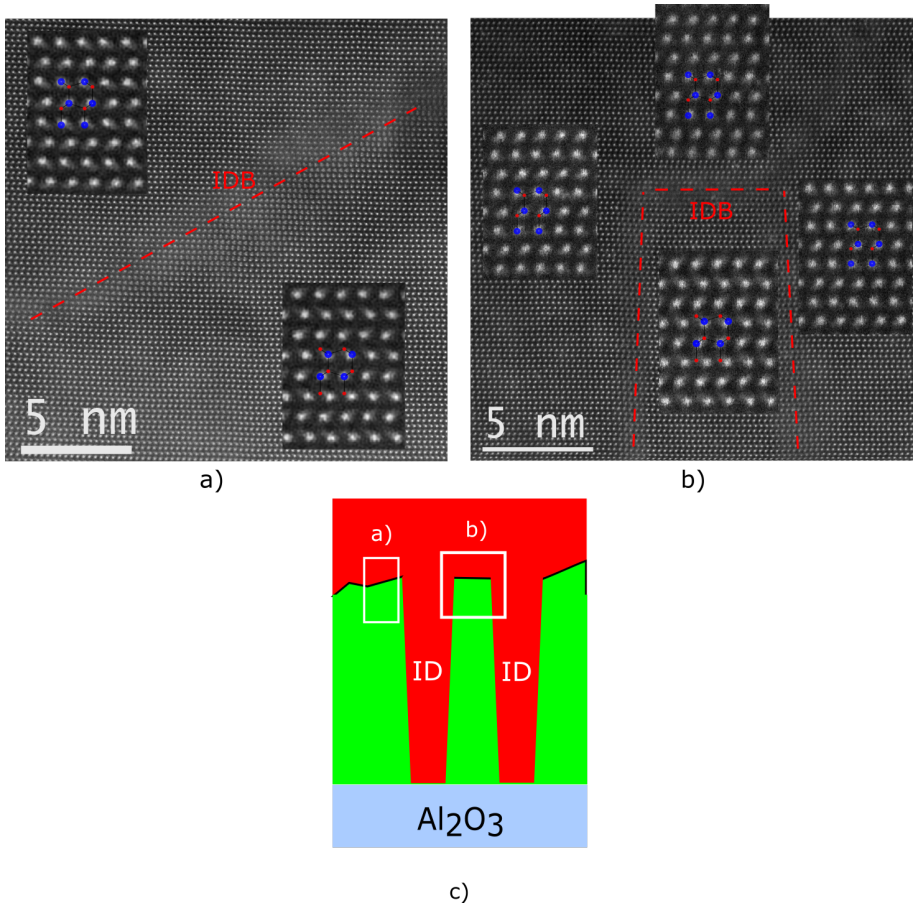

Figure 5.2.: High-resolution HAADF-STEM images of the areas near the zig-zag boundary. On schematic representation (c) the areas at which high-resolution images are taken are shown in white frames. (Red and green colors denote metal and N-polar regions of the layer, respectively.) The insets on images (a) and (b) are magnified images of the respective areas, where the polarity can be determined.

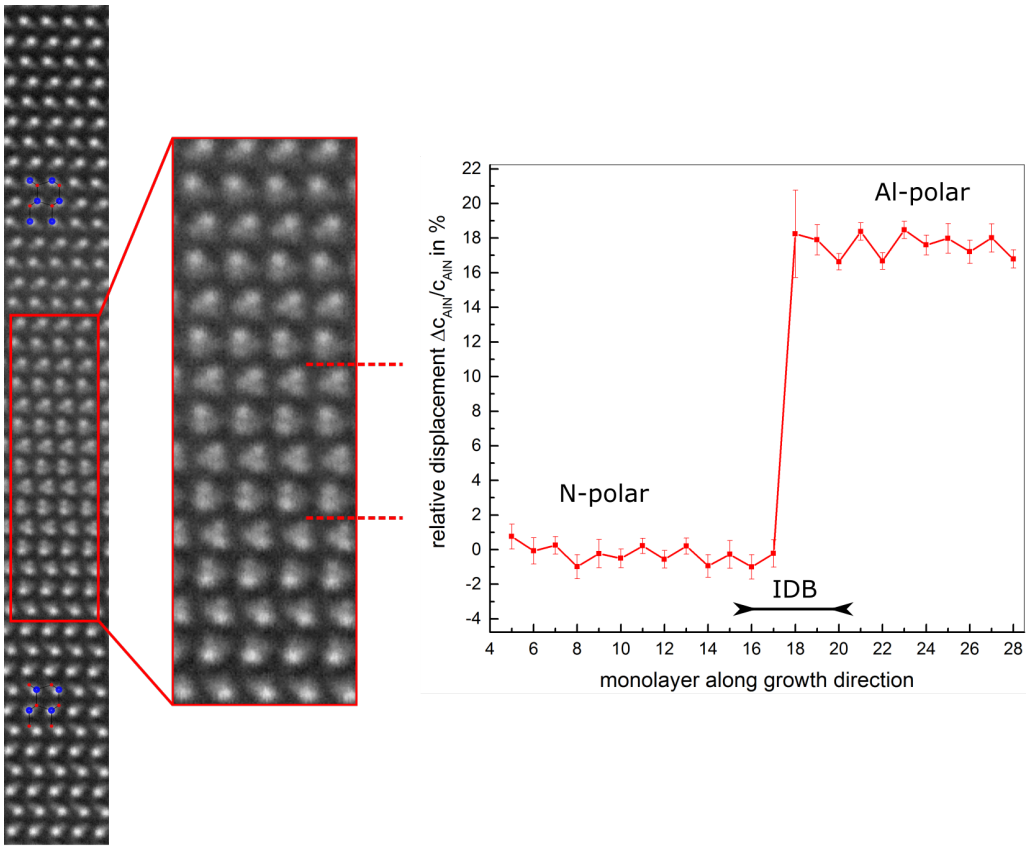

Figure 5.3.: Analysis of zig-zag inversion domain boundary microstructure. a)High-resolution HAADF-STEM image revealing the microstructure of IDB. The magnified images shows the triangular contrast within IDB. Red dashed lines delimits the areas, at whish the cation contrast is shifted towards lower or upper positions (corresponding to N- or Al-polar sub-lattices, respectively). The contrast in upper and lower cation position in the area between the dashed lines is approximately even, indicating equal occupation of these sites by Al atoms. b) Relative displacement of c-lattice parameter with respect to c_{AlN} across the area of AlN layer with zig-zag IDB.

above this line is only Al-polar, which means that the polarity of N-polar region is inverted, while the polarity of Al-polar columnar inversion domains persists. A large number of additional HR-TEM and HAADF-STEM measurements supports our observations that the layer above the zig-zag boundary is predominantly Al-polar, with a few inclusions of N-polar inversion domains. For simplicity we will refer to the regions of the zig-zag boundary, that introduce the inversion of N-polar to Al-polar AlN, as zig-zag "inversion domain boundary (IDB)".
We have "sliced" image 5.2 (a) into 10 narrow patches with similar features from the region containing inversion domain boundary, aligned them and superimposed with each other. This method allows to reduce the original image noise and thus help to resolve the atomic structure of the boundary, that inverts N-polar AlN to Al-polar AlN. The result of this procedure is shown on fig. 5.3 (a).Twelve monolayers at the bottom part of the image have the zig-zag contrast of wurtzite lattice with N-polarity, and 15 ML at the top part – wurtzite lattice with Al-polarity. The microstructure of the transition interface between two wurtzite lattices is characterized by 15 monolayers with triangular-shaped contrast. (magnified area in red rectangular of fig. 5.2 (a)) The triangular contrast is formed by two atomic columns, situated on the sites that follows the cation stacking in wurtzite below. These cations share one anion, therefore can be represented as two interpenetrating sub-lattices – "N-polar" sub-lattice and "Al-polar" sub-lattice. The HAADF-intensity of the cation columns shifts, first being higher at lower position, corresponding to "N-polar" sites (1-5 monolayer on the magnified image), then being even on both "N-polar" and "Al-polar" sites (6-9 monolayers) and at the end shifting to the upper position of "Al-polar" sites (10-15 monolayers). This indicates that the occupation of the "N-polar" cation sites is gradually decreasing, while the occupation of the "Al-polar" cation sites is accordingly increasing. We evaluated the displacement of the *c*-lattice parameter relative to the *c*-lattice parameter of AlN along the growth direction and obtained the average value of approximately 17%. (fig. 5.3 (b)).
In addition we have conducted a spatially-resolved electron energy-loss spectroscopy on the inversion domain boundary, where the polarity of AlN is switched from N- to Al-polar. Fig. 5.4(a) shows the extracted map of oxygen integrated intensity inside the area with the faceted inversion domain boundary, shown on the HAADF-STEM image which was taken simultaneously during EELS acquisition. We see that oxygen is dominantly segregated within the faceted IDB. Figure 5.4(b) displays the O/N atomic ratio along the [0001] growth direction in monolayers. We have translated the distance along the red rectangular, shown on fig.5.4(a), into the distance in monolayers along the growth direction, thus representing the faceted inversion domain boundary as planar IDB. This will help us to analyze the spacial distribution of oxygen within the IDB. The length of the extracted profile was 15.5 nm, projected onto c-direction results in 13.5 nm, which corresponds to 54 monolayers on the HAADF-STEM image taken during the EELS scanning. We have applied a Gaussian fitting function to estimate the width of the oxygen concentration profile. The calculated FWHM suggests that oxygen atoms are distributed within 4.8 ML.

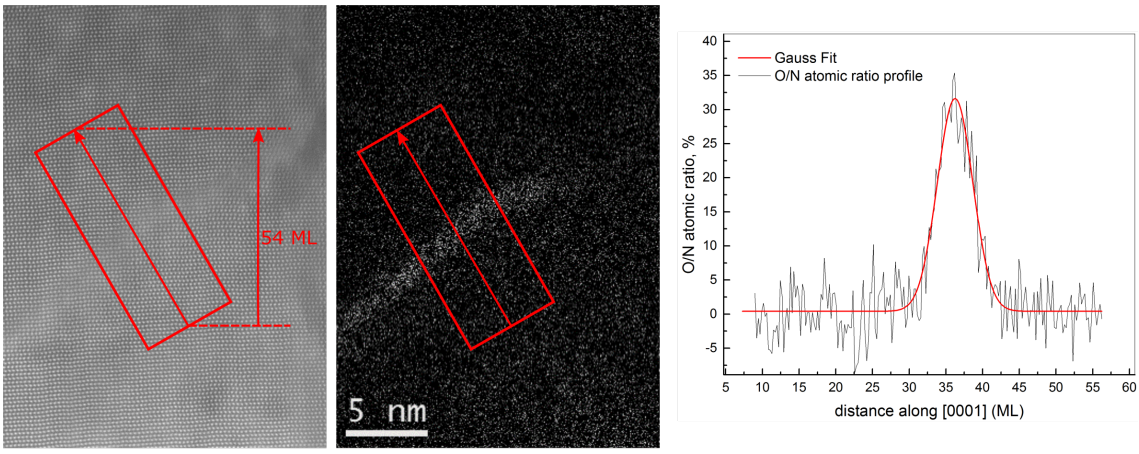

Figure 5.4.: EELS analysis of zig-zag inversion domain boundary. a) HAADF-STEM image and map of oxygen signal within this area. b) Extracted raw profile of O/N atomic ratio along red rectangular on image (a) (black line) and Gaussian fitting of this profile (red line).

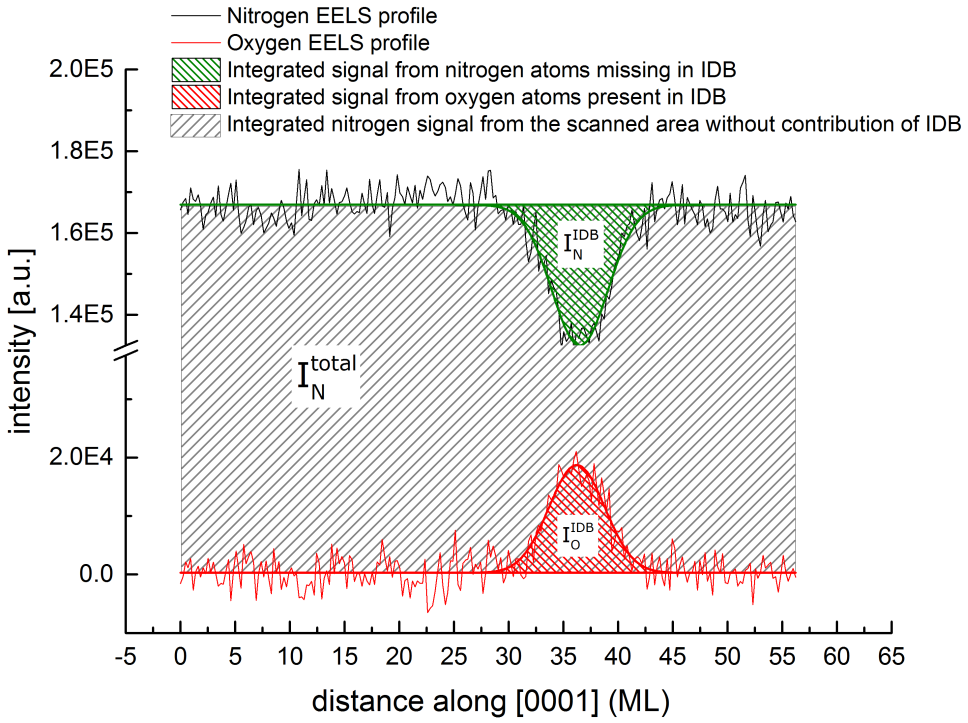

Figure 5.5.: Integrated O and N signal intensity profiles across the area with IDB.

Let us now estimate the actual concentration of oxygen atoms within the width of 4.8 ML in IDB. We have discussed in 1.2.6 that the composition ratio of the analyzed elements is proportional to the intensities of the corresponding signals:

$$\frac{C_O}{C_N} = k \times \frac{I_O}{I_N}, \tag{5.1}$$

where k is the ratio of partial scattering cross-sections for O and N for the used experimental convergence and collection semi-angles.
We have extracted the unknown k-factor from the EELS measurements of the Al_2O_3/AlN interfaces, as if the concentrations of O atoms in Al_2O_3 and N atoms inAlN are known. (see A.1 for the details) Since we applied the same experimental conditions during the EELS measurements of the zig-zag boundary in AlN film, we can use the value for the correction factor, estimated from the measurements of Al_2O_3/AlN interfaces : $k \approx 2.24$.
Fig. 5.5 shows the line profiles of extracted oxygen and nitrogen signals integrated within the 50 eV energy window across the IDB. On this image I_O^{IDB} is the area below the Gauss fitting of oxygen profile across the IDB, which corresponds to the integrated oxygen signal from the investigated sample volume. I_N^{Total} – integrated nitrogen signal if no IDB were present within the scanned volume (or, if the IDB had the same concentration of N atoms as the AlN outside it). On fig. 5.5 I_N^{Total} corresponds to the area confined by the gray rectangular. I_N^{IDB}– the integrated signal, that would be given by nitrogen atoms, missing within the IDB. The area below the black curve corresponds to the integrated nitrogen signal within the scanned area. This area can be represented as a difference of two components: $I_N^{Total} - I_N^{IDB}$.
We can estimate the number of missing monolayers of nitrogen within the investigated sample volume by the following formula:

$$C_N^{IDB} = \frac{I_N^{IDB}}{I_N^{Total}} \times 54\text{ML} = 1.27\text{ML}$$

Following the eq. 5.1 for the relation between signal intensities and element concentrations, we find the ratio between concentration of oxygen atoms within the IDB and nitrogen atoms missing in the IDB:

$$\frac{C_O^{IDB}}{C_N^{IDB}} = k \times \frac{I_O^{IDB}}{I_N^{IDB}}$$

As we estimated the concentration of missing nitrogen atoms to be 1.27 ML and we know the integrated signal intensity I_N^{IDB}, the oxygen concentration (in monolayers) is:

$$C_O^{IDB} = k \times \frac{I_O^{IDB}}{I_N^{IDB}} \times 1.27\text{ML} = 1.5\text{ML}$$

Therefore the observed integrated intensity of oxygen signal within the studied volume corresponds to approximately 1.5 full monolayers of oxygen present within the IDB region. It means that the concentration equal to 1.5 full monolayers of oxygen is distributed within 4.8 ML of inversion domain boundary structure. This will result in the average of 30% oxygen occupation of the anion positions within the IDB.

5.3. Discussion

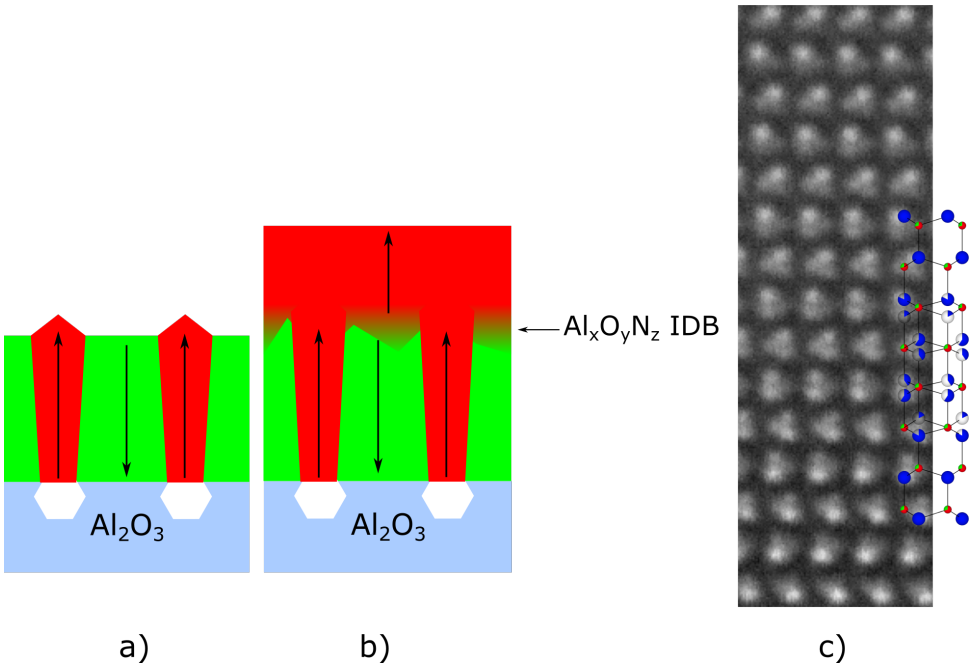

Figure 5.6.: Schematic representation of polarity inversion in a mixed-polar AlN layers induced via oxygen annealing.(Green color and downwards pointing arrow denote N-polarity; Red color and upwards pointing arrow denote metal-polarity.) a) Initial state: AlN layer with dominant N-polarity and Al-polar columnar inversion domains. b) Final state (after annealing in O-rich environment and AlN overgrowth): aluminum-oxynitride inversion domain boundary, formed due to annealing in oxygen, inverts polarity of N-polar domains. AlN layer grown during a second step is Al-polar. c) Comparison of microstructute of zig-zag IDB with $Al_9O_3N_7$ model.

In this chapter we experimentally demonstrated the possibility of controlled polarity inversion in AlN film by introducing oxygen annealing as a mediating step in MOVPE growth of AlN. We started from dominantly N-polar layer with high density of Al-polar columnar inversion domains, applying the growth recipe, described in the previous chapter.(fig. 5.6 (a)) We annealed the mixed-polar AlN film in an oxygen-rich atmosphere outside the MOVPE growth reactor. As oxygen annealing was completed, the sample was transferred back to MOVPE growth reactor where the AlN was regrown at the same deposition conditions.
We have shown that this process results in the formation of a zig-zag shaped inversion domain boundary, that switches the N-polar domains of the AlN film to Al-polar ones. We observed that this IDB inverts the polarity only of the N-polar matrix of initially deposited AlN film. The crystalline structure and polarity of Al-polar domains, which start at the interface with the sapphire substrate, remain unaffected.

Thus the AlN film, deposited after oxygen annealing, turns out to have a dominant Al-polarity as opposed to the mainly N-polar AlN, formed during the first growth step before annealing. (fig. 5.6 (b))
We have investigated the microstructure of the IDB by high-resolution HAADF-STEM. We may notice that the crystal structure of IDB, that mediates the layer polarity from N to Al has similar characteristics as the $Al_9O_3N_7$ that we discussed in the case of self-induced polarity inversion in nitridation layer in chapter 2 (fig. 5.6 (c)): the tetrahedrally-coordinated Al-atoms at the N-polar wurtzite sites are followed by the rhombohedral structure. The exchange in site occupation between N-polar and Al-polar sub-lattices leads to the establishment of Al-polarity. On the HAADF high-resolution image the width of the transition interface appears to consist of 13-14 monolayers instead of 4 monolayers in the model structure of $Al_9O_3N_7$. We assume that this occurs due to the fact that IDB is not planar, as it was observed in chapters 2 and 3, but has a zig-zag three-dimensional shape. Thus the inclined facets of IDB within the depth of the sample may be projected on the image plane, resulting in the increased width of the IDB observed on the image.
The EELS measurements of the area with the zig-zag boundary within AlN film show that oxygen atoms are localized within the IDB between N-polar and Al-polar AlN. That supports our assumption, that the polarity inversion in this experiment is guided by a mechanism similar to the formation of the aluminum-oxynitride R27 phase, as we discussed in chapters 2 and 3.
We have shown that introducing an oxygen annealing step in the growth process leads to incorporation of oxygen atoms on N-polar surfaces and formation of symmetrical rhombohedral $Al_9O_3N_7$ phase, that mediates the layer polarity transition from N-face to Al-face. However we have not observed the opposite polarity transitions – from Al-face to N-face. The possible reason is that oxygen atoms are more favorably adsorbed on N-polar than on Al-polar AlN surfaces. Kirilyuk et. al. have experimentally demonstrated this effect for GaN films. [114] They showed a broad photoluminescence emission in epitaxial layer grown on $[000\bar{1}]$ GaN substrate, indicating the presence of free electrons. The secondary ion-mass spectrometry (SIMS) measurements confirmed that these free electrons originate from oxygen atoms, substituting nitrogen in GaN lattice, and acting as a shallow donor. Takeuchi et.al and Fichtenbaum et. al. also performed SIMS measurements on N- and Al-polar AlN layers showing a higher oxygen concentrations in N-polar layers. [115, 6]
There are certain contradictions in theoretical calculations of oxygen absorption energy as a function of oxygen coverage for $[000\bar{1}]$ and [0001] AlN and GaN surfaces. The general trend shown by Zywietz et. al. for GaN films [116] and later for AlN films by Ye et. al. [117] and Miao et.al. [118], shows that at low oxygen coverage, oxygen atoms, adsorbed in hollow sites in Me-terminated surfaces of both polarities, passivate the metal atom dangling bonds, and the adsorption energies for both $[000\bar{1}]$ and [0001]-polar surfaces are comparably low. With an increased oxygen coverage of the surface, the adsorption energy for [0001]-polar surface is increasing significantly, causing strong repulsive forces between oxygen atoms, while for the $[000\bar{1}]$-polar AlN

and GaN surface the adsorption energy remains low. However, Miao et.al showed that this trend depends strongly on the surface reconstruction and on the oxygen occupation sites. For example, for oxygen occupying nitrogen sites in AlN lattice, there is no significant difference in adsorption energies for $[000\bar{1}]$ and [0001]-polar surfaces even for high oxygen coverage.

Despite of this uncertainty in the theoretical predictions of oxygen adsorption, our observation supports the fact, that during the 30 minutes of annealing in oxygen plasma, more oxygen atoms are trapped at the surface of N-polar matrix regions, than inside Al-polar domains. Oxygen atoms will bind to Al-atoms, forming the symmetrical rhombohedral structure of R27 phase ($Al_9O_3N_7$), described in 2.3.2. We have observed that 30 minutes of annealing in oxygen-rich atmosphere results in only 1.5 full monolayers of oxygen atoms at the interface between N-polar AlN and overgrown Al-polar AlN. Therefore, we can assume that the process of oxygen in-diffusion is self-limited and presumably driven by the effect of charge compensation of the dangling bonds in N-polar surface. Our result is in agreement with the model proposed by Westwood et.al. [119, 120, 121] and investigated by Bruley et.al. [122]. They have claimed that the polarity inversion from N-face on one side of the planar inversion domain boundary to Al-face on the other side of the defect is driven by the charge compensation effect in order to fulfill the Pauling rule. They also demonstrated that the charge compensation is provided by 1.5 monolayers of oxygen which incorporates within the boundary and increases its stability.

The zig-zag shape of the IDB may be explained by the nonuniform adsorption of oxygen atoms into N-polar AlN surface. In our studies the oxidation of AlN was done by ex-situ annealing in oxygen plasma in PAMBE chamber followed by regrowth of AlN by MOVPE. Although the transfer from MOVPE growing chamber to plasma-assisted MBE chamber was done rapidly avoiding the long exposure of the sample to atmosphere, we can not exclude the role of natural oxidation on IDB formation. The combination of two oxidizing processes can cause non-uniformity in adsorption of oxygen atoms in N-polar surfaces. Another reason for the zig-zag shape is related to the morphology of AlN layer after the first deposition step: the surface is not flat with facets at the top of IDBs.

To summarize, we have demonstrated the possibility of controlled inversion of AlN layers from N-polarity to Al-polarity, grown by MOVPE, that was achieved by annealing in oxygen-rich environment. We have resolved and discussed in details the microstructure of the inversion domain boundary and confirmed that the polarity is mediated by aluminum-oxynitride rhombohedral structure that forms due to oxygen incorporation within the surface of N-polar AlN. Our study offers new possibilities of growing hetero-structures where the polarity properties may be controlled by in-situ oxidation on any step of layer deposition, by implementing oxygen gas source in a MOVPE growth system. In-situ AlN oxidation may offer simple and effective method to manipulate the polarity along the growth direction during MOVPE process, thus opening the way to novel heterostructure devices.

Summary and Conclusions

The main focus of this work is understanding the processes that control the polarity of GaN and AlN films grown along *c*-direction on non-polar sapphire substrates by metal-organic vapor phase epitaxy. The layers were investigated at each growth step separately to follow the evolution of films' polarity during the growth process. A variety of experimental techniques are applied to study surface morphology, chemistry and atomic structure of the layers. Aberration-corrected high-resolution TEM is the principal technique used for determination of the layer polarity and the images were taken using the negative C_S imaging method, that allows to distinguish metal, nitrogen and oxygen atomic columns and thus to define the polarity of the layers with atomic resolution. In order to gain additional information about the atomic structure of the layers we used high-angular annular dark field scanning TEM and electron energy-loss spectroscopy techniques. The analysis of our experimental investigations yields the following principal results that concerns (i) mechanism that governs polarity selection during MOVPE growth of III-nitrides films; (ii) relation between initial sapphire surface nitridation and Al-polar inversion domains in N-polar AlN films; (iii) possibility of controlled switching the layers polarity from N to Al by oxygen annealing.

(i) Mechanism that governs polarity selection during MOCVD growth of III-nitrides films We have studied sapphire surfaces annealed in NH_3 ambient in the range of temperatures between 800 °C and 1080 °C. Our experimental results show that nitridation begins at 800 °C as a chemical transformation occurring non-homogeneously across the sapphire surface in the form of separated patches of aluminum-oxynitride crystalline film. At temperatures above 850 °C these patches transform into a continuous relaxed thin aluminum-oxynitride layer, that completely covers the surface of the sapphire substrate. Aluminum-oxynitride has a rhombohedral crystal symmetry and matches with that of the $Al_9O_3N_7$. AlON has a rich phase diagram with various compositions from Al_2O_3, where Al is octaherdally coordinated, to AlN, where Al atom is tetrahedrally coordinated. $Al_9O_3N_7$ contains a planar inversion domain boundary that promotes the inversion from N-polarity at the interface with the sapphire substrate to Al-polarity at topmost monolayers of the nitridation layer. The analysis of AlN and GaN buffer layer deposited at low temperatures (580 – 650 °C) after sapphire nitridation shows that they are metal polar. The aluminum-oxynitride film with planar IDB is still present underneath the buffer layer and all its characteristic features are present. Thick films deposited in a second step above a buffer layer at high temperature (1000 – 1080 °C) exhibit

smooth morphology and pure metal polarity without inversion domains. On the other hand, when the first step of low temperature buffer layer deposition is omitted and a high temperature layer is grown directly on the nitridated sapphire surface, the resulting film has N-polarity and $Al_9O_3N_7$ is not present. In such high temperature growth environment $Al_9O_3N_7$ is unstable and dissociates, resulting in a N-polar monolayer at the interface and the layer deposited on top inherits N-polarity. To summarize, metal polarity is established during annealing of sapphire substrate in NH_3 ambient via formation of a rhombohedral aluminum-oxynitride structure. The buffer layer deposited at low temperature inherits metal polarity due to preservation of the underlying $Al_9O_3N_7$. Dissociation of aluminum-oxynitride, which occurs when it is not protected by LT buffer, leads to films with N-polarity.
Our results explain the mechanism by which polarity is controlled in a MOVPE growth process that have been applied for the growth of group III-nitrides for three decades. Understanding of this mechanism opens up the possibilities for more controlled polarity engineering in nitride films and can as well give a clue to understanding polarity control in other material systems (e.g. oxides).

(ii) Relation between initial sapphire surface nitridation and Al-polar inversion domains in N-polar AlN films Though the mechanism described above explains very well the establishment of metal-polarity during MOVPE growth of III-nitride films, it falls short to explain some peculiarities in growing N-polar films. We show that N-polar layers still contain a high density of Al-polar inversion domains ($\approx 10^{10} cm^{-2}$). Our experimental results suggest that there is a direct connection between pre-treatment of sapphire substrate (nitridation) and formation of Al-polar inversion domains. Nitridation for extended time and at high temperatures ($>$ 1000 °C) leads to transformation of a smooth and continuous aluminum-oxynitride film to a heterogeneous three-dimensional film. In this case one observes that in addition to the two-dimensional $Al_9O_3N_7$ film, three-dimensional AlN islands form. AlN islands are Al-polar directly from the interface and do not contain a planar IDB. The experimental results of in-situ vacuum annealing in TEM showed that the two-dimensional layer rapidly dissociates at annealing temperatures of 850°C, while three-dimensional islands are more stable remaining present up to temperatures of 1000 °C.
Our experimental results show that metal polar domains in the otherwise N-polar films originate from these metal polar AlN islands. While the aluminum-oxynitride layer is unstable under high temperature growth conditions resulting in N-polar films, Al-polar islands are stable and induce Al-polar columnar inversion domains in the N-polar AlN films. Thus for achieving N-polar films free of inversion domains it is important to control the nitridation conditions preventing the formation of such Al-polar islands. Besides this, we suggest that proper adjustment of the growth parameters (reactor pressure, NH3 flux, etc.) is important in order to increase growth rate of AlN and prevent the concomitant effect of extensive nitridation. Slow growth rate essentially extends the effective nitridation time and consequently result

in formation of Al-polar AlN islands. We believe that our findings on the origin of the metal polar inversion domains will allow to develop new growth strategies for achieving inversion domain free N-polar layers, which will consequently lead to devices with improved electrical properties.

(iii) The possibility of controlled switch of layer polarity from N to Al by oxygen annealing Based on the results in the previous chapters we demonstrate controlled inversion of polarity in mixed-polar films by introducing ex-situ oxygen annealing as an intermediate step in MOVPE growth of AlN. The results of EELS analyses show that annealing of mixed-polar films in oxygen-rich atmosphere results in oxygen incorporation into the surfaces of N-polar domains and formation of an inversion domain boundary. Thus N-polar domains switch their polarity and the overgrown AlN film has predominant Al-polarity. The crystal structure of the inversion domain boundary between the N-polar domains of the original film and the Al polar overgrown film is similar to the symmetrical rhombohedral $Al_9O_3N_7$ phase. Therefore, polarity inversion by annealing in oxygen atmosphere follows similar mechanisms as aluminum-oxynitride formation due to nitridation. Our analysis shows that the process of oxygen atom incorporation into N-polar surfaces is self-limited and results in only 1.5 ML of oxygen atoms at the interface between N-polar AlN and overgrown Al-polar AlN after 30 minutes of annealing. We assume that this limitation is due to charge compensation of the dangling bonds in the N-polar surface. At the same time, oxygen annealing does not influence the polarity of Al-polar domains of the original layer since oxygen atoms do not incorporate into surfaces of Al-polar domains.

Our findings offer new possibilities for "playing with polarity" – creating heterostructures where the polarity properties are manipulated by oxidation at any step of the deposition process. This process can also be conducted in-situ, if oxygen gas source is implemented directly in a MOVPE growth reactor. This process may offer a simple and effective method for growing heteroepitaxial structures with abrupt interfaces between layers having opposite polarities.

Acknowledgments

This thesis has been carried out in the Centre de Recherche sur l'Hétéro-Epitaxie et ses Applications (CRHEA) in Valbonne, France and Leibniz-Institute for Crystal Growth (IKZ) in Berlin, Germany. I would like to thank all people from both laboratories, who made this work possible.

I would like to express my deep gratitude to **Philippe Vennéguès** for introducing me into the world of science and his wise, mindful and careful supervision of my work through the whole period of time despite of the long distance between Valbonne and Berlin. I am thankful for his patience and persistence whilst familiarizing me with the techniques of transmission electron microscopy and the art of sample preparation.

I am immensely thankful to **Dr. Martin Albrecht**, who has supervised my work during my stay in Berlin, for countless discussions and valuable advises, for sharing his professional knowledge and experience with me and for being a constantly inspiring example of a scientist.

I am thankful to **Aimeric Courville** from CRHEA for preparing MOVPE samples for my research, for being open to all my ideas and providing the samples in the shortest possible time. I would also like to thank **Olivier Tottereau**, **Virginie Brändli** and **Frédéric Georgi** for their assistance with SEM and XPS measurements.

I express my thanks to **Stefan Mohn** for his priceless contribution for this thesis, that makes the work complete, and numerous discussions on the polarity control issues. I am deeply grateful to **Dr. Toni Markurt** for his assistance with the STEM investigations and data analysis, for the patience with all my questions and concerns, for the encouragement and constructive ideas. I thank **Dr. Tobias Schulz** for reading this manuscript. I would also like to thank the rest of the members of the electron microscopy group at the Leibniz Institute of Crystal Growth for the great working environment.

I acknowledge the funding from the ESTEEM2 project for the opportunity to work with the probe-corrected NION Ultrastem microscope. I would like to thank **Katia March** for the high-quality EELS and HR-STEM measurements, presented in this work.

I am thankful to **Michèle Pefferkorn**, **Isabelle Cerutti** and **Anne-Marie Galiana** from CRHEA, as well as **Birgit Ruthenberg** and **Andrea Lepper** from IKZ for their administrative support and solving my bureaucratic problems, what made my stay in France and Germany trouble-free.

I acknowledge the funding from GANEX (ANR-11- LABX-0014) project for financial

support of my thesis and, personally, **Jean-Yves Duboz** for the unique opportunity to work in a frame of this project.
I am grateful to **Michel Khoury** for being an excellent office-mate and even better friend, for tons of good laughs and cordial talks, and for being my personal professional motivation.
I feel inexpressible gratitude to my parents for their impact in my education and deep faith in me on the road to this degree.
Finally, I am hugely thankful to my partner for empowering me with his support and confidence every day.

Bibliography

[1] S. Mohn, N. Stolyarchuk, T. Markurt, R. Kirste, M. P. Hoffmann, R. Collazo, A. Courville, R. Di Felice, Z. Sitar, P. Vennéguès, and M. Albrecht, "Polarity control in group-III nitrides beyond pragmatism," *Physical Review Applied*, vol. 5, no. 5, 2016.

[2] F. Bernardini, V. Fiorentini, and D. Vanderbilt, "Spontaneous polarization and piezoelectric constants of III-V nitrides," *Phys. Rev. B*, vol. 56, pp. R10024–R10027, 1997.

[3] M. Stutzmann, O. Ambacher, M. Eickhoff, U. Karrer, A. Lima Pimenta, R. Neuberger, J. Schalwig, R. Dimitrov, P. Schuck, and R. Grober, "Playing with polarity," *physica status solidi (b)*, vol. 228, no. 2, pp. 505–512, 2001.

[4] M. Sumiya, K. Yoshimura, K. Ohtsuka, and S. Fuke, "Dependence of impurity incorporation on the polar direction of GaN film growth," *Applied Physics Letters*, vol. 76, no. 15, p. 2098, 2000.

[5] J. Neugebauer, T. K. Zywietz, M. Scheffler, J. E. Northrup, H. Chen, and R. M. Feenstra, "Adatom kinetics on and below the surface: The existence of a new diffusion channel," *Phys. Rev. Lett.*, vol. 90, p. 056101, 2003.

[6] N. Fichtenbaum, T. Mates, S. Keller, S. DenBaars, and U. Mishra, "Impurity incorporation in heteroepitaxial N-face and Ga-face GaN films grown by metalorganic chemical vapor deposition," *Journal of Crystal Growth*, vol. 310, no. 6, pp. 1124 – 1131, 2008.

[7] J. L. Rouviere, M. Arlery, R. Niebuhr, K. H. Bachem, and O. Briot, "Correlation between surface morphologies and crystallographic structures of GaN layers grown by MOCVD on sapphire," *MRS Internet Journal of Nitride Semiconductor Research*, vol. 2, 1996.

[8] H. Kawakami, K. Sakurai, K. Tsubouchi, and N. Mikoshiba, "Epitaxial growth of AlN film with an initial-nitriding layer on $\alpha - Al_2O_3$ substrate," *Japanese Journal of Applied Physics*, vol. 27, no. 2, pp. 161–163, 1988.

[9] H. Amano, N. Sawaki, I. Akasaki, and Y. Toyoda, "Metalorganic vapor phase epitaxial growth of a high quality GaN film using an AlN buffer layer," *Applied Physics Letters*, vol. 48, no. 5, p. 353, 1986.

[10] S. Nakamura, "GaN growth using GaN buffer layer," *Japanese Journal of Applied Physics*, vol. 30, no. 10A, p. L1705, 1991.

[11] O. Ambacher, "Two-dimensional electron gases induced by spontaneous and piezoelectric polarization charges in N- and Ga-face AlGaN/GaN heterostructures," *J. Appl. Phys.*, vol. 85, no. 6, p. 3222, 1999.

[12] S. Rajan, M. Wong, Y. Fu, F. Wu, J. S. Speck, and U. K. Mishra, "Growth and

electrical characterization of N-face AlGaN/GaN heterostructures," *Japanese Journal of Applied Physics*, vol. 44, no. 11L, p. L1478, 2005.

[13] M. H. Wong, S. Keller, S. D. Nidhi, D. J. Denninghoff, S. Kolluri, D. F. Brown, J. Lu, N. A. Fichtenbaum, E. Ahmadi, U. Singisetti, A. Chini, S. Rajan, S. P. DenBaars, J. S. Speck, and U. K. Mishra, "N-polar GaN epitaxy and high electron mobility transistors," *Semiconductor Science and Technology*, vol. 28, no. 7, p. 074009, 2013.

[14] J. Verma, J. Simon, V. Protasenko, T. Kosel, H. G. Xing, and D. Jena, "N-polar III-nitride quantum well light-emitting diodes with polarization-induced doping," *Applied Physics Letters*, vol. 99, no. 17, p. 171104, 2011.

[15] J. Jasinski, Z. Liliental-Weber, Q. S. Paduano, and D. W. Weyburne, "Inversion domains in AlN grown on (0001) sapphire," *Applied Physics Letters*, vol. 83, no. 14, p. 2811, 2003.

[16] R. Miyagawa, S. Yang, H. Miyake, K. Hiramatsu, T. Kuwahara, M. Mitsuhara, and N. Kuwano, "Microstructure of AlN grown on a nucleation layer on a sapphire substrate," *Applied Physics Express*, vol. 5, no. 2, p. 025501, 2012.

[17] V. Kueller, A. Knauer, F. Brunner, A. Mogilatenko, M. Kneissl, and M. Weyers, "Investigation of inversion domain formation in AlN grown on sapphire by MOVPE," *physica status solidi (c)*, vol. 9, no. 3-4, pp. 496–498, 2012.

[18] R. Collazo, S. Mita, A. Aleksov, R. Schlesser, and Z. Sitar, "Growth of Ga- and N- polar gallium nitride layers by metalorganic vapor phase epitaxy on sapphire wafers," *Journal of Crystal Growth*, vol. 287, no. 2, pp. 586–590, 2006.

[19] S. Mita, R. Collazo, and Z. Sitar, "Fabrication of a GaN lateral polarity junction by metalorganic chemical vapor deposition," *Journal of Crystal Growth*, vol. 311, no. 10, pp. 3044 – 3048, 2009.

[20] A. Chowdhury, H. M. Ng, M. Bhardwaj, and N. G. Weimann, "Second-harmonic generation in periodically poled GaN," *Applied Physics Letters*, vol. 83, no. 6, pp. 1077–1079, 2003.

[21] R. Dimitrov, M. Murphy, J. Smart, W. Schaff, J. R. Shealy, L. F. Eastman, O. Ambacher, and M. Stutzmann, "Two-dimensional electron gases in Ga-face and N-face AlGaN/GaN heterostructures grown by plasma-induced molecular beam epitaxy and metalorganic chemical vapor deposition on sapphire," *Journal of Applied Physics*, vol. 87, no. 7, pp. 3375–3380, 2000.

[22] A. Aleksov, R. Collazo, S. Mita, R. Schlesser, and Z. Sitar, "Current-voltage characteristics of n/n lateral polarity junctions in GaN," *Applied Physics Letters*, vol. 89, no. 5, p. 052117, 2006.

[23] H. P. Maruska and J. J. Tietjen, "The preparation and properties of vapor-deposited single-crystalline GaN," *Applied Physics Letters*, vol. 15, no. 10, pp. 327–329, 1969.

[24] W. M. Yim, E. J. Stofko, P. J. Zanzucchi, J. I. Pankove, M. Ettenberg, and S. L. Gilbert, "Epitaxially grown AlN and its optical band gap," *Journal of Applied Physics*, vol. 44, no. 1, pp. 292–296, 1973.

[25] H. Schulz and K. Thiemann, "Crystal structure refinement of AlN and GaN," *Solid State Communications*, vol. 23, no. 11, pp. 815 – 819, 1977.

[26] B. B. Kosicki and D. Kahng, "Preparation and structural properties of GaN thin films," *Journal of Vacuum Science and Technology*, vol. 6, no. 4, pp. 593–596, 1969.

[27] H. M. Manasevit, F. M. Erdmann, and W. I. Simpson, "The use of metalorganics in the preparation of semiconductor materials: IV. The nitrides of aluminum and gallium," *Journal of The Electrochemical Society*, vol. 118, no. 11, pp. 1864–1868, 1971.

[28] D. B. Williams and C. B. Carter, *Transmission electron microscopy: a textbook for materials science*. New York: Springer US, 2nd ed., 2008.

[29] B. Fultz and J. Howe, *Transmission Electron Microscopy and Diffractometry of Materials*. Springer, 3rd ed., 2009.

[30] S. J. Pennycook and P. D. Nellist, eds., *Scanning Transmission Electron Microscopy*. New York: Springer, 2011.

[31] R. Brydson, ed., *Aberration-Corrected Analytical Tranmission Electron Microscopy*. JOHN WILEY & SONS INC, 1st ed., 2011.

[32] R. Egerton, *Electron Energy-Loss Spectroscopy in the Electron Microscope*. Springer US, 2011.

[33] H. Bethge, *Electron Microscopy in Solid State Physics (Materials Science Monographs)*. Elsevier Science Ltd, 1987.

[34] H. Lichte, "Optimum focus for taking electron holograms," *Ultramicroscopy*, vol. 38, no. 1, pp. 13 – 22, 1991.

[35] H. Rose, "Correction of aberrations, a promising means for improving the spatial and energy resolution of energy-filtering electron microscopes," *Ultramicroscopy*, vol. 56, no. 1, pp. 11 – 25, 1994.

[36] S. Uhlemann and M. Haider, "Residual wave aberrations in the first spherical aberration corrected transmission electron microscope," *Ultramicroscopy*, vol. 72, no. 3, pp. 109–119, 1998.

[37] M. Lentzen, B. Jahnen, C. L. Jia, A. Thust, K. Tillmann, and K. Urban, "High-resolution imaging with an aberration-corrected transmission electron microscope," *Ultramicroscopy*, vol. 92, no. 3, pp. 233–242, 2002.

[38] C.-L. Jia, M. Lentzen, and K. Urban, "High-resolution transmission electron microscopy using negative spherical aberration," *Microscopy and Microanalysis*, vol. 10, no. 2, p. 174–184, 2004.

[39] C. L. Jia, L. Houben, A. Thust, and J. Barthel, "On the benefit of the negative-spherical-aberration imaging technique for quantitative HRTEM," *Ultramicroscopy*, vol. 110, no. 5, pp. 500–505, 2010.

[40] R. Serneels, M. Snykers, P. Delavignette, R. Gevers, and S. Amelinckx, "Friedel's law in electron diffraction," *Physica Status Solidi (b)*, vol. 58, no. 1, pp. 277–292, 1973.

[41] L. T. Romano, J. E. Northrup, and M. A. O'Keefe, "Inversion domains in GaN grown on sapphire," *Applied Physics Letters*, vol. 69, no. 16, pp. 2394–2396,

1996.

[42] A. Howie, "Image contrast and localized signal selection techniques," *Journal of Microscopy*, vol. 117, no. 1, pp. 11–23, 1979.

[43] C. R. Hall and P. B. Hirsch, "Effect of thermal diffuse scattering on propagation of high energy electrons through crystals," *Proceedings of the Royal Society of London A: Mathematical, Physical and Engineering Sciences*, vol. 286, no. 1405, pp. 158–177, 1965.

[44] L.-M. Peng, "Electron atomic scattering factors and scattering potentials of crystals," *Micron*, vol. 30, no. 6, pp. 625 – 648, 1999.

[45] E. J. Kirkland, *Advanced Computing in Electron Microscopy*. Springer US, 2010.

[46] J. M. LeBeau and S. Stemmer, "Experimental quantification of annular dark-field images in scanning transmission electron microscopy," *Ultramicroscopy*, vol. 108, no. 12, pp. 1653 – 1658, 2008.

[47] O. Krivanek, N. Dellby, and A. Lupini, "Towards sub-Å electron beams," *Ultramicroscopy*, vol. 78, no. 1, pp. 1 – 11, 1999.

[48] O. Krivanek, P. Nellist, N. Dellby, M. Murfitt, and Z. Szilagyi, "Towards sub-0.5Å electron beams," *Ultramicroscopy*, vol. 96, no. 3, pp. 229 – 237, 2003. Proceedings of the International Workshop on Strategies and Advances in Atomic Level Spectroscopy and Analysis.

[49] N. Dellby, N. Bacon, P. Hrncirik, M. Murfitt, G. Skone, Z. Szilagyi, and O. Krivanek, "Dedicated STEM for 200 to 40 keV operation," *The European Physical Journal - Applied Physics*, vol. 54, no. 3, 2011.

[50] R. F. Egerton, "Electron energy-loss spectroscopy in the TEM," *Reports on Progress in Physics*, vol. 72, no. 1, p. 016502, 2008.

[51] J. M. Cowley and A. F. Moodie, "The scattering of electrons by atoms and crystals. I. A new theoretical approach," *Acta Crystallographica*, vol. 10, no. 10, pp. 609–619, 1957.

[52] P. Stadelmann, "EMS - a software package for electron diffraction analysis and HREM image simulation in materials science," *Ultramicroscopy*, vol. 21, no. 2, pp. 131 – 145, 1987.

[53] J.-L. Rouviere, C. Bougerol, B. Amstatt, E. Bellet-Almaric, and B. Daudin, "Measuring local lattice polarity in AlN and GaN by high resolution z-contrast imaging: The case of (0001) and (1100) GaN quantum dots," *Applied Physics Letters*, vol. 92, no. 20, p. 201904, 2008.

[54] G. B. Stringfellow, *Organometallic Vapor-Phase Epitaxy*. Elsevier Science, 2012.

[55] T. Kuech, *Handbook of Crystal Growth*. Elsevier Science & Technology, 2014.

[56] D. W. Shaw, "Kinetic aspects in the vapour phase epitaxy of III–V compounds," *Journal of Crystal Growth*, vol. 31, pp. 130 – 141, 1975.

[57] E. Bauer and J. H. van der Merwe, "Structure and growth of crystalline superlattices: From monolayer to superlattice," *Phys. Rev. B*, vol. 33, pp. 3657–3671, 1986.

[58] B. Beaumont and P. J. L. Gibart, "Metal organic vapor phase epitaxy of GaN and lateral overgrowth," *Proc. SPIE 3725, International Conference on Solid State Crystals '98: Epilayers and Heterostructures in Optoelectronics and Semiconductor Technology, 2*, vol. 3725, pp. 2–13, 1999.

[59] A. Koukitu, N. Takahashi, and H. Seki, "Thermodynamic study on metalorganic vapor-phase epitaxial growth of group III nitrides," *Japanese Journal of Applied Physics*, vol. 36, no. 9A, p. L1136, 1997.

[60] V. S. Ban, "Mass spectrometric studies of vapor-phase crystal growth," *Journal of The Electrochemical Society*, vol. 119, no. 6, p. 761, 1972.

[61] D. D. Koleske, A. E. Wickenden, R. L. Henry, M. E. Twigg, J. C. Culbertson, and R. J. Gorman, "Enhanced GaN decomposition in H_2 near atmospheric pressures," *Applied Physics Letters*, vol. 73, no. 14, pp. 2018–2020, 1998.

[62] Digital Insturments, Veeco Metrology Group 2000, *Scanning Probe Microscopy Training Notebook*, 2000.

[63] I. Horcas, R. Fernández, J. M. Gómez-Rodríguez, J. Colchero, J. Gómez-Herrero, and A. M. Baro, "WSXM: A software for scanning probe microscopy and a tool for nanotechnology," *Review of Scientific Instruments*, vol. 78, no. 1, p. 013705, 2007.

[64] C. Powell and P. Larson, "Quantitative surface analysis by x-ray photoelectron spectroscopy," *Applications of Surface Science*, vol. 1, no. 2, pp. 186 – 201, 1978.

[65] C. D. Wagner, L. E. Davis, M. V. Zeller, J. A. Taylor, R. H. Raymond, and L. H. Gale, "Empirical atomic sensitivity factors for quantitative analysis by electron spectroscopy for chemical analysis," *Surface and Interface Analysis*, vol. 3, no. 5, pp. 211–225, 1981.

[66] S. Keller, B. P. Keller, Y.-F. Wu, B. Heying, D. Kapolnek, J. S. Speck, U. K. Mishra, and S. P. DenBaars, "Influence of sapphire nitridation on properties of gallium nitride grown by metalorganic chemical vapor deposition," *Applied Physics Letters*, vol. 68, no. 11, p. 1525, 1996.

[67] N. Grandjean, J. Massies, and M. Leroux, "Nitridation of sapphire. Effect on the optical properties of GaN epitaxial overlayers," *Applied Physics Letters*, vol. 69, no. 14, p. 2071, 1996.

[68] A. Yamamoto, M. Tsujino, M. Ohkubo, and A. Hashimoto, "Nitridation effects of substrate surface on the metalorganic chemical vapor deposition growth of InN on si and $\alpha - Al_2O_3$ substrates," *Journal of Crystal Growth*, vol. 137, no. 3-4, pp. 415–420, 1994.

[69] K. Uchida, A. Watanabe, F. Yano, M. Kouguchi, T. Tanaka, and S. Minagawa, "Nitridation process of sapphire substrate surface and its effect on the growth of GaN," *Journal of Applied Physics*, vol. 79, no. 7, p. 3487, 1996.

[70] S. Fuke, H. Teshigawara, K. Kuwahara, Y. Takano, T. Ito, M. Yanagihara, and K. Ohtsuka, "Influences of initial nitridation and buffer layer deposition on the morphology of a (0001) GaN layer grown on sapphire substrates," *Journal of Applied Physics*, vol. 83, no. 2, p. 764, 1998.

[71] F. Dwikusuma and T. F. Kuech, "X-ray photoelectron spectroscopic study on sapphire nitridation for GaN growth by hydride vapor phase epitaxy: Nitridation mechanism," *Journal of Applied Physics*, vol. 94, no. 9, p. 5656, 2003.

[72] K. Akiyama, Y. Ishii, H. Murakami, Y. Kumagai, and A. Koukitu, "In situ gravimetric monitoring of surface reactions between sapphire and NH_3," *Journal of Crystal Growth*, vol. 311, no. 10, pp. 3110–3113, 2009.

[73] C. Heinlein, J. Grepstad, T. Berge, and H. Riechert, "Preconditioning of c-plane sapphire for GaN epitaxy by radio frequency plasma nitridation," *Applied Physics Letters*, vol. 71, no. 3, pp. 341–343, 1997.

[74] C. Heinlein, J. K. Grepstad, S. Einfeldt, D. Hommel, T. Berge, and A. P. Grande, "Preconditioning of c-plane sapphire for GaN molecular beam epitaxy by electron cyclotron resonance plasma nitridation," *Journal of Applied Physics*, vol. 83, no. 11, pp. 6023–6027, 1998.

[75] T. Akiyama, Y. Saito, K. Nakamura, and T. Ito, "Nitridation of Al_2O_3 surfaces: Chemical and structural change triggered by oxygen desorption," *Physical Review Letters*, vol. 110, no. 2, 2013.

[76] Y. Saito, T. Akiyama, K. Nakamura, and T. Ito, "Ab initio-based approach to elemental nitridation process of $\alpha - Al_2O_3$," *Journal of Crystal Growth*, vol. 362, pp. 29–32, 2013.

[77] T. Hashimoto, "Structural investigation of sapphire surface after nitridation," *Journal of Crystal Growth*, vol. 189/190, pp. 254–258, 1998.

[78] Y. Cho, Y. Kim, E. R. Weber, S. Ruvimov, and Z. Liliental-Weber, "Chemical and structural transformation of sapphire Al_2O_3 surface by plasma source nitridation," *Journal of Applied Physics*, vol. 85, no. 11, p. 7909, 1999.

[79] D. Skuridina, D. V. Dinh, M. Pristovsek, B. Lacroix, M.-P. Chauvat, P. Ruterana, M. Kneissl, and P. Vogt, "Surface and crystal structure of nitridated sapphire substrates and their effect on polar InN layers," *Applied Surface Science*, vol. 307, pp. 461–467, 2014.

[80] M. Losurdo, P. Capezzuto, and G. Bruno, "Plasma cleaning and nitridation of sapphire ($\alpha - Al_2O_3$) surfaces: New evidence from in situ real time ellipsometry," *Journal of Applied Physics*, vol. 88, no. 4, p. 2138, 2000.

[81] G. Namkoong, W. A. Doolittle, A. S. Brown, M. Losurdo, P. Capezzuto, and G. Bruno, "Role of sapphire nitridation temperature on GaN growth by plasma assisted molecular beam epitaxy: Part I. Impact of the nitridation chemistry on material characteristics," *Journal of Applied Physics*, vol. 91, no. 4, p. 2499, 2002.

[82] Y. Wang, X. L. Du, Z. X. Mei, Z. Q. Zeng, M. J. Ying, H. T. Yuan, J. F. Jia, Q. K. Xue, and Z. Zhang, "Cubic nitridation layers on sapphire substrate and their role in polarity selection of ZnO films," *Applied Physics Letters*, vol. 87, no. 5, p. 051901, 2005.

[83] P. Vennéguès and B. Beaumont, "Transmission electron microscopy study of the nitridation of the (0001) sapphire surface," *Applied Physics Letters*, vol. 75, no. 26, p. 4115, 1999.

[84] M. Seelmann-Eggebert, H. Zimmermann, H. Obloh, R. Niebuhr, and B. Wachtendorf, "Plasma cleaning and nitridation of sapphire substrates for $Al_xGa_{1-x}N$ epitaxy as studied by x-ray photoelectron diffraction," *Journal of Vacuum Science & Technology A: Vacuum, Surfaces, and Films*, vol. 16, no. 4, pp. 2008–2015, 1998.

[85] F. Widmann, G. Feuillet, B. Daudin, and J. L. Rouvière, "Low temperature sapphire nitridation: A clue to optimize GaN layers grown by molecular beam epitaxy," *Journal of Applied Physics*, vol. 85, no. 3, pp. 1550–1555, 1999.

[86] S. Sonoda, S. Shimizu, X.-Q. Shen, S. Hara, and H. Okumura, "Characterization of polarity of wurtzite GaN film grown by molecular beam epitaxy using NH_3," *Japanese Journal of Applied Physics*, vol. 39, no. 3A, p. L202, 2000.

[87] S. Mikroulis, A. Georgakilas, A. Kostopoulos, V. Cimalla, E. Dimakis, and P. Komninou, "Control of the polarity of molecular-beam-epitaxy-grown GaN thin films by the surface nitridation of Al_2O_3 (0001) substrates," *Applied Physics Letters*, vol. 80, no. 16, pp. 2886–2888, 2002.

[88] Q. S. Paduano, D. W. Weyburne, J. Jasinski, and Z. Liliental-Weber, "Effect of initial process conditions on the structural properties of AlN films," *Journal of Crystal Growth*, vol. 261, no. 2-3, pp. 259–265, 2004.

[89] Y. Wu, A. Hanlon, J. F. Kaeding, R. Sharma, P. T. Fini, S. Nakamura, and J. S. Speck, "Effect of nitridation on polarity, microstructure, and morphology of AlN films," *Applied Physics Letters*, vol. 84, no. 6, pp. 912–914, 2004.

[90] K. Kachel, D. Siche, S. Golka, P. Sennikov, and M. Bickermann, "FTIR exhaust gas analysis of GaN pseudo-halide vapor phase growth," *Materials Chemistry and Physics*, vol. 177, pp. 12–18, 2016.

[91] M. A. Moram, C. S. Ghedia, D. V. S. Rao, J. S. Barnard, Y. Zhang, M. J. Kappers, and C. J. Humphreys, "On the origin of threading dislocations in GaN films," *Journal of Applied Physics*, vol. 106, no. 7, p. 073513, 2009.

[92] J. W. McCauley and N. D. Corbin, "High temperature reactions and microstructures in the Al_2O_3-AlN system," in *Progress in Nitrogen Ceramics* (F. L. Riley, ed.), pp. 111–118, Dordrecht: Springer Nature, 1983.

[93] N. D. Corbin, "Aluminum oxynitride spinel: A review," *Journal of the European Ceramic Society*, vol. 5, no. 3, pp. 143–154, 1989.

[94] P. Goursat, M. Billy, P. Goeuriot, J. Labbe, J. Villechenoux, G. Roult, and J. Bardolle, "Contribution a l'etude du systeme AL/O/N II: Retention d'azote dans les produits d'oxydation de l'oxynitrure d'aluminium γ," *Materials Chemistry*, vol. 6, no. 2, pp. 81–93, 1981.

[95] P. Tabary and C. Servant, "Crystalline and microstructure study of the AlN-Al_2O_3 section in the Al-NO system. I. Polytypes and-AlON spinel phase," *Journal of applied crystallography*, vol. 32, no. 2, pp. 241–252, 1999.

[96] J. W. McCauley, "A simple model for aluminum oxynitride spinels," *Journal of the American Ceramic Society*, vol. 61, no. 7-8, pp. 372–373, 1978.

[97] T. Asaka, H. Banno, S. Funahashi, N. Hirosaki, and K. Fukuda, "Electron density distribution and crystal structure of 27R-AlON, $Al_9O_3N_7$," *Journal of*

Solid State Chemistry, vol. 204, pp. 21–26, 2013.

[98] T. Asaka, T. Kudo, H. Banno, S. Funahashi, N. Hirosaki, and K. Fukuda, "Electron density distribution and crystal structure of 21R-AlON, $Al_7O_3N_5$," *Powder Diffraction*, vol. 28, no. 03, pp. 171–177, 2013.

[99] R. Di Felice and J. E. Northrup, "Energetics of AlN thin films on the Al_2O_3(0001) surface," *Applied Physics Letters*, vol. 73, no. 7, p. 936, 1998.

[100] T. Ito, M. Sumiya, Y. Takano, K. Ohtsuka, and S. Fuke, "Influence of thermal annealing on GaN buffer layers and the property of subsequent GaN layers grown by metalorganic chemical vapor deposition," *Japanese journal of applied physics*, vol. 38, no. 2R, p. 649, 1999.

[101] M. Sumiya, N. Ogusu, Y. Yotsuda, M. Itoh, S. Fuke, T. Nakamura, S. Mochizuki, T. Sano, S. Kamiyama, H. Amano, and I. Akasaki, "Systematic analysis and control of low-temperature GaN buffer layers on sapphire substrates," *Journal of Applied Physics*, vol. 93, no. 2, p. 1311, 2003.

[102] M. Sumiya, K. Yoshimura, N. Ogusu, S. Fuke, K. Mizuno, M. Yoshimoto, H. Koinuma, and L. T. Romano, "Effect of buffer-layer engineering on the polarity of GaN films," *Journal of Vacuum Science & Technology A: Vacuum, Surfaces, and Films*, vol. 20, no. 2, pp. 456–458, 2002.

[103] P. Vennéguès, B. Beaumont, S. Haffouz, M. Vaille, and P. Gibart, "Influence of in situ sapphire surface preparation and carrier gas on the growth mode of GaN in MOVPE," *Journal of crystal growth*, vol. 187, no. 2, pp. 167–177, 1998.

[104] M. Funato, M. Shibaoka, and Y. Kawakami, "Heteroepitaxy mechanisms of AlN on nitridated c- and a-plane sapphire substrates," *Journal of Applied Physics*, vol. 121, no. 8, p. 085304, 2017.

[105] M. Imura, K. Nakano, N. Fujimoto, N. Okada, K. Balakrishnan, M. Iwaya, S. Kamiyama, H. Amano, I. Akasaki, T. Noro, T. Takagi, and A. Bandoh, "High-temperature metal-organic vapor phase epitaxial growth of AlN on sapphire by multi transition growth mode method varying V/III ratio," *Japanese Journal of Applied Physics*, vol. 45, no. 11R, p. 8639, 2006.

[106] Y. Ohba and R. Sato, "Growth of AlN on sapphire substrates by using a thin AlN buffer layer grown two-dimensionally," *Journal of Crystal Growth*, vol. 221, no. 1-4, pp. 258–261, 2000.

[107] S. Keller, N. A. Fichtenbaum, F. Wu, D. Brown, A. Rosales, S. P. DenBaars, J. S. Speck, and U. K. Mishra, "Influence of the substrate misorientation on the properties of N-polar GaN films grown by metal organic chemical vapor deposition," *Journal of Applied Physics*, vol. 102, no. 8, p. 083546, 2007.

[108] Y. Ohba and A. Hatano, "Growth of high-quality AlN and AlN/GaN/AlN heterostructure on sapphire substrate," *Japanese Journal of Applied Physics*, vol. 35, no. 8B, p. L1013, 1996.

[109] C. H. Chen, H. Liu, D. Steigerwald, W. Imler, C. P. Kuo, M. G. Craford, M. Ludowise, S. Lester, and J. Amano, "A study of parasitic reactions between NH_3 and TMGa or TMAl," *Journal of Electronic Materials*, vol. 25, no. 6,

pp. 1004–1008, 1996.

[110] A. V. Lobanova, K. M. Mazaev, R. A. Talalaev, M. Leys, S. Boeykens, K. Cheng, and S. Degroote, "Effect of V/III ratio in AlN and AlGaN MOVPE," *Journal of Crystal Growth*, vol. 287, no. 2, pp. 601–604, 2006.

[111] D. Zhao, J. Zhu, D. Jiang, H. Yang, J. Liang, X. Li, and H. Gong, "Parasitic reaction and its effect on the growth rate of AlN by metalorganic chemical vapor deposition," *Journal of Crystal Growth*, vol. 289, no. 1, pp. 72–75, 2006.

[112] M. Adachi, M. Takasugi, D. Morikawa, K. Tsuda, A. Tanaka, and H. Fukuyama, "Analysis of the dislocation and polarity in an AlN layer grown using Ga-Al flux," *Applied Physics Express*, vol. 5, no. 10, p. 101001, 2012.

[113] M. H. Wong, F. Wu, J. S. Speck, and U. K. Mishra, "Polarity inversion of N-face GaN using an aluminum oxide interlayer," *Journal of Applied Physics*, vol. 108, no. 12, p. 123710, 2010.

[114] V. Kirilyuk, M. Zielinski, P. Christianen, A. Zauner, J. Weyhera, P. Hageman, and P. Larsen, "Shallow-impurity-related photoluminescence in homoepitaxial GaN," *MRS Proceedings*, vol. 639, 2000.

[115] M. Takeuchi, H. Shimizu, R. Kajitani, K. Kawasaki, Y. Kumagai, A. Koukitu, and Y. Aoyagi, "Improvement of crystalline quality of N-polar AlN layers on c-plane sapphire by low-pressure flow-modulated MOCVD," *Journal of Crystal Growth*, vol. 298, pp. 336–340, 2007.

[116] T. K. Zywietz, J. Neugebauer, and M. Scheffler, "The adsorption of oxygen at GaN surfaces," *Applied Physics Letters*, vol. 74, no. 12, pp. 1695–1697, 1999.

[117] H. Ye, G. Chen, Y. Zhu, and S.-H. Wei, "Asymmetry of adsorption of oxygen at wurtzite AlN (0001) and ($000\bar{1}$) surfaces: First-principles calculations," *Physical Review B*, vol. 77, no. 3, 2008.

[118] M. S. Miao, P. G. Moses, J. R. Weber, A. Janotti, and C. G. V. de Walle, "Effects of surface reconstructions on oxygen adsorption at AlN polar surfaces," *EPL (Europhysics Letters)*, vol. 89, no. 5, p. 56004, 2010.

[119] A. D. Westwood, R. A. Youngman, M. R. McCartney, A. N. Cormack, and M. R. Notis, "Oxygen incorporation in aluminum nitride via extended defects: Part I. Refinement of the structural model for the planar inversion domain boundary," *Journal of materials research*, vol. 10, no. 05, pp. 1270–1286, 1995.

[120] A. D. Westwoord, R. A. Youngman, M. R. McCartney, A. N. Cormack, and M. R. Notis, "Oxygen incorporation in aluminum nitride via extended defects: Part III. Reevaluation of the polytypoid structure in the aluminum nitride-aluminum oxide binary system," *Journal of Materials Research*, vol. 10, no. 10, pp. 2573–2585, 1995.

[121] A. D. Westwood, R. A. Youngman, M. R. McCartney, A. N. Cormack, and M. R. Notis, "Oxygen incorporation in aluminum nitride via extended defects: Part II. Structure of curved inversion domain boundaries and defect formation," *Journal of Materials Research*, vol. 10, no. 5, pp. 1287–1300, 1995.

[122] J. Bruley, A. Westwood, R. A. Youngman, J.-C. Zhao, and M. Notis, "Sreels analysis of oxygen-rich inversion domain boundaries in aluminum nitride,"

MRS Proceedings, vol. 357, 1994.

A. Analysis of EELS experimental data

A.1. The relation between intensities and elemental concentrations of oxygen and nitrogen in EELS measurements

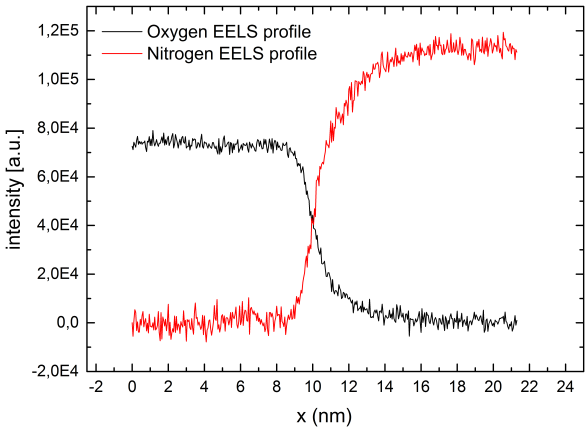

Figure A.1.: a) O K-edge (black line) and N K-edge (red line) EELS intensity profiles across Al_2O_3/AlN interface.

According to 1.30, knowing the experimental intensity ratios of two extracted core-loss signals, we may obtain the elemental ratio of two elements by using the equation:

$$\frac{C^O}{C^N} = \frac{I_c^O}{I_c^N} \times \frac{\sigma_c^N(\beta,\Delta)}{\sigma_c^O(\beta,\Delta)}, \tag{A.1}$$

where C – volume density of atoms for elements O and N; $I_C(\beta,\Delta)$ – the intensity of the core-loss signals collected within the semi-angle β and integrated over an energy range of Δ; $\sigma_c(\beta,\Delta)$ – is a partial cross-section of elements O and N, calculated for core-loss scattering up to an angle β and energy above the edge onset of Δ. Let us assign the cross-section ratio $\frac{\sigma_c^N(\beta,\Delta)}{\sigma_c^O(\beta,\Delta)}$ as k-factor for convenience. Then, the k-factor may be deduced from the eq.A.1:

$$k = \frac{C^O}{C^N} \times \frac{I_c^N}{I_c^O} \tag{A.2}$$

We have calculated the integrated intensities ratio for the O K-edge signal in Al_2O_3 and N K-edge signal in AlN from the EELS-spectra of the Al-polar AlN film on Al_2O_3 substrate.The resulting line-profiles of the integrated signal across the Al_2O_3/AlN interface is shown on fig. A.1. The integrated signal ratio is:

$$\frac{I_c^{N/\mathrm{AlN}}}{I_c^{O/\mathrm{Al_2O_3}}} = \frac{112093}{73540} = 1.52$$

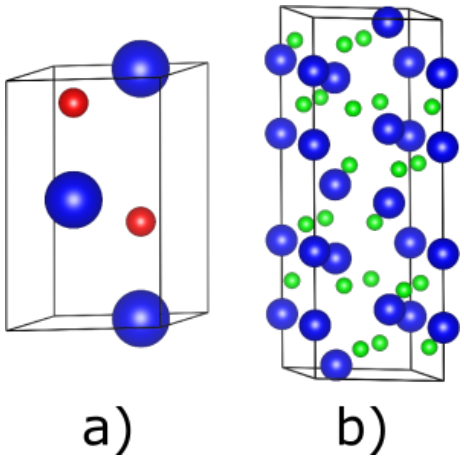

Figure A.2.: Unit cells of AlN (a) and Al_2O_3 (b). (Blue balls represent Al atoms, red – N, green – O atoms).

In order to calculate the volume density of atoms, we have counted the number of atoms in the unit cell and divided this by the volume of the unit cell. The volume of the unit cell is:

$$V_{\mathrm{AlN}} = a \cdot \sin 60° \cdot a \cdot c = \sin 60° \cdot (0.3112nm)^2 \cdot 0.4982nm = 4.178 \cdot 10^{-23} cm^3$$

For wurtzite AlN there are 2 Al and 2 N atoms per unit cell (fig.A.2 (a)). Then the volume density of N atoms within a unit cell is:

$$C_N^{\mathrm{AlN}} = \frac{2}{4.178 \cdot 10^{-23} cm^3} = 4.79 \cdot 10^{22} \frac{N\ atoms}{cm^3}$$

In the unit cell of sapphire there are 12 Al atoms and 18 oxygen atoms.(fig. A.2 (b)) The volume of the unit cell is:

$$V_{\mathrm{Al_2O_3}} = a \cdot \sin 60° \cdot a \cdot c = \sin 60° \cdot (0.47606nm)^2 \cdot 1.2994nm = 2.55 \cdot 10^{-22} cm^3$$

There 18 oxygen atoms per unit cell. The volume density of oxygen atoms within the sapphire unit cell is:

$$C_O^{Al_2O_3} = \frac{18}{2.55 \cdot 10^{-22} cm^3} = 7.06 \cdot 10^{22} \frac{O\, atoms}{cm^3}$$

Applying the equation A.2 we find k :

$$k = \frac{7.06 \cdot 10^{22}}{4.79 \cdot 10^{22}} \times 1.52 = 2.24$$

Since k-factor is a parameter dependent on the element, collection semi-angle β and the energy integration window Δ, we may apply the deduced k-value for analyzing the composition ratio between O and N signals in the case when the used experimental conditions are matching.

A.2. Extraction of effective oxygen profile from the raw EELS profile of Al_2O_3/AlN interface

The recorded oxygen signal can be described as a convolution of the effective oxygen distribution function ($F_0(x)$) and the measurement broadening characterized by Gaussian function ($G(x)$).

$$Signal\, O(x) = G(x) * F_0(x) \tag{A.3}$$

We can describe the $F_0(x)$ function of the effective oxygen distribution following the next assumptions.

- The intensity of the signal is proportional to its concentration.
- Oxygen concentration is constant in Al_2O_3. Therefore the intensity in the left side of the profile is constant (A_0) for $0 < x < x_{IF}$, where x_{IF} – position of the interface.
- Above the interface ($x > x_{IF}$) oxygen concentration is decreasing according to the diffusion law. The simple case solution for the Fick's law of diffusion in one dimension is

  $$n = n_o(1 - erf(\frac{x - x_0}{2\sqrt{Dt}})),$$

  where $2\sqrt{Dt}$ – diffusion length. In the following explanations we will assign the diffusion length as w_{IF} and will name it as "interface width".

$$F_0(x) = \begin{cases} A_0, & 0 < x < x_{IF} \\ (A_0 + dA) \cdot \left[1 - erf(\frac{x - x_{IF}}{w_{IF}})\right], & x > x_{IF} \end{cases}, \tag{A.4}$$

where dA – is the difference in oxygen intensity (i.e. concentration) in sapphire far from the interface and at the interface.
We applied the fitting procedure for the measured oxygen signal by the function resulted from the convolution and found the fitting parameters for the function $F_0(x)$ and extracted the original profile. The main parameters are $A_0 + dA$ and w_{IF} which we can use to characterize and compare the analyzed interfaces.

B. Simulated HAADF-STEM intensities for AlN, GaN and Al_2O_3

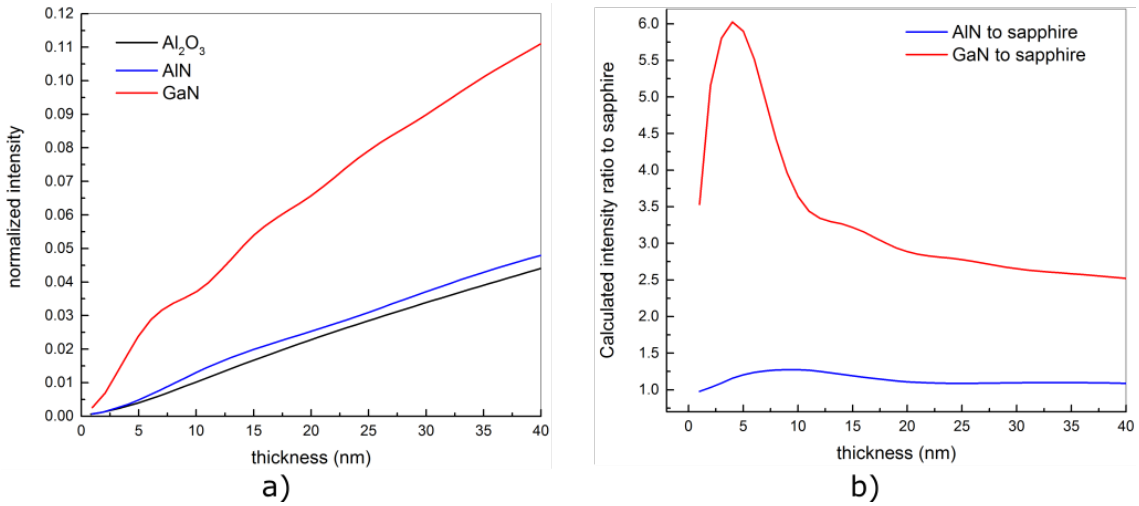

Figure B.1.: Frozen phonon simulations of GaN, AlN andAl_2O_3. a) Simulated normalized HAADF-intensities for AlN, GaN and Al_2O_3 versus thickness; b) HAADF-intensities of GaN and AlN relative to normalized HAADF-intensity of Al_2O_3 as a function of thickness.

Fig. B.1 (a) shows normalized HAADF-STEM intensities for GaN and AlN along the $[11\bar{2}0]$ projection and Al_2O_3 along the $[10\bar{1}0]$ projection as a function of thickness simulated using the frozen phonon approach. Simulated intensities were used for comparison with experimentally obtained values of $I_{normalized}$, calculated using the eq.1.27. Fig. B.1 (b) shows simulated intensities of AlN and GaN normalized to intensity of sapphire.

Publications

Peer-review

1. S. Mohn, N. Stolyarchuk, T. Markurt, R. Kirste, M. P. Hoffmann, R. Collazo, A. Courville, R. Di Felice, Z. Sitar, P. Vennéguès, and M. Albrecht, "Polarity control in group-III nitrides beyond pragmatism," *Physical Review Applied*, vol. 5, no. 5, 2016.
2. N. Stolyarchuk, T. Markurt, A. Courville, K. March, O. Tottereau, P. Vennéguès, and M. Albrecht., "Impact of sapphire nitridation on formation of Al-polar inversion domains in N-polar AlN epitaxial layers," *Journal of Applied Physics*, vol. 122, no. 15, p. 155303, 2017.

Conference contributions

1. Contributed talk: N. Stolyarchuk, A. Courville, S. Mohn, R. Di Felice, J. Northrup , P. Vennéguès and M. Albrecht, "Transmission electron microscopy investigations of nucleation of AlN layers on Al_2O_3 substrates", Microscopy of Semiconducting Materials XIX, Cambridge, UK, 2015.
2. Contributed talk: N. Stolyarchuk, A. Courville, S. Mohn, R. Di Felice, J. Northrup , P. Vennéguès and M. Albrecht, "Transmission electron microscopy investigations of III-Nitride/Sapphire Interfaces at the atomic scale ", Le XIVe colloque de la Société Française des Microscopies, Nice, France, 2015.
3. Contributed talk: N. Stolyarchuk, S. Mohn, T. Markurt, R. Kirste, M. P. Hoffmann, R. Collazo, A. Courville, R. Di Felice, Z. Sitar, , P. Vennéguès and M. Albrecht, "Mechanisms of Polarity Inversion during the MOVPE Growth of III-Nitrides on Sapphire Investigated by Transmission Electron Microscopy ", 18th International Conference on Metal Organic Vapor Phase Epitaxy, San Diego, USA, 2016.
4. Poster presentation: N. Stolyarchuk, A. Courville, T. Neisus, J.L. Rouvière, O. Tottereau, S. Vézian, M. Albrecht and P. Vennéguès, "Transmission Electron Microscopy Investigation of III-Nitrides/Sapphire Interface at the Atomic Scale", International Workshop on Nitride Semiconductors, Wroclaw, Poland, 2014.

Selbständigkeitserklärung

Hiermit erkläre ich, dass ich die vorliegende Arbeit selbständig ohne fremde Hilfe und nur unter Verwendung der angegebenen Literatur und Hilfsmittel angefertigt habe. Des Weiteren bestätige ich hiermit, dass ich mich an keiner anderen Universität um einen Doktorgrad beworben habe und keinen entsprechenden Doktorgrad besitze. Ich habe Kenntnis über die dem Verfahren zugrunde liegende Promotionsordnung der Mathematisch-Naturwissenschaftlichen Fakultät der Humboldt-Universität zu Berlin.

Berlin, February 5, 2018

Natalia Stolyarchuk